

**NOVEL MULTIFUNCTIONAL SLOT-BASED POWER-
DIVIDING COUPLERS**

By

LIM CHIANG WEI

A dissertation submitted to the Department of Electrical and Electronic Engineering,
Faculty of Engineering and Science,
Universiti Tunku Abdul Rahman,
in partial fulfillment of the requirement for the degree of
Master of Engineering Science
in
May 2014

ABSTRACT

NOVEL MULTIFUNCTIONAL SLOT-BASED POWER-DIVIDING COUPLERS

Lim Chiang Wei

Microwave power divider is frequently used by various wireless subsystems. They can divide an input power into a number of smaller outputs for exciting the radiating elements in an antenna array. Usually, the same piece can also be used for power combining. Most existing power dividing structures are made of resonators such as hybrid and $\lambda/4$ line, which do not have high selectivity in spectrum. It is well known that a high-Q resonator gives better selectivity, but with the price of narrower bandwidth. Broad bandwidth, which is demanded by the modern microwave systems, can only be made on low-Q resonators. To solve this problem, they are usually incorporated with bandpass filters for improving selectivity. However, this causes the circuit size and footprint to increase significantly. In my project, for the first time, zeros are introduced to a multi-pole power divider for shaping the roll-off skirts at both the cutoff frequencies around the passband. By such an approach, it can be made to achieve wide bandwidth and high selectivity at the same time. The first part of this project is to explore different resonators for the making of the high-selective in- and out-of-phase power dividers. Multifunction concept is later introduced to re-configure the output phase.

Slot resonator, with low Q, is selected for broadband performance in the first part of my project. Travelling-wave mechanism is deployed. Three slots are

symmetrically cascaded in series for designing a 3-port power divider, giving simultaneous in-phase and out-of-phase outputs at different ports. Transmission zeroes are placed to the lower and upper bounds for reshaping the frequency roll-off rate, resulting in better selectivity. Later, the power divider is incorporated with the RF diodes so that it becomes a dual-functional component that gives either in-phase or out-of-phase signal.

In the second part, the multilayered slot-based bandpassing coupler is explored. It is designed on two circular patches with annular sectorial slot to provide bandpassing effect and multiple outputs. The proposed bandpassing power-dividing coupler can provide two 20-dB coupled signals simultaneously on a same design configuration by simply adding in two output ports to the bandpassing power divider. Meanwhile, it has kept the original performance of the half power division. Also, excellent selectivity has been achieved because two transmission zeroes are placed near to the lower and upper bounds for reshaping the frequency roll-off rate.

Ansoft HFSS was used to simulate all the configurations, with experiments done for verification. Good agreement is found between the simulated and measured data. Parametric analysis was also performed to study the effects of all the design parameters.

ACKNOWLEDGEMENT

I would like to thank Dr. Lim Eng Hock and Dr. Lo Fook Loong for their valuable guidance and advices throughout the completion of this research project. Besides, invaluable recommendations and suggestions have been shared. In addition, they were always available whenever I faced doubt.

I also wish to thank Mr. Ho, who guided me on fabrication process. With his experience, I am able to fabricate my design precisely. Besides that, I also like to extend my gratitude to all the seniors and friends during problem solving.

In addition, I would like to thanks to UTAR management for preparing a good environment for me to complete this project. Equipment, devices and materials have been prepared well. Moreover, UTAR had prepared and set up the OPAC system which enables students to obtain the necessary journal and scientific papers to complete the thesis writing successfully.

APPROVAL SHEET

This thesis entitled 'NOVEL MULTIFUNCTIONAL SLOT-BASED POWER DIVIDING COUPLERS' was prepared by LIM CHIANG WEI and submitted as partial fulfillment of the requirement for the degree of Master of Engineering Science at Universiti Tunku Abdul Rahman.

Approved by,

(Dr. Lim Eng Hock)

Supervisor

Department of Electrical and Electronic Engineering

Faculty of Engineering Science

Universiti Tunku Abdul Rahman

Date: _____

(Dr. Lo Fook Loong)

Co-supervisor

Department of Electrical and Electronic Engineering

Faculty of Engineering Science

Universiti Tunku Abdul Rahman

Date: _____

FACULTY OF ENGINEERING SCIENCE
UNIVERSITI TUNKU ABDUL RAHMAN

Date: 15th May 2014

SUBMISSION OF FINAL YEAR PROJECT /DISSERTATION/THESIS

It is hereby certified that **LIM CHIANG WEI**(ID No: **11 UEM 06592**) has completed this dissertation entitled “**NOVEL MULTIFUNCTIONAL SLOT-BASED POWER DIVIDING COUPLERS**” under the supervision of Dr. Lim Eng Hock (Supervisor) from the Department of Electrical and Electronic Engineering, Faculty of Engineering and Science (FES), and Dr. Lo Fook Loong(Co-Supervisor) from the Department of Electrical and Electronic Engineering, Faculty of Engineering and Science (FES).

I understand that University will upload softcopy of my final dissertation in pdf format into UTAR Institutional Repository, which may be made accessible to UTAR community and public.

Yours truly,

(LIM CHIANG WEI)

DECLARATION

I hereby declare that the dissertation is based on my original work except for citations and quotations which have been duly acknowledged. I also declare that it has not been previously and concurrently submitted for any other degree or award at UTAR or other institutions.

Name : LIM CHIANG WEI

Date : 15th May 2014

TABLE OF CONTENTS

ABSTRACT	ii
ACKNOWLEDGEMENT	iv
APPROVAL SHEET	v
DECLARATION	vii
TABLE OF CONTENTS	viii
LIST OF TABLES	x
LIST OF FIGURES	xi

CHAPTER

1	Introduction	1
	1.1 Background	1
	1.2 Problem Statement	3
	1.3 Research Objectives and Motivation	4
	1.4 Thesis Organization	5
2	Review of Traveling-wave Components	7
	2.1 Development of Traveling-wave Components	7
	2.2 Analysis Methods	10
	2.2.1 Transmission Line Method (TLM)	10
	2.2.2 Cavity Method	13
	2.2.3 Full-wave Method	14
3	Reconfigurable Traveling-wave Bandpassing Power Dividers	20
	3.1 Introduction	20
	3.2 In-phase Bandpassing Power Divider	22
	3.2.1 Configuration	22
	3.2.2 Simulation and Experiment Results	24
	3.2.3 Resonances and Field Characteristics	27

3.3	Out-of-phase Bandpassing Power Divider	32
3.3.1	Configuration	32
3.3.2	Simulation and Experimental Results	34
3.3.3	Resonances and Field Characteristics	37
3.4	Parametric Analysis	41
3.4.1	Gaps: G_1 and G_2	42
3.4.2	Interconnecting Slots: D_1 and S_1	45
3.4.3	Coupling Rings: W_1 , W_2 and W_3	48
3.5	Reconfigurable Bandpassing Power Divider	52
3.5.1	Configuration	52
3.5.2	Biasing Circuitry for RF PIN Diode	54
3.5.3	Simulation and Experimental Results	55
3.6	Conclusion	60
4	Multilayered Bandpassing Couplers	61
4.1	Introduction	61
4.2	Multilayered Bandpassing Power Divider	62
4.2.1	Configuration	62
4.2.2	Simulation and Experimental Results	66
4.2.3	Electric and Magnetic Field Characteristics	69
4.2.4	Parametric Analysis	71
4.3	Multifunctional Bandpass Power-Dividing Directional Coupler	77
4.3.1	Configuration	77
4.3.2	Simulation and Experiment Results	79
4.3.3	Electric and Magnetic Field Characteristics	84
4.3.4	Parametric Analysis	85
4.4	Conclusion	92
5	Conclusion	93
5.1	Summary	93
5.2	Future Works	93

References

LIST OF TABLES

TABLE	TITLE	PAGE
Table 2.1:	Examples of Traveling- and Standing-wave Components	9

LIST OF FIGURES

FIGURE	TITLE	PAGE
Figure 2.1:	Equivalent circuit of the antenna including the matching line.	12
Figure 2.2:	Transmission line model of slot antenna.	12
Figure 3.1:	Schematic of the proposed in-phase power divider.	23
Figure 3.2:	Photograph of the prototype: (a) Top view (b) Bottom view.	23
Figure 3.3:	Measured and simulated (a) amplitude response, (b) phase response of the in-phase power divider.	25
Figure 3.4:	Calculated amplitude imbalance and phase difference of the in-phase power divider.	26
Figure 3.5:	Measured and simulated isolation curves between the output ports of the in-phase power divider.	26
Figure 3.6:	Measured and simulated group delays at the output ports.	27
Figure 3.7:	Magnetic field distributions of the proposed in-phase power divider at (a) 1.58 GHz, (b) 2.93 GHz, and (c) 3.83 GHz.	29
Figure 3.8:	Wave fronts of P_1 at 1.58 GHz captured at different snapshots when the slot resonator is supplied with a microwave signal source with phases of (a) 0° , (b) 45° , (c) 75° , (d) 90° , (e) 120° , and (f) 165° at the input port.	30
Figure 3.9:	Wave fronts of the P_2 at 2.93 GHz captured at different snapshots when the slot resonator is supplied with a microwave signal source with phases of (a) 45° , (b) 105° , (c) 135° , (d) 150° , (e) 165° , and (f) 0° at the input port.	31

Figure 3.10:	Wave fronts of P_3 at 3.83 GHz captured at different snapshots when the slot resonator is supplied with a microwave signal source with phases of (a) 90° , (b) 150° , (c) 180° , (d) 15° , (e) 30° , and (f) 45° at the input port.	31
Figure 3.11:	Magnetic field distributions of the proposed in-phase power divider at 4.90 GHz.	32
Figure 3.12:	Schematic of the proposed out-of-phase power divider.	33
Figure 3.13:	Photograph of the prototype: (a) Top view (b) Bottom view.	33
Figure 3.14:	Measured and simulated (a) amplitude response, (b) phase response of the out-of-phase power divider.	35
Figure 3.15:	Calculated amplitude imbalance and phase difference of the out-of-phase power divider.	36
Figure 3.16:	Measured and simulated isolation curves between the output ports of the out-of-phase power divider.	36
Figure 3.17:	Measured and simulated group delays.	37
Figure 3.18:	Magnetic field distributions of the proposed out-of-phase power divider at (a) 1.59 GHz, (b) 2.94 GHz, (c) 3.80 GHz.	38
Figure 3.19:	Wave fronts of P_1 at 1.58 GHz captured at different snapshots when the slot resonator is supplied with a microwave signal source with phases of (a) 0° , (b) 30° , (c) 60° , (d) 90° , (e) 120° , and (f) 150° at the input port.	39
Figure 3.20:	Wave fronts of P_2 at 2.93 GHz captured at different snapshots when the slot resonator is supplied with a microwave signal source with phases of (a) 45° , (b) 90° , (c) 120° , (d) 135° , (e) 165° , and (f) 180° at the input port.	40
Figure 3.21:	Wave fronts of P_3 at 3.80 GHz captured at different snapshots when the slot resonator is supplied with a microwave signal source with phases of (a) 90° , (b) 165° , (c) 180° , (d) 15° , (e) 30° , and (f) 45° at the input port.	40
Figure 3.22:	The electric field distributions of the proposed out-of-phase power divider at 4.90 GHz.	41

Figure 3.23: Amplitude responses of the (a) in-phase power divider and (b) out-of-phase power divider when G_1 is varied.	43
Figure 3.24: Amplitude responses of the (a) in-phase power divider and (b) out-of-phase power divider when G_2 is varied.	44
Figure 3.25: Amplitude responses of the (a) in-phase power divider and (b) out-of-phase power divider when D_1 is varied.	46
Figure 3.26: Amplitude responses of the (a) in-phase power divider and (b) out-of-phase power divider when S_1 is varied.	47
Figure 3.27: Amplitude responses of the (a) in-phase power divider and (b) out-of-phase power divider when W_1 is varied.	49
Figure 3.28: Amplitude responses of the (a) in-phase power divider and (b) out-of-phase power divider when W_2 is varied.	50
Figure 3.29: Amplitude responses of the (a) in-phase power divider and (b) out-of-phase power divider when W_3 is varied.	51
Figure 3.30: Schematic of the proposed reconfigurable power divider.	53
Figure 3.31: Photograph of the prototype of the proposed reconfigurable power divider: (a) Top view.(b) Bottom view.	53
Figure 3.32: Biasing Circuit for the RF PIN Diode.	55
Figure 3.33: Measured and simulated (a) amplitude response, (b) phase response of the reconfigurable in-phase power divider.	57
Figure 3.34: Calculated amplitude imbalance and phase difference of the reconfigurable in-phase power divider.	58
Figure 3.35: Measured and simulated (a) amplitude response, (b) phase response of the reconfigurable out-of-phase power divider.	59

Figure 3.36:	Calculated amplitude imbalance and phase difference of the reconfigurable out-of-phase power divider.	60
Figure 4.1:	Schematic of the proposed bandpassing power divider: (a) Front view.(b) Top patch. (c) Bottom patch. (d) Concentric slot sectors in the middle layer.	64
Figure 4.2:	Photographs of the prototype of the proposed bandpassing power divider: (a) Top patch.(c) Bottom patch.(c) Concentric slot sectors in the middle layer.	65
Figure 4.3:	Measured and simulated (a) amplitude response, (b) phase response of the bandpassing power divider.	67
Figure 4.4:	Measured and simulated isolation curves between the output ports of the bandpassing power divider.	68
Figure 4.5:	Measured and simulated group delays.	68
Figure 4.6:	The field distributions of the proposed bandpassing power divider at (a) 2.25 GHz, (b) 2.71 GHz, (c) 1.69 GHz,(d) 3.52 GHz.	70
Figure 4.7:	Amplitude response of the bandpassing power divider when R_1 is varied.	72
Figure 4.8:	Amplitude response of the bandpassing power divider when R_2 is varied.	72
Figure 4.9:	Amplitude response of the bandpassing power divider when R_3 is varied.	73
Figure 4.10:	Amplitude response of the bandpassing power divider when R_4 is varied.	74
Figure 4.11:	Amplitude response of the bandpassing power divider when θ_1 is varied.	75
Figure 4.12:	Amplitude response of the bandpassing power divider when θ_2 is varied.	75
Figure 4.13:	Amplitude response of the bandpassing power divider when θ_3 is varied.	76
Figure 4.14:	Amplitude response of the bandpassing power divider when θ_4 is varied.	76

Figure 4.15:	Schematic of the proposed bandpass power dividing directional coupler: (a) Front view. (b) Top patch. (c) Bottom patch. (d) Concentric slot sectors in the middle layer.	78
Figure 4.16:	Photographs of the prototype of the proposed bandpass power dividing directional coupler: (a) Top patch. (c) Bottom patch. (c) Concentric slot sectors in the middle layer.	79
Figure 4.17:	Measured and simulated (a) amplitude response, (b) phase response of the half-power outputs of the bandpass power dividing directional coupler.	81
Figure 4.18:	Measured and simulated phase response of the 20-dB output signals of the bandpass power dividing directional coupler.	82
Figure 4.19:	Measured and simulated isolation between the output ports of the bandpass power dividing directional coupler.	82
Figure 4.20:	Measured and simulated group delays for the input signal to reach the half-power division ports (Ports 2 and 3).	83
Figure 4.21:	Measured and simulated group delays for the input signal to reach the 20-dB coupling ports (Ports 4 and 5).	83
Figure 4.22:	The field distributions of the proposed bandpassing power divider at (a) 2.23 GHz, (b) 2.71 GHz, (c) 1.78 GHz,(d) 3.53 GHz.	84
Figure 4.23:	Amplitude response of the bandpass power-dividing directional coupler when R_1 is varied.	86
Figure 4.24:	Amplitude response of the bandpass power-dividing directional coupler when R_2 is varied.	86
Figure 4.25:	Amplitude response of the bandpass power-dividing directional coupler when R_3 is varied.	87
Figure 4.26:	Amplitude response of the bandpass power dividing directional coupler when R_4 is varied.	88
Figure 4.27:	Amplitude response of the bandpass power-dividing directional coupler when θ_1 is varied.	89

Figure 4.28:	Amplitude response of the bandpass power-dividing directional coupler when θ_2 is varied.	89
Figure 4.29:	Amplitude response of the bandpass power-dividing directional coupler when θ_3 is varied.	90
Figure 4.30:	Amplitude response of the bandpass power-dividing directional coupler when θ_4 is varied.	90
Figure 4.31:	Amplitude response of the bandpass power-dividing directional coupler when θ_5 is varied.	91

CHAPTER 1

Introduction

1.1 Background

Microwave signal is electromagnetic wave working at frequencies ranging from 300 MHz to 300 GHz, corresponding to wavelength from 1 m to 1 mm in free space. Signal with wavelength lesser than 1 mm is usually referred as millimeter wave (J.-S. Hong, 2011). Because of its easy transmission in air, microwave spectrum has broadly been used for communication, radar, navigation, radio astronomy, sensing, etc. As the wavelength of a microwave signal is usually comparable or even smaller than the circuit size, it is more appropriate to use distributed elements to describe the microwave components, instead of the conventional low-frequency lumped elements (D. M. Pozar, 1998).

Nowadays, microwave components are highly demanded due to the rapid advancement of mobile and wireless communications. Among all, power dividers and combiners are frequently used by the wireless transmitters and receivers. They can divide an input power into a number of smaller outputs for excitation of the radiating elements in an antenna array. The multiplexing wireless systems also require the use of multiple power dividers so that the received RF signal can be equally divided into several channels. Besides that, for an I/Q modulator, the output modulated signals from the two mixers are combined through a two-way 3-dB in-phase power divider. Usually, the same piece can also be used for power combining.

The T-junction power divider is the simplest transmission line power-dividing structure. But, it is not possible to have all ports matched at the same time.

Since the 50s, myriads of microwave structures have been proposed to design different types of power dividers (E. J. Wilkinson, 1959; U. H. Gysel, 1975; K. J. Russell, 1979; K. Chang and C. Sun, 1983). E. J. Wilkinson was the first to propose a power divider which can have all the matched as well as minimum coupling among the output ports. Most existing power dividing structures are made of resonators such as hybrid or $\lambda/4$ line (Z. Jia, et al., 2006; J.-C. Chiu, et al., 2006; X. Tang and K. Mouthaan, 2009), which do not have broad bandwidth and high selectivity. Because of its low Q factor, the slot resonator has also been used for designing various broadband power dividers (N. Seman, et al., 2007; M. E. Bialkowski, et al., 2007; A.M. Abbosh, 2009). But the slot-based power dividers have poor selectivity. In order to solve this problem, they are usually incorporated with bandpass filters for improved selectivity.

A filtering power divider is a multifunctional component which can remove the unwanted signals efficiently. To achieve multifunction and high compactness, recently, filtering effect has also been embedded into different types of power dividers, both the passive and active. K. Song and Q. Xue (2010) disclosed a slot-line power divider which has bandpassing effect. It was shown that a bandpass filter, which is made of a pair of quarter-wavelength short-circuited stubs and two parallel coupled lines, can also be cascaded to the output ports of a standard Wilkinson power divider for shaping the roll-off-skirts of an ultra-wide passband (S. W. Wong, and L. Zhu, 2008). S. S. Gao, et al. (2013) proposed connecting two open-ended stubs as

well as embedding coupled lines into all the ports of a ring resonator to obtain multiple poles and zeros for a wideband bandpassing power divider. Similar design idea was also demonstrated by other researchers (K. Kim, et al., 2009; M.-J. Park, 2011). However, all of them require use of lumped resistors for improving isolation performance. In 2009, without needing any external components, P. K. Singh, et al. integrated a single-stage coupled line filter into the conventional Wilkinson power divider to improve selectivity. For active case in R. V. Gatti, et al., (2006), it was demonstrated that multiple diplexers and phase shifters can be combined using the RF PIN diodes for forming a power divider which is switchable between two passbands. G. Monti, et al. (2009) integrated MEMS switch in to the composite right/left-handed transmission to design a dual-band power divider that has reconfigurable power ratio.

1.2 Problem Statement

With the advent of multimedia era, most of the commercial wireless systems are required to work in multiple broad frequency bands. To provide wide bandwidth, at the component-level design perspective, it is more suitable to deploy microwave resonators that possess low Q-factor. Nevertheless, low-Q resonators do not give high selectivity, causing poor cutoff of undesirable noise. To solve this problem, in this thesis, multiple poles are combined with transmission zeroes for designing different wide-band power dividers with high selectivity. The resonances of the microstrip-based resonators are tactfully integrated to form wide passband and zeroes

that are near to the cutoff frequencies. In this thesis, several multifunctional power dividers will be explored. In the first project, the slot array configuration has been deployed for designing the in-phase and out-of-phase bandpassing power dividers, as well as one that is switchable. The second project proposes a power-dividing structure that can be used as a directional coupler at the same time. All of the proposed configurations are able to achieve broad bandwidth and high selectivity simultaneously.

1.3 Research Objectives and Motivation

In this thesis, two projects have been conducted to achieve the same research objectives and motivation. In both, complex slot resonators are explored for the design of different multifunctional power-dividing structures. Also, multiple poles and zeros are added to provide broad bandwidth and high selectivity. The first project is devoted to studying an array which is made by combining three slots in series to give in-phase and out-of-phase power divisions. In the second project, multiple slot annular sectors are incorporated with the microstrip patch resonators for a dual-functional component that can provide power division and signal coupling at the same time.

In Chapter 3, the traveling-wave mechanism of the slot array is explored for designing a multifunctional and multimode power divider that can be configured to give in-phase or out-of-phase power division. Three poles have been successfully

combined to provide a broad bandwidth of greater than 100%. Also, the introduction of multiple transmission zeros is achieved for shaping the roll-off skirts near to the cutoff frequencies. This bandpassing feature is very useful for improving the selectivity of the proposed power dividers. It can also be made reconfigurable by incorporating several RF PIN diodes into the slot array structure, making it switchable as an in-phase or out-of-phase power divider.

Chapter 4 is dedicated to studying a dual-functional hybrid resonator which is constructed by merging annular sectorial slots and microstrip circular patches. This structure can be optimized to work as an in-phase power divider. An additional function – Power-dividing Directional Coupler can also be implemented in the same piece of resonator without disturbing the operation of the half-power divider. For all, multiple poles and zeros have been introduced to widen the passband as well as to sharpen the roll-off skirts.

1.4 Thesis Organization

An overview of the thesis will be provided in this section. There are 5 chapters in this thesis. A complete reference list has also been appended.

Chapter 1 introduces the concept of multifunctional microwave components such as antenna filter, balun filter and filtering power dividers. The recent development and current issues are also discussed in this chapter.

Chapter 2 discusses the physical mechanism of travelling-wave. A review on the analysis methods is also provided. Some of the recently proposed radiating and non-radiating travelling-wave components are described.

Chapter 3 explores a dual-function power divider. In the first part, a slot array resonator structure is deployed for designing the in-phase and out-of-phase power dividers. Next, they are combined to form a reconfigurable component that can give in-phase or out-of-phase output with the use of several RF PIN diodes. Parametric analysis is also conducted, along with elucidation.

Chapter 4 explores a hybrid resonator that is made by combining the annular sectorial slots and circular patches. A bandpassing half-power power divider is first demonstrated. Later, a multifunctional power divider that can give in-phase half-power division with an additional coupled signal is analyzed. The design theory is then discussed. Experiments are performed to verify its performance.

Chapter 5 summarizes the research and future works presented in this dissertation.

CHAPTER 2

Review of Traveling-wave Components

2.1 Development of Traveling-wave Components

Traveling-wave mechanism was first explored for slot antenna by J. N. Hines, et al. (1953), with performance similar to the traveling-wave wire. W. Menzel (1978) studied the radiation characteristics of a long traveling-wave rectangular microstrip patch antenna, with no design equation provided. Later in 1990, A. K. Bhattacharyya derived the formula for the higher-order traveling-wave resonance of the long rectangular patch, which can achieve an antenna gain of ~10-dBi with an operating bandwidth 4.1%. For broadband usage, W.-R. Dong and D. L. Sengupta (1984) proposed a microstrip traveling wave antenna by cascading several non-uniform rectangular patches for a wider bandwidth (~40%) and a higher gain (~10-dBi), with the price of increasing the circuit size. Similar design concept was also demonstrated by P. Hallbjorner, et al. (2005) in the design of a millimeter-wave switched beam antenna. T.-L. Chen and Y.-D. Lin (1998) employed the first higher-order mode to design a broadside leaky-wave microstrip array. This structure has isolated the feeding network from the radiating element. Furthermore, the position of the slot can be adjusted to achieve the desired scanning angle range, which is very desired by the scanned beam antenna. A fixed-frequency dual-beam steering microstrip leaky-wave antenna was later implemented by Y. Li, et al. (2008) to achieve high gain. The main beams can be switched by changing the feeding positions. All the aforementioned designs are for linear polarization.

The concept of a novel circularly polarized (CP) traveling-wave patch array was demonstrated by K. M. Lum, et al. (2005), which has an operating bandwidth of 6%. The proposed structure is particularly suitable for the highly integrated multilayer transceivers since its aperture coupling mechanism does not require any feeding probe, but its CP bandwidth is much narrower. In order to achieve broader CP bandwidth, S.-K. Lin and Y.-C. Lin (2011) combined the traveling-wave and resonant modes of circular aperture to achieve an antenna bandwidth of ~55%, but the gain is low (~5-dBic) because the Q-factor of the slot is low. To have higher antenna gain, Y. Li, et al., (2007) crossed two long patches orthogonally to generate CP operation. In general, microstrip leaky-wave antennas have the advantages of high directivity, compact size, low profile, ease of matching, and frequency-scanning ability.

Since the early 50s, many different types of coupler structures have been proposed for a myriad of power dividers. F. S. Coale first proposed a new type of filter based on traveling-wave mechanism, where two directional couplers were combined to form a transmission-line loop for the design of a directional filter. A similar idea was used to construct a traveling-wave half-mode substrate integrated waveguide (HMSIW) directional filter (Y. Cheng, et al., 2007) which has not only good performances such as low insertion loss, high Q factor, high power handling capacity, and mass producibility, but it also cuts the component size by half. Later in 1980, A. G. Bert and D. Kaminsky presented a traveling-wave power divider that can give wide bandwidth. The same design idea was also applied by H. Q. Tserng and P. Saunier (1985) in the design of a high frequency power divider. However, most of

the traveling-wave passive components are bulky in size and work at low frequency. To solve this problem, in 1994, C. W. Cheung and Y. O. Yam designed a traveling-wave power divider/combiner for low frequency by using lumped elements for miniaturization.

Usually, the size of the standing-wave component is inversely proportional to its operating frequency. As a result, it can be very hard to fabricate a microwave component at higher frequency as the footprint is very small. In the millimeter-wave ranges, a larger circuit size is always desired for the ease of fabrication. Some of the traveling- and standing-wave components are summarized in Table 2.1. It can be seen that the circuit size of the traveling is usually much larger than one wavelength. Also, the bandwidth of the standing-wave component is much smaller.

Table 2.1: Examples of Traveling- and Standing-wave Components

Examples	Component	Frequency (GHz)	Maximum Dimension (mm)	Bandwidth (%)
A. K. Bhattacharyya, 1990	Traveling-wave patch antenna	2.48	275 ($\sim 3\lambda_g$)	4.1
Y. Li, et al., 2008	Traveling-wave patch antenna	7.00	128.6 ($\sim 4.5 \lambda_g$)	4.25
Z. Zakaria, et al., 2012	Standing-wave patch antenna	2.00	32.72 ($\sim 0.4 \lambda_g$)	2.00

2.2 Analysis Methods

There are three methods to analyze the traveling-wave components (C. A. Balanis, 1997), namely transmission line method, cavity method, and full-wave method. The transmission line model is the easiest among all. It gives good physical insight, but this method provides no insight into the coupling mechanism. The cavity model is much more complicated and more accurate compared to transmission line model. Again, it is not able to model the cross-coupling fields. Full-wave model is very complex, but it is very accurate and versatile. This method can be used to model the coupling mechanism for the finite and infinite structures.

2.2.1 Transmission Line Method (TLM)

Transmission line theory is a common method that has been broadly used for analyzing different types of microwave resonators (C. A. Balanis, 1997). A. K. Bhattacharyya (1990) showed that a microstrip rectangular long patch ($a \times b$) can be represented by the equivalent circuit in *Figure 2.1*. The lumped elements of the resonator can be expressed as

$$y_1 = jay_0\{\csc(\beta b) - \cot(\beta b)\} \quad (2.1)$$

and

$$y_2 = -ja y_0 \csc(\beta b) \quad (2.2)$$

where a and b are the length and width of the patch, respectively while

$$y_0 = \frac{\beta}{\omega \mu} \quad (2.3)$$

and the propagation constant (β) is taken as real since the line is lossless along y -axis.

J. E. Ruyle and J. T. Bernhard (2011) used the TLM method to analyze the slot resonating antenna. *Figure 2.2* shows the equivalent circuit of the slot antenna and the voltage wave inside the slot can be expressed as

$$V_m(x) = A_m \left(e^{-\gamma_m x} + \frac{B_m}{A_m} e^{\gamma_m x} \right) \quad (2.4)$$

where γ_m is the modal propagation constant and B_m/A_m is the modal ratio between the forward and backward voltage waves. The current can be expressed as

$$I_m(x) = \frac{A_m}{Z_c} \left(e^{-\gamma_m x} - \frac{B_m}{A_m} e^{\gamma_m x} \right). \quad (2.5)$$

The end of the slot is no longer shorted when the width of the slot is increased, therefore the slot appear to be inductive. The inductance can be expressed as

$$L = 0.2w_a \left(\ln \left(\frac{4w_a}{d} \right) + \frac{d}{2w_a} - 1 \right) \text{nH} \quad (2.6)$$

where w_a is the width of the slot and d is the effective width of the equivalent wire that creates the load inductance. The parameter d can be expressed as

$$d = \frac{w_a + h_m}{20p^2} \quad (2.7)$$

where

$$p = \frac{\lambda_0}{\lambda} \quad (2.8)$$

and h_m is the metal thickness of the ground plane. The slot becomes resistive when its width is increased. In this case, the resistance can be expressed as

$$R = 2.63 \times 10^{-3} \frac{w_a}{d} \sqrt{f} \quad (2.9)$$

where f is the frequency in GHz. Therefore, the impedance of each end of the slot is

$$Z_L = R + j\omega L. \quad (2.10)$$

This wideband TLM model can be used to analyze the resonance modes of a slot antenna that go beyond the first resonance mode.

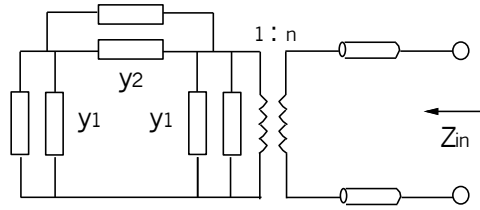


Figure 2.1: Equivalent circuit of the antenna including the matching line.

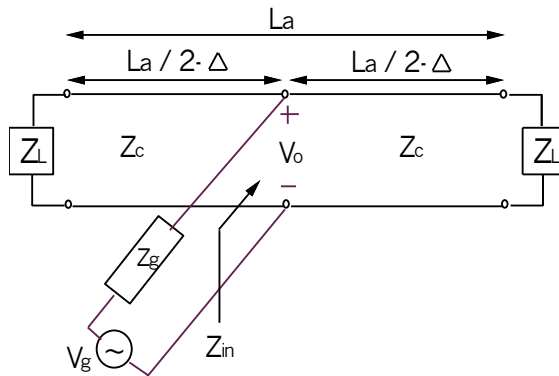


Figure 2.2: Transmission line model of slot antenna.

2.2.2 Cavity Method

In 2002, P.-W. Chen, et al. used the cavity model to analyze a double-layered microstrip leaky-wave antenna. Here, the full-wave spectral domain technique was used to calculate the attenuation constant as the cavity model itself is not able to do it. Again, this method was used by Y. Li, et al. (2008) to study the characteristics of a dual-beam steering leaky wave long patch. Cavity model is an approximate model that gives good physical insight, but it does not include radiated power. It assumes that the patch resonator is composed of two electric conductors on the top and bottom surfaces but perfect magnetic conductors at all the four sides. The homogeneous wave function A_x (C. A. Balanis, 1997) inside the cavity can be written as,

$$\nabla^2 A_x + k^2 A_x = 0. \quad (2.11)$$

The electric and magnetic fields inside the cavity can be calculated after knowing A_x . By applying all the given boundary conditions, the solution of the wave function is

$$A_x = A_{mnp} \cos(k_x x') \cos(k_y y') \cos(k_z z') \quad (2.12)$$

where A_{mnp} denotes the amplitude coefficient of each mnp mode. The wave numbers k_x, k_y, k_z are defined as

$$\left. \begin{aligned} k_x &= \left(\frac{m\pi}{h}\right), m = 0, 1, 2, \dots \\ k_y &= \left(\frac{n\pi}{L}\right), n = 0, 1, 2, \dots \\ k_z &= \left(\frac{p\pi}{W}\right), p = 0, 1, 2, \dots \end{aligned} \right\} m = n = p \neq 0 \quad (2.13)$$

where m, n, p represent, respectively, the number of half-cycle field variations along the x, y, z directions. Since the wave numbers k_x, k_y, k_z are constrained by

$$k_x^2 + k_y^2 + k_z^2 = \left(\frac{m\pi}{h}\right)^2 + \left(\frac{n\pi}{L}\right)^2 + \left(\frac{p\pi}{W}\right)^2 = k_r^2 = \omega_r^2 \mu \epsilon, \quad (2.14)$$

the resonant frequencies of the cavity are given by

$$(f_r)_{mnp} = \frac{1}{2\pi\sqrt{\mu\epsilon}} \sqrt{\left(\frac{m\pi}{h}\right)^2 + \left(\frac{n\pi}{L}\right)^2 + \left(\frac{p\pi}{W}\right)^2}. \quad (2.15)$$

This model is only applicable when the substrate thickness (h) is small so that the electric field variation along the z -axis becomes negligible.

2.2.3 Full-wave Method

Numerical techniques such as method of moments(MoM), and the finite-elements(FEM) method and the time-domain finite difference(FDTD) technique are among the full-wave methods that are commonly used for analyzing many types of microwave structures (C. A. Balanis, 1997). MoM is simple as it only requires the calculation of currents on the boundaries, rather than extracting the fields throughout the entire space. It is very advantageous in analyzing the two-dimensional (2D) structures. The FEM analyzes the 3D structures in the form of partial differential equation (PDE) or integral equation. It is able to handle complex geometries with complex restraints. Comparing with MoM, the FEM is more computational intensive as it involves 3-dimensional space. The FEM is more suitable to analyze closed space problems such as waveguide and cavities. This is because it does not have a

high-performance absorbing boundary. The FDTD method can solve complex problems, but it is generally very expensive. This is because the solutions may require a large amount of memory and computation time. The FDTD algorithms solve the Maxwell's equations in a fully explicit way in time domain, but the MoM and FEM algorithms solve them implicitly by solving matrices in the frequency domain.

2.2.3.1 Method of Moment

The MoM solves an electromagnetic problem by converting it into an operator equation, which can be in the form of integral or integro-differential (W. Yu, et al., 2011). The unknowns are expanded into a finite number of well-chosen basic functions. By taking the scalar product between the operator equation and a set of testing functions, a set of matrix equations can be generated. The resulting matrix equation is then solved by using a direct or iteration method. The operator equation can be expressed as

$$Lf = h \tag{2.16}$$

where L is a linear differential or integral operator. h is a known function while f is an unknown function that needs to be solved and it can be expressed as the expansion of the basic functions,

$$f(x) \approx a_1 f_1(x) + a_2 f_2(x) + \dots + a_N f_N(x) = \sum_{n=1}^N a_n f_n(x) \quad (2.17)$$

where a_n are the coefficients of the unknown f . The new operator equation can then be written as

$$\sum_{n=1}^N a_n L f_n(x) \approx h(x). \quad (2.18)$$

A set of weight functions (w_1, w_2, \dots, w_n) will be selected to multiply with unknown function $f(x)$ to generate a set of linear equations,

$$\sum_{n=1}^N Z_{mn} L a_n = b_n, m = 1, 2, 3, \dots, N \quad (2.19)$$

where

$$Z_{mn} = \int w_m(x) L f_n dx \quad (2.20)$$

$$b_m = \int w_m(x) h(x) dx. \quad (2.21)$$

The unknown function $f(x)$ can be solved after the coefficients a_n are calculated. D. Yau, et al. (1999) combined the traveling-wave and basic functions for the current expansion to minimize the number of unknowns. This reduces the computation times and resources significantly. M. Lucido, et al., (2008) re-constructed the edge behavior of the EM field so that a more accurate MoM result can be obtained for the leaky wave antennas.

2.2.3.2 Finite-Element Method

The FEM formulation is built through the variational or Galerkin approach (W. Yu, et al., 2011). When the global parameter is needed, it is much desired to use the variational approach. But the Galerkin approach is more flexible. Scalar variation formulation is the simplest approach to use with FEM. The Poisson equation for calculating the potential φ generated by a charge ρ in a domain Ω can be written as,

$$\nabla \cdot (\varepsilon \nabla \varphi) = -\rho. \quad (2.22)$$

Most 3D problems can be expressed in a vector field which is generalized from the single scalar formulation. Assuming a domain Ω is filled with the material having permittivity, ε_r and permeability, μ_r , an arbitrary current density J_{imp} in this domain will generate an electric field that satisfies

$$\nabla \times \left(\frac{1}{\mu_r} \nabla \times \vec{E} \right) - k_0^2 \varepsilon_r \vec{E} = -jk_0 Z_0 J_{imp} \quad (2.23)$$

$$k_0 = \omega \sqrt{\frac{\varepsilon_0}{\mu_0}} \quad (2.24)$$

$$Z = \sqrt{\frac{\varepsilon_0}{\mu_0}} \quad (2.25)$$

where k_0 is the propagation constant in free space and Z is the wave impedance. After applying boundary condition, it can be expressed as the following equation through a weighted function,

$$\vec{K} \vec{E} = \vec{b} \quad (2.26)$$

where \vec{K} is the matrix associated with the system, \vec{E} is the unknown vector that will be solved, and \vec{b} is the known vector which is determined by the charge and boundary condition. C. K. Wu and C. K. C. Tzuang (2002) used the PBG cells to design the magnetic surface of a higher-order leaky-wave antenna, which is analyzed by the FEM. H. Jiang, et al., (2006) showed that the inhomogeneous dielectric profiles can be analyzed by using the FEM. Also, it was used to evaluate the field and performance of a leaky-wave antenna.

2.2.3.3 Finite Difference Time Domain Method

K. S. Yee (1966) was the first to use the FDTD algorithm to solve an electromagnetic problem. In order to get electric and magnetic fields staggered in space and time, this method replaces the derivatives of the Ampere's and Faraday's laws with finite differences, which are

$$\frac{\partial E_x}{\partial t} = \frac{1}{\varepsilon_x} \left(\frac{\partial H_z}{\partial y} - \frac{\partial H_y}{\partial z} - \sigma_x E_x \right) \quad (2.27)$$

$$\frac{\partial E_y}{\partial t} = \frac{1}{\varepsilon_y} \left(\frac{\partial H_x}{\partial z} - \frac{\partial H_z}{\partial x} - \sigma_y E_y \right) \quad (2.28)$$

$$\frac{\partial E_z}{\partial t} = \frac{1}{\varepsilon_z} \left(\frac{\partial H_y}{\partial x} - \frac{\partial H_x}{\partial y} - \sigma_z E_z \right) \quad (2.29)$$

$$\frac{\partial H_x}{\partial t} = \frac{1}{\mu_x} \left(\frac{\partial E_y}{\partial z} - \frac{\partial E_z}{\partial y} - \sigma_{Mx} H_x \right) \quad (2.30)$$

$$\frac{\partial H_y}{\partial t} = \frac{1}{\mu_y} \left(\frac{\partial E_z}{\partial x} - \frac{\partial E_x}{\partial z} - \sigma_{My} H_y \right) \quad (2.31)$$

$$\frac{\partial H_z}{\partial t} = \frac{1}{\mu_z} \left(\frac{\partial E_x}{\partial y} - \frac{\partial E_y}{\partial x} - \sigma_{Mz} H_z \right) \quad (2.32)$$

where ε, σ, μ and σ_M are the electric and magnetic constitutive parameters of the material. M. K. Kim, et al., (2000) used the FDTD to analyze a wide rectangular slot antenna, yielding good agreement between simulation and measurement. FDTD method can also be used to calculate the complex propagation constant of the microstrip leaky-wave antenna (Y. Li, et al., 2008).

CHAPTER 3

Reconfigurable Traveling-wave Bandpassing Power Dividers

3.1 Introduction

A slot array which can be configured into either an in-phase or out-of-phase microwave power divider will be explored in this chapter. The concept of placing multiple resonators into array form is popular in antenna design so that stronger field is obtainable afar. In the 80s, the traveling-wave mechanism of a serially cascaded rectangular patch array was demonstrated to have a broader antenna bandwidth (W.-R. Dong, et al., 1984). The patch arrays have been widely used in mobile communication systems due to their distinctive features such as compactness, ease of fabrication, high power handling, frequency-scanning capability, and wideband performance (Y. Hase, et al., 1996; E. E. Okon and C. W. Turner, 2002; Y. E. Erdemli, et al., 2002; K. Wincza and S. Gruszczynski, 2011). On the other hand, the dumb-bell-shaped slot, which is formed by interconnecting two slot resonators in array form, has been broadly deployed for designing various periodic defected ground structures (DGS). In some cases (D. Packiaraj, et al., 2008; R. Chaudhuri, et al., 2011), the slot arrays were used as the resonating standing-wave structures. The size of a standing-wave component is usually inversely proportional to its operating frequency, causing the component size to become very small at the higher frequency. This causes the design complexity and the material cost to increase significantly. For the first time in my project, the traveling-wave mechanism of the slot array is explored for designing passive and active power dividers. As the traveling-wave

component does not reduce in size when its operating frequency goes up, this makes the manufacturability mechanically possible. To demonstrate, three rectangular slot resonators are interconnected by narrow slot lines and each of them is excited by a metallic ring to give three operational ports, which can be configured into a passive component that provides either in-phase or out-of-phase outputs. To make it more versatile, several RF switches have been inserted into the feedlines, making it an active four-port device that can be configured to become both an in-phase or out-of-phase power divider in one piece. Ansoft HFSS (Ansoft Corporation, HFSS) was used to simulate all the configurations, with parametric analysis performed to study the effects of the design parameters. Manual optimization approach is adopted due to the unavailability of the HFSS Optimizer. Although the optimization process may get slower, it enables real-time visualization and analysis of the simulated data. The high-frequency laminated substrate RT/Duroid 6006, with dielectric constant of $\epsilon_r = 6.15$ and thickness of $h = 0.635$ mm, was used for fabricating the prototypes. Experiments were done by using R&S®ZVB8 Vector Network Analyzer (VNA) to verify the simulated results.

3.2 In-phase Bandpassing Power Divider

3.2.1 Configuration

The configuration of the proposed in-phase bandpassing power divider will be discussed in this section, with the schematic depicted in *Figure 3.1*. It is a 3-port structure made by three rings located on the top surface of a substrate with each of them exciting a slot on the bottom. Port 1 is the input port while Ports 2 and 3 are the outputs. The input signal travels from the central slot to the neighboring ones through two narrow slot lines. And this slot array is symmetric along $A - A'$ and $B - B'$. All rings are connected to the 50Ω microstrip feed lines. The detailed design parameters of the proposed in-phase power divider are given by $L_1 = 13.6\text{mm}$, $L_2 = 17.6\text{mm}$, $L_3 = 12.4\text{mm}$, $L_4 = 12\text{mm}$, $G_1 = 0\text{mm}$, $G_2 = 0.6\text{mm}$, $D_1 = 2.75\text{mm}$, $S_1 = 3\text{mm}$, $W_1 = 0.2\text{mm}$, $W_2 = 0.2\text{mm}$, $W_3 = 0.4\text{mm}$. A cavity was used as a shield to minimize radiation. The prototype is shown in *Figure 3.2*.

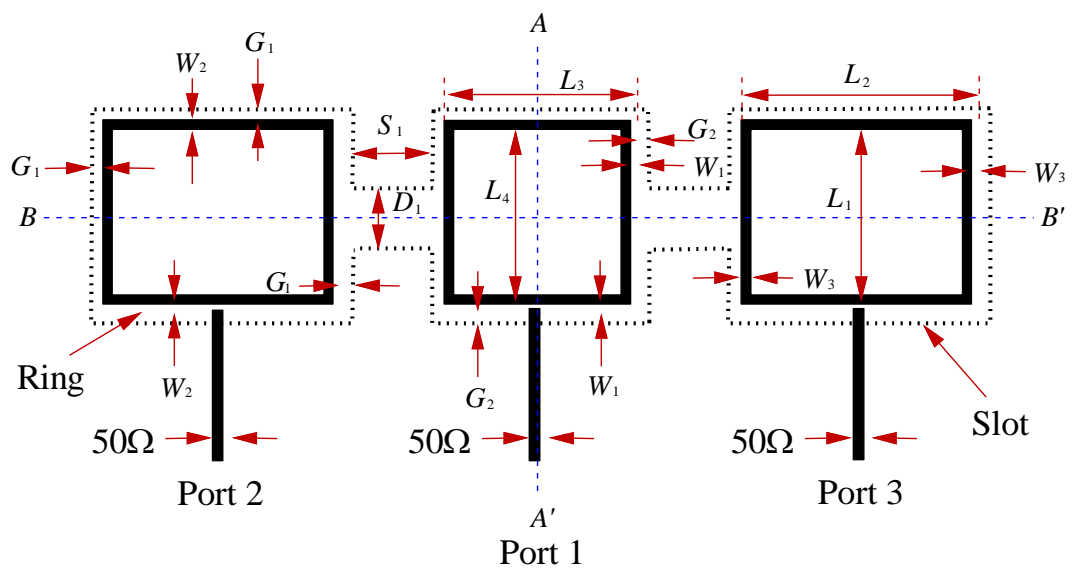


Figure 3.1: Schematic of the proposed in-phase power divider.



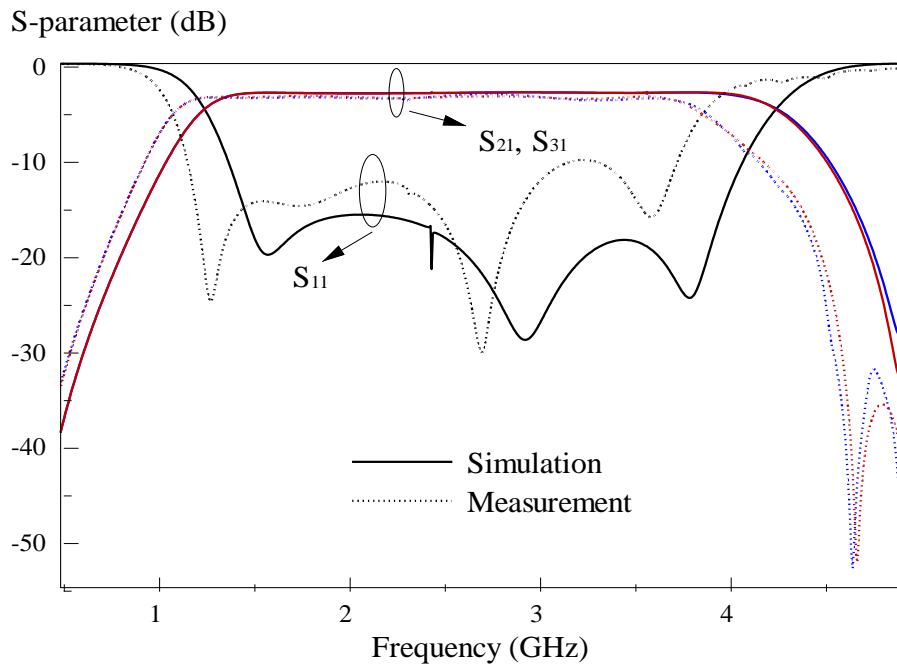
(a)

(b)

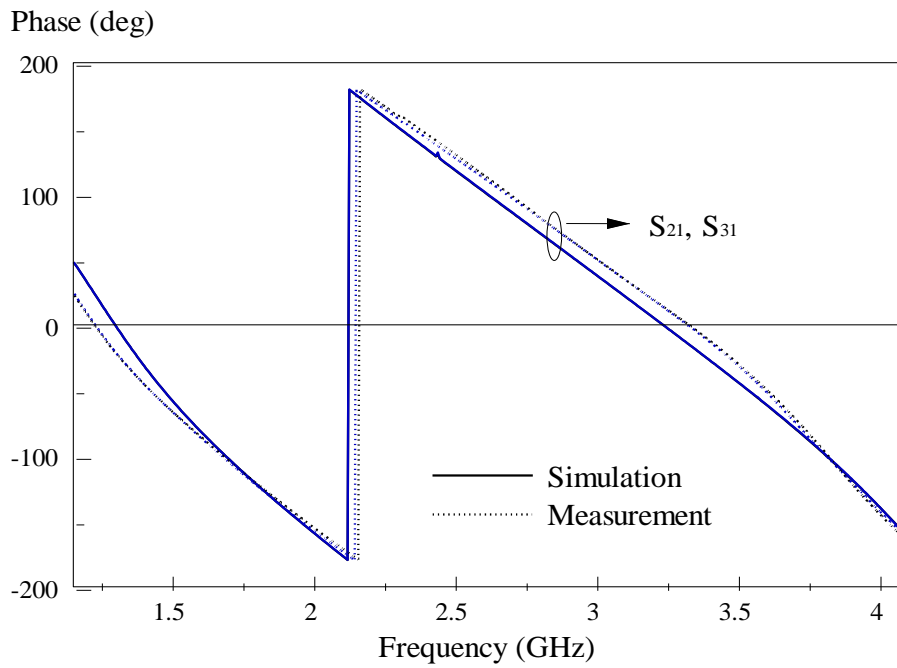
Figure 3.2: Photograph of the prototype: (a) Top view (b) Bottom view.

3.2.2 Simulation and Experiment Results

From the amplitude and phase responses shown in *Figure 3.3*, the experimental and simulation results agree well. Three resonances are observed in simulation forming a broad bandwidth. Also, transmission zeros are available near to the cutoff frequencies to shape the roll-off skirts for a better selectivity. It can be seen from simulation that the in-phase power divider has a passband covering 1.38 - 4.08 GHz, giving a fractional bandwidth of 98.90%. Measurement shows an operating frequency range of 1.17-3.74 GHz, with a fractional bandwidth of 104.68%, slightly larger than the simulated result. It can be seen from *Figure 3.4* that an input power at Port 1 is equally divided between the two output ports with an amplitude imbalance of less than 1dB across the passband. Besides that, the output signals are in-phase ($|\angle S_{21} - \angle S_{31}|$) with a discrepancy of less than $\pm 4^\circ$ across the passband. With reference to *Figure 3.5*, the isolation between the two outputs is around -6-dB - -7-dB across the entire passband. Both the measured and simulated group delays (*Figure 3.6*) show a constant delay of ~0.5 ns throughout the entire passband. This is very positive as it implies that the input signals experience minimum distortion when getting through the component.



(a)



(b)

Figure 3.3: Measured and simulated (a) amplitude response, (b) phase response of the in-phase power divider.

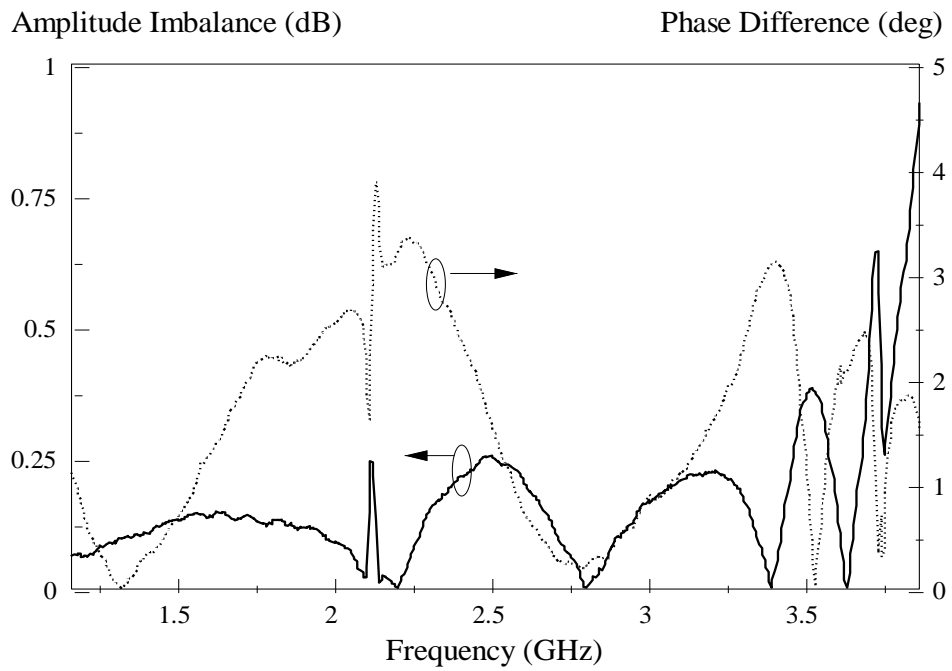


Figure 3.4: Calculated amplitude imbalance and phase difference of the in-phase power divider.

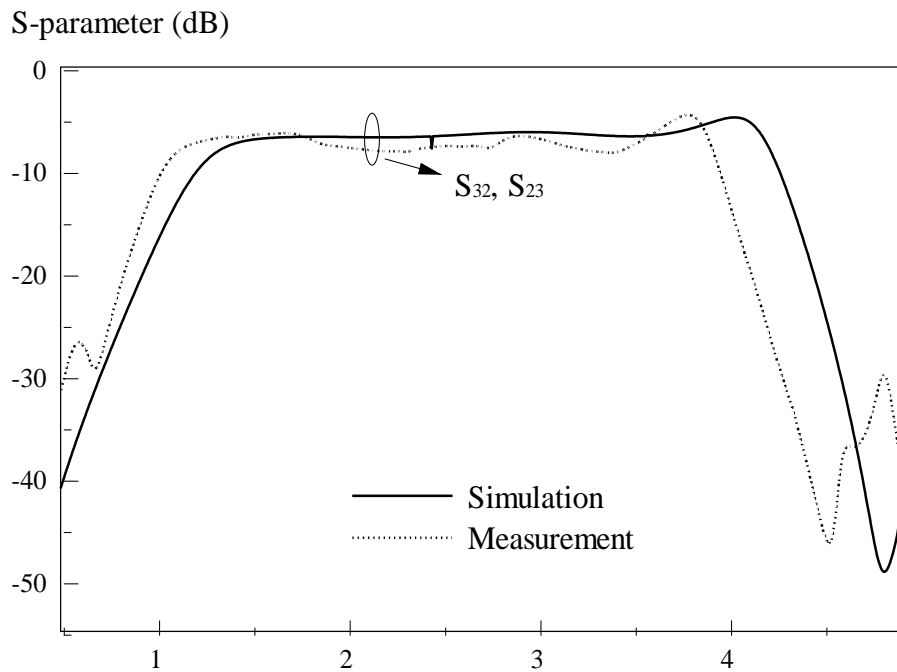


Figure 3.5: Measured and simulated isolation curves between the output ports of the in-phase power divider.

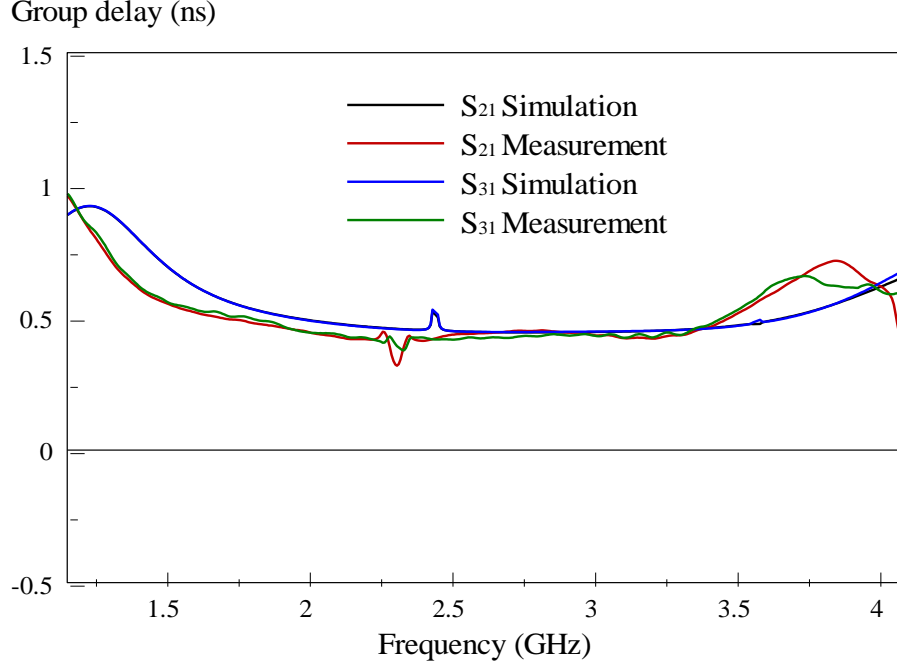


Figure 3.6: Measured and simulated group delays at the output ports.

3.2.3 Resonances and Field Characteristics

The magnetic field distributions of the slot array for the proposed in-phase power divider are illustrated in this section. As can be seen from the amplitude response in *Figure 3.3(a)*, the simulated reflection coefficient has three poles at 1.58 GHz (P_1), 2.93 GHz (P_2), and 3.83 GHz (P_3). Now, their corresponding magnetic field distributions are shown in *Figure 3.7(a)-(c)*. As can be seen from the fields in *Figure 3.7(a)*, the first resonating mode can be curve-fitted as

$$f_{P1} = \frac{c}{A_{P1}\sqrt{\epsilon_{eff}}} \quad (3.1)$$

where c is speed of light, $\epsilon_{reff} = \frac{\epsilon_r + 1}{2}$ and A_{P1} is expressed as

$$A_{P1} = \left[\left(\frac{L_2 + 2G_1}{2} \right) + (L_1 + 2G_1 + 2W_2) + (L_2 + 2G_1) + \left(\frac{L_1 + 2G_1 + 2W_2 - D_1}{2} \right) \right] \times 2 \quad (3.2)$$

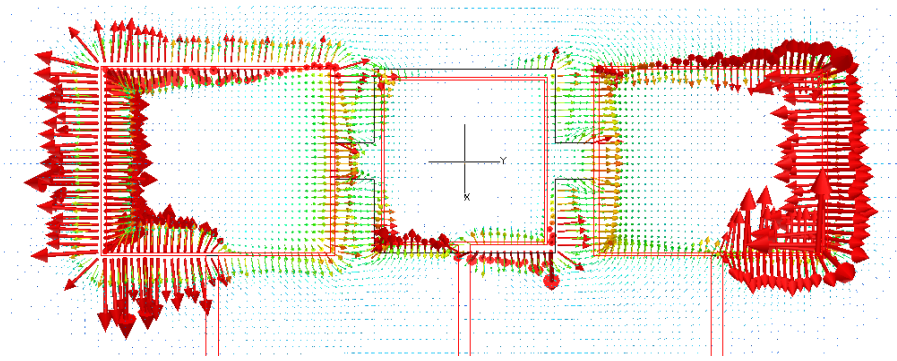
For the given configuration, the resonating frequency f_{P1} is calculated to 1.55 GHz, which is pretty close to the simulated one of 1.58 GHz. It can be observed from the magnetic field patterns in *Figure 3.7(a)* that there exist two crests in the side rings. With reference to the field patterns in *Figure 3.7(b)*, the resonant frequency of the P_2 can be obtained by $f_{P2} = \frac{c}{A_{P2}\sqrt{\epsilon_{eff}}}$, where

$$A_{P2} = [(L_1 + 2G_1 + 2W_2) \times 2] + 2S_1 + (L_3 + 2G_2) \quad (3.3)$$

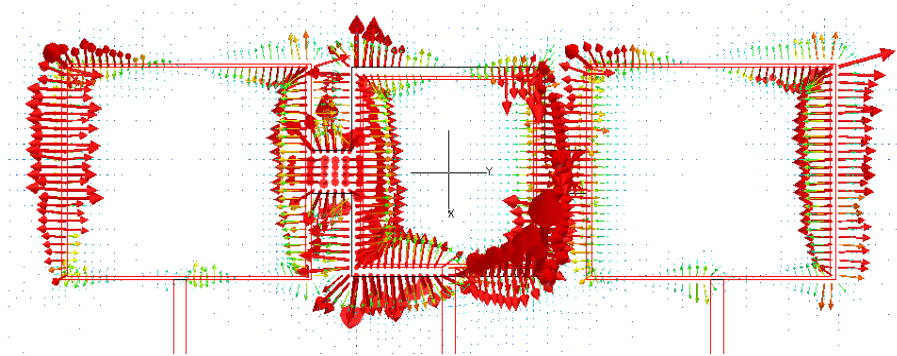
The resonant frequency can be calculated as 3.00 GHz, which not far from the simulated one of 2.93GHz. The magnetic fields for P_3 shows that the resonant frequency can be approximated by $f_{P3} = \frac{c}{A_{P3}\sqrt{\epsilon_{eff}}}$, where

$$A_{P3} = \left[\left(\frac{L_2 + 2G_1}{2} \right) + \left(\frac{L_1 + 2G_1 + 2W_2}{2} \right) + S_1 \right] \times 2. \quad (3.4)$$

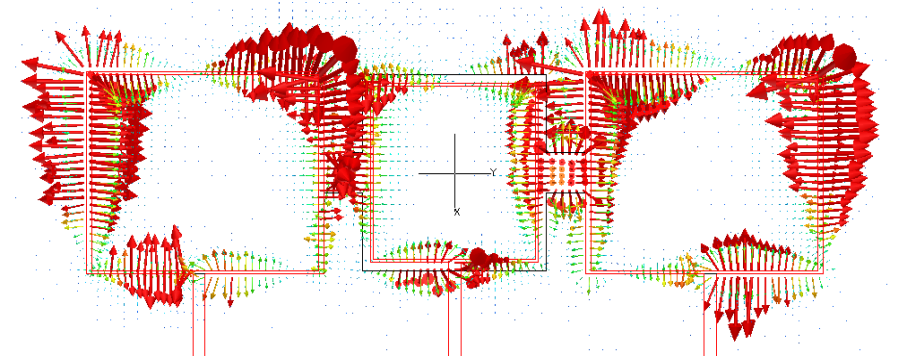
The third pole frequency is located around 3.80 GHz, agreeing well to the simulation (3.83GHz).



(a)



(b)



(c)

Figure 3.7: Magnetic field distributions of the proposed in-phase power divider at (a) 1.58 GHz, (b) 2.93 GHz, and (c) 3.83 GHz.

To visualize wave propagation of the proposed in-phase power divider, magnetic fields at different snapshots are studied on the slot resonator in *Figure 3.1*. For the P_1 at 1.58 GHz, a wave front is seen propagating from the input to the output ports when the slot resonator is supplied with a microwave signal source with different phases of 0° , 45° , 75° , 90° , 120° , and 165° at the input port, shown in *Figure 3.8*. This shows that it is a traveling-wave resonator. Similar property has been observed in the P_2 and P_3 in *Figure 3.9* and *3.10*.

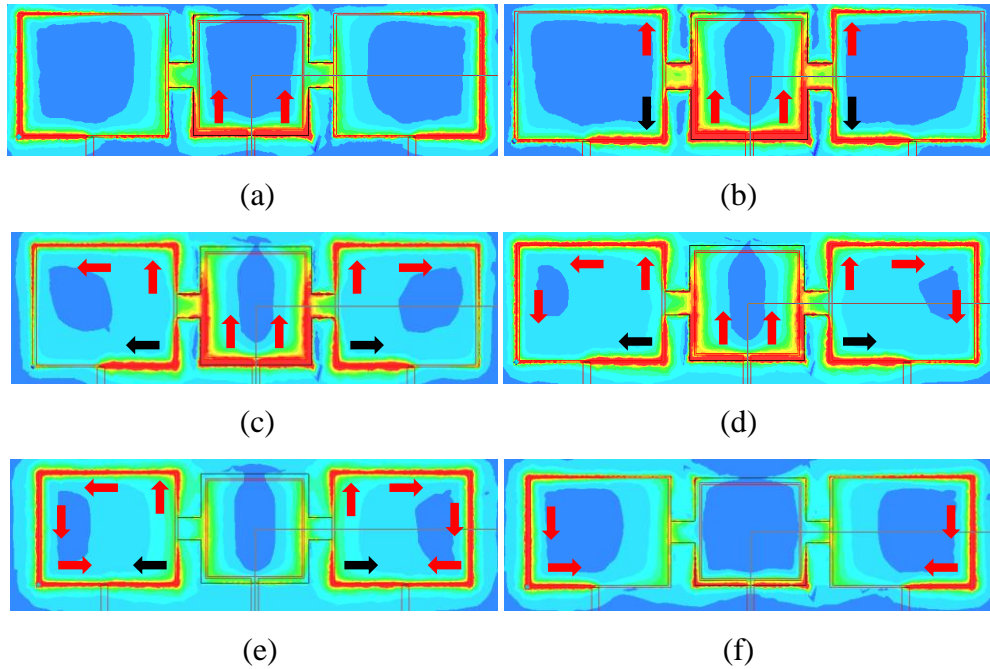


Figure 3.8: Wave fronts of P_1 at 1.58 GHz captured at different snapshots when the slot resonator is supplied with a microwave signal source with phases of (a) 0° , (b) 45° , (c) 75° , (d) 90° , (e) 120° , and (f) 165° at the input port.

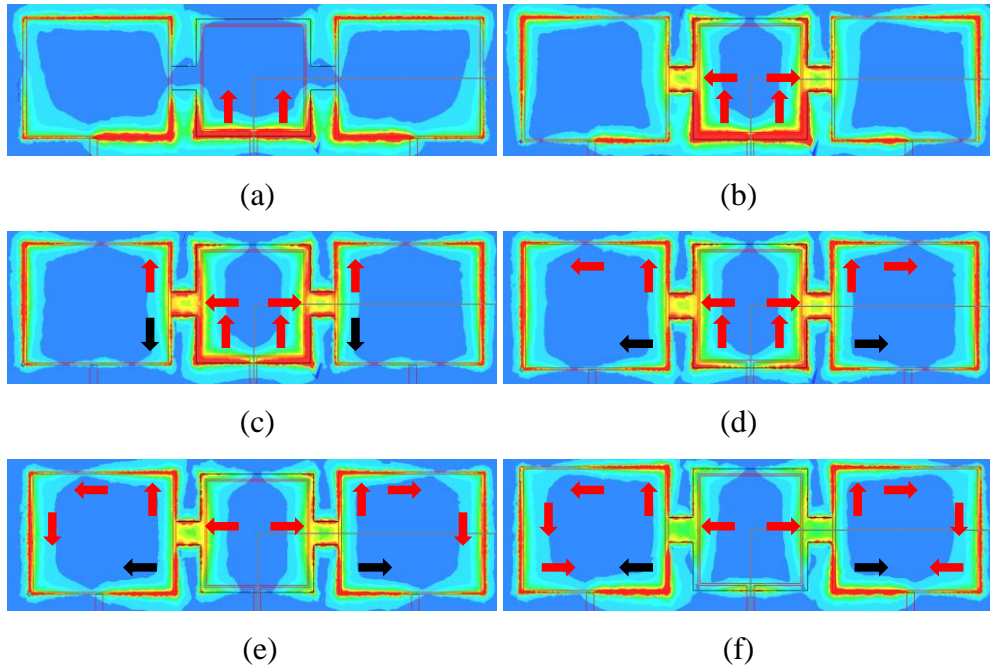


Figure 3.9: Wave fronts of the P_2 at 2.93 GHz captured at different snapshots when the slot resonator is supplied with a microwave signal source with phases of (a) 45° , (b) 105° , (c) 135° , (d) 150° , (e) 165° , and (f) 0° at the input port.

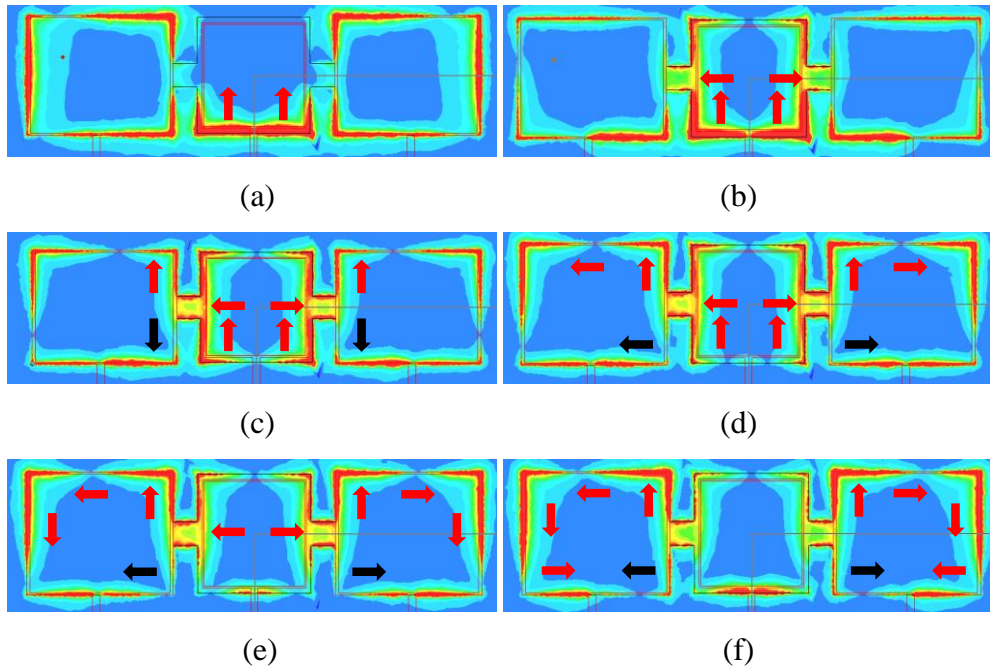


Figure 3.10: Wave fronts of P_3 at 3.83 GHz captured at different snapshots when the slot resonator is supplied with a microwave signal source with phases of (a) 90° , (b) 150° , (c) 180° , (d) 15° , (e) 30° , and (f) 45° at the input port.

One transmission zero is observed at 4.90 GHz (Z_2) with its magnetic field distribution shown in *Figure 3.11*. The frequency of the transmission zero can be

estimated by $f_{z1} = \frac{c}{A_{z1}\sqrt{\epsilon_{eff}}}$, where

$$2A_{z1} = 2[(L_3 + 2G_2) + (L_1 + 2G_1 + 2W_2)]$$

$$\therefore A_{z1} = (L_3 + 2G_2) + (L_1 + 2G_1 + 2W_2) \quad (3.5)$$

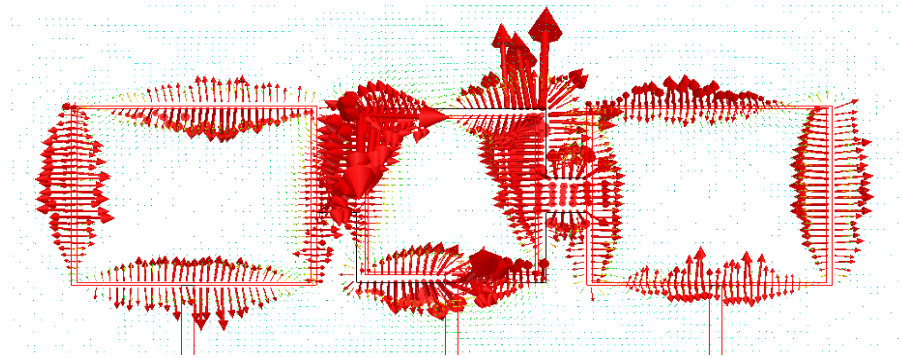


Figure 3.11: Magnetic field distributions of the proposed in-phase power divider at 4.90 GHz.

3.3 Out-of-phase Bandpassing Power Divider

3.3.1 Configuration

The configuration of the proposed out-of-phase bandpassing power divider will be illustrated in this section, with the schematic shown in *Figure 3.12*. Just like the in-phase power divider, the top surface of the substrate has three rings to excite three slots on the bottom. The only difference between the in-phase and out-of-phase power dividers is that the output port (Port 2) is tapped from a different position on

the left ring. And all rings are connected to the 50Ω microstrip feedlines. Also, this slot array is symmetric along $A - A'$ and $B - B'$. The detailed design parameters of the proposed out-of-phase power divider are given by $L_1 = 13.6\text{mm}$, $L_2 = 17.6\text{mm}$, $L_3 = 12.4\text{mm}$, $L_4 = 12\text{mm}$, $G_1 = 0\text{mm}$, $G_2 = 0.6\text{mm}$, $D_1 = 2.75\text{mm}$, $S_1 = 3\text{mm}$, $W_1 = 0.2\text{mm}$, $W_2 = 0.2\text{mm}$, $W_3 = 0.4\text{mm}$. Again, the circuit is shielded by a metallic cavity for reducing radiation. *Figure 3.13* shows the prototype for experiment.

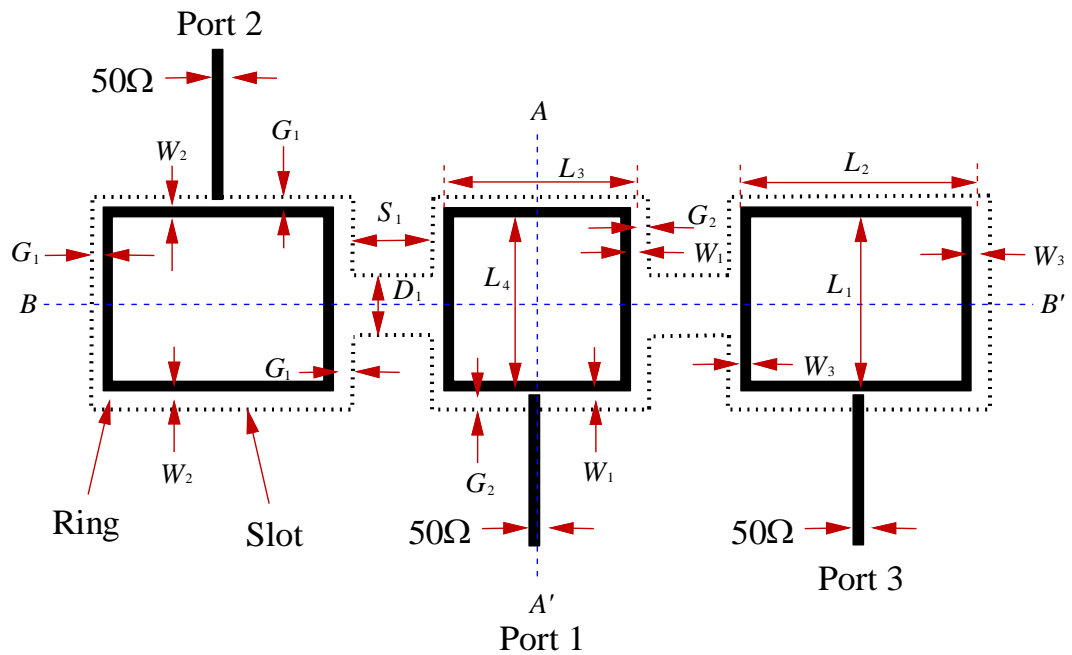


Figure 3.12: Schematic of the proposed out-of-phase power divider.

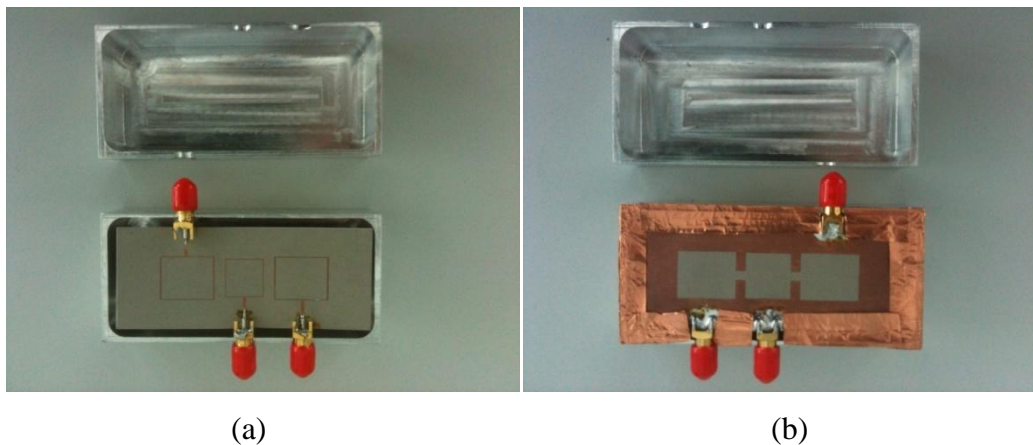
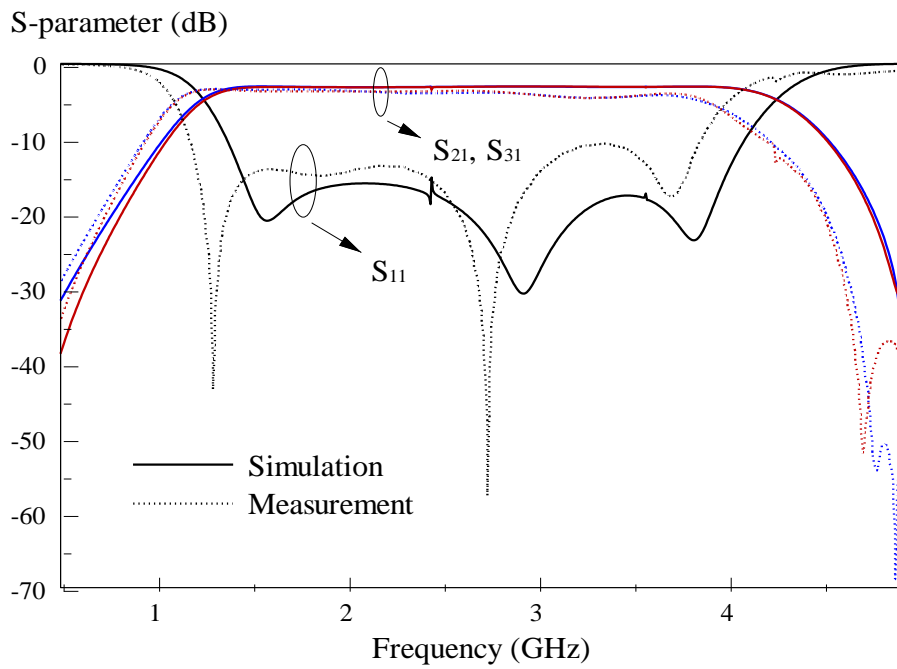


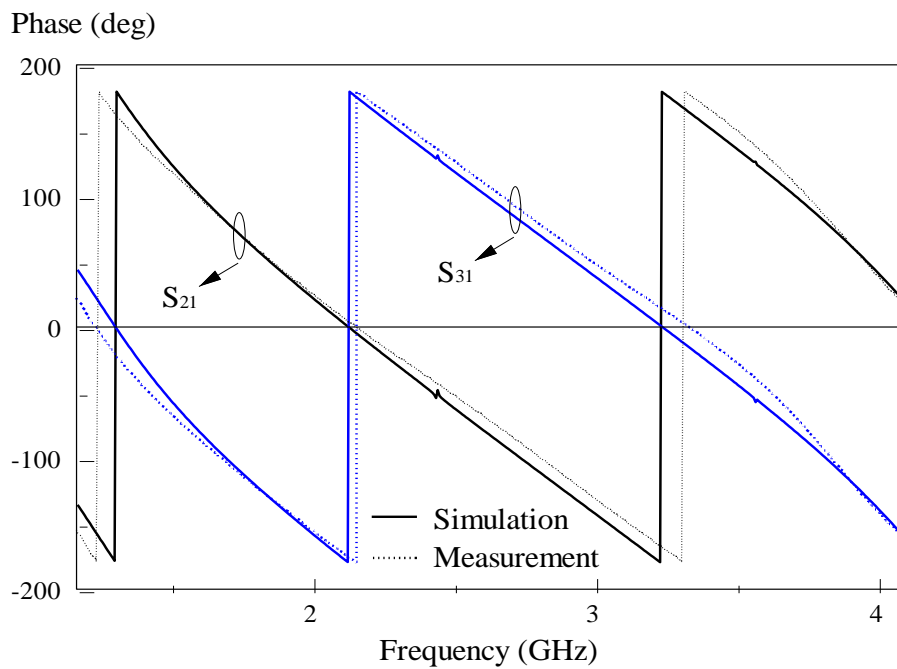
Figure 3.13: Photograph of the prototype: (a) Top view (b) Bottom view.

3.3.2 Simulation and Experimental Results

The amplitude and phase responses are shown in *Figure 3.14*. It can be seen that the experimental and simulated results agree reasonably well. Broad bandwidth has been formed by the three resonances, which can be seen in simulation. Besides that, the selectivity is improved by introducing transmission zeroes near to the cutoff frequencies. The out-of-phase power divider has a fractional bandwidth of 99.63% with a passband covering 1.37 - 4.09 GHz in simulation. The measured result is slightly larger than the simulated one with a fractional bandwidth of 106.35% and an operating frequency range of 1.18-3.86 GHz. As observed in *Figure 3.14(b)*, the two output signals are 180° out-of-phase. Amplitude imbalance and phase difference can be calculated ($|\angle S_{21} - \angle S_{31}|$) from the measured output phases are less than 1-dB and 6°, respectively, as shown in *Figure 3.15*. The isolation (*Figure 3.16*) between the two outputs is around -6-dB - -7-dB. With reference to *Figure 3.17*, the group delay gives a constant value of ~0.5 ns in the passband. This implies that the input signal reaches the two output ports at the same time, leading to minimum signal distortion.



(a)



(b)

Figure 3.14: Measured and simulated (a) amplitude response, (b) phase response of the out-of-phase power divider.

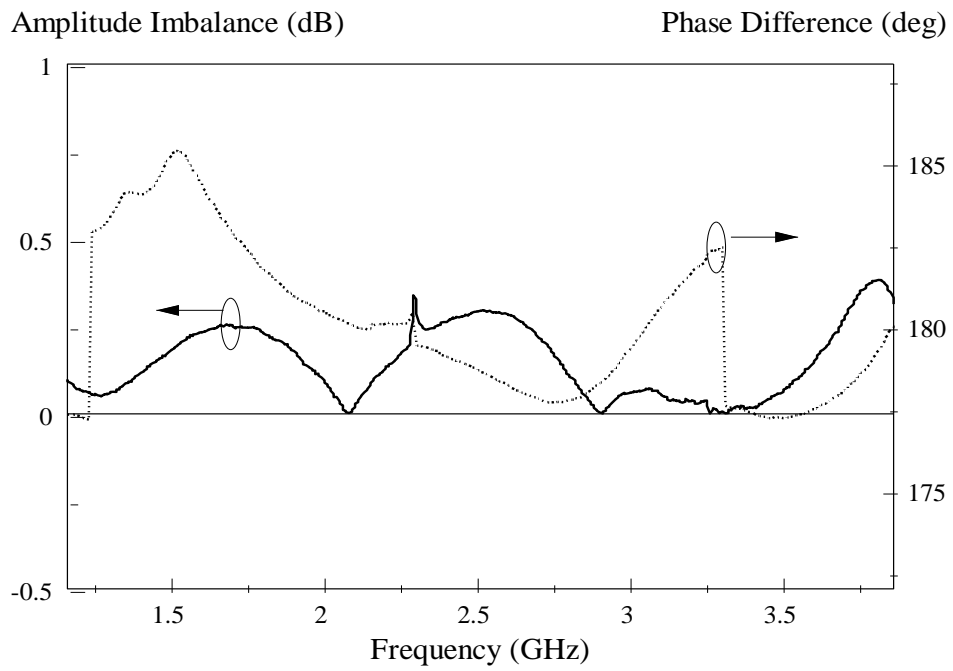


Figure 3.15: Calculated amplitude imbalance and phase difference of the out-of-phase power divider.

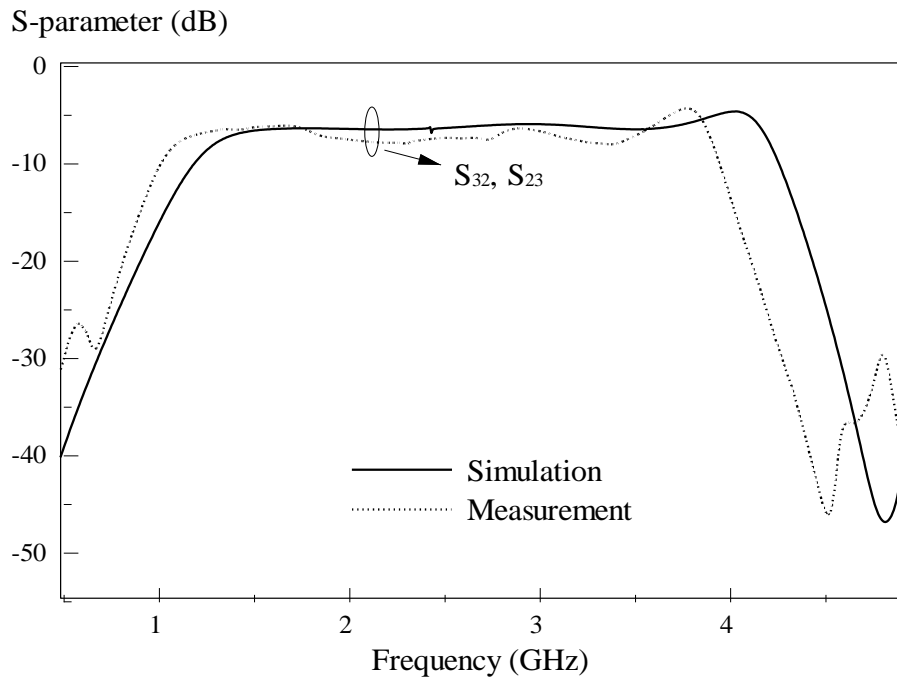


Figure 3.16: Measured and simulated isolation curves between the output ports of the out-of-phase power divider.

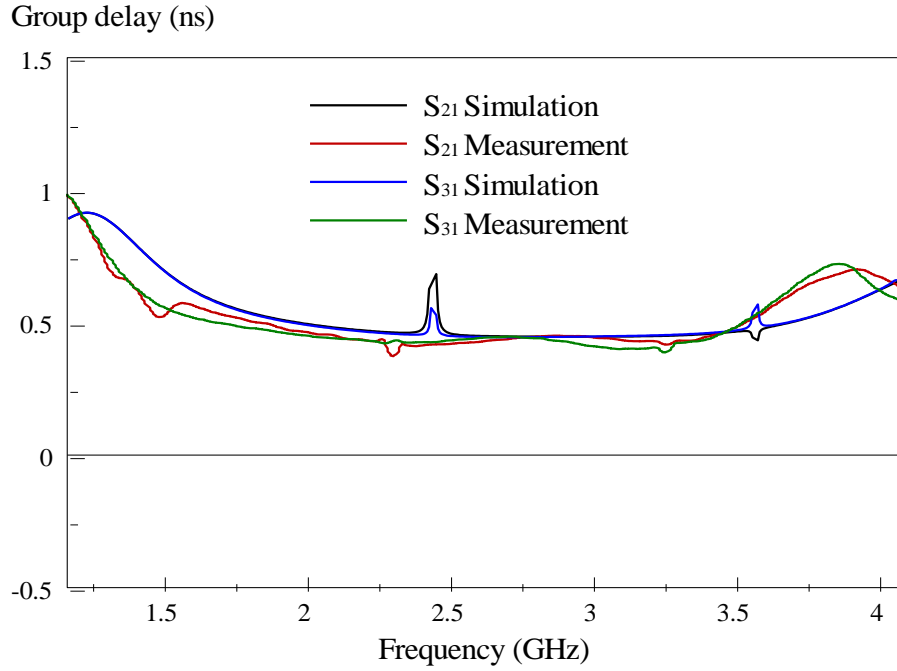
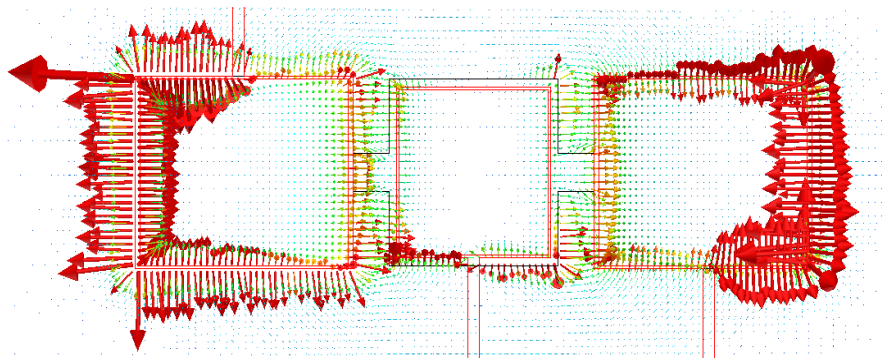


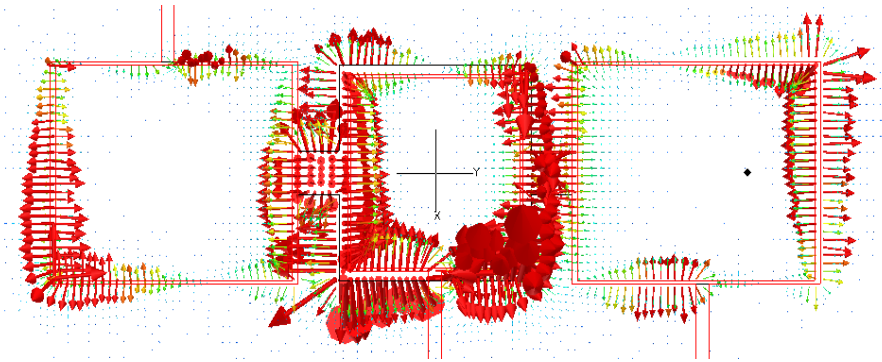
Figure 3.17: Measured and simulated group delays.

3.3.3 Resonances and Field Characteristics

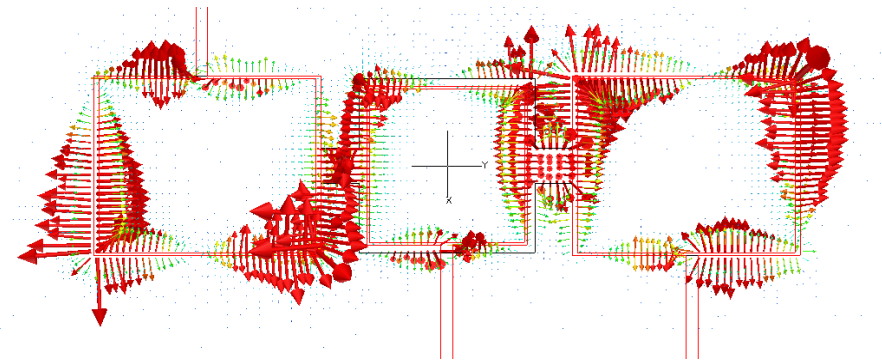
The magnetic field distributions of the proposed out-of-phase power divider are discussed in this section. The simulated reflection coefficient has three poles at 1.59 GHz (P_1), 2.94 GHz (P_2), and 3.80 GHz (P_3), which are shown in *Figure 3.14(a)*. *Figure 3.18(a) - (c)* show their corresponding magnetic field distributions, which are quite similar to those in *Figure 3.7*. The out-of-phase power divider has almost the same pole frequencies with the in-phase one. Therefore, (3.1)- (3.4) can also be used to calculate the resonant frequencies of the out-of-phase power divider.



(a)



(b)



(c)

Figure 3.18: Magnetic field distributions of the proposed out-of-phase power divider at (a) 1.59 GHz, (b) 2.94 GHz, (c) 3.80 GHz.

Magnetic fields at different snapshots are studied for the slot resonator in *Figure 3.12* in order to visualize the wave propagation. In *Figure 3.19*, the slot resonator is supplied with a signal source with different phases of 0° , 30° , 60° , 90° , 120° , and 150° at the input port for the P_1 at 1.59 GHz. Again, it is proven that the slot is a travelling-wave resonator. Similar characteristics are observed in *Figure 3.20* and *3.21* for the P_2 and P_3 .

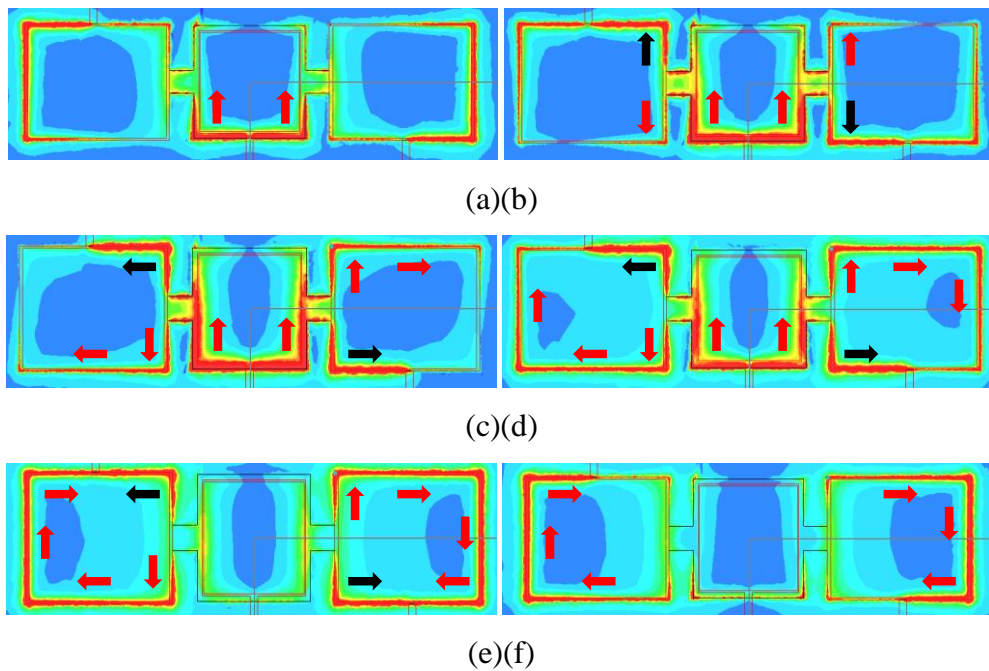


Figure 3.19: Wave fronts of P_1 at 1.58 GHz captured at different snapshots when the slot resonator is supplied with a microwave signal source with phases of (a) 0° , (b) 30° , (c) 60° , (d) 90° , (e) 120° , and (f) 150° at the input port.

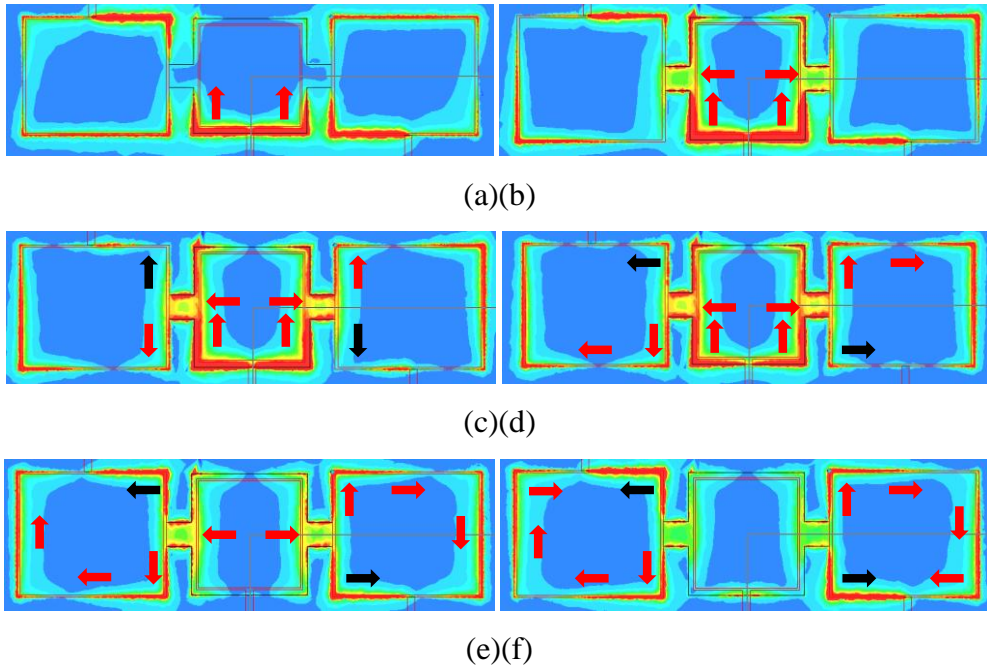


Figure 3.20: Wave fronts of P_2 at 2.93 GHz captured at different snapshots when the slot resonator is supplied with a microwave signal source with phases of (a) 45° , (b) 90° , (c) 120° , (d) 135° , (e) 165° , and (f) 180° at the input port.

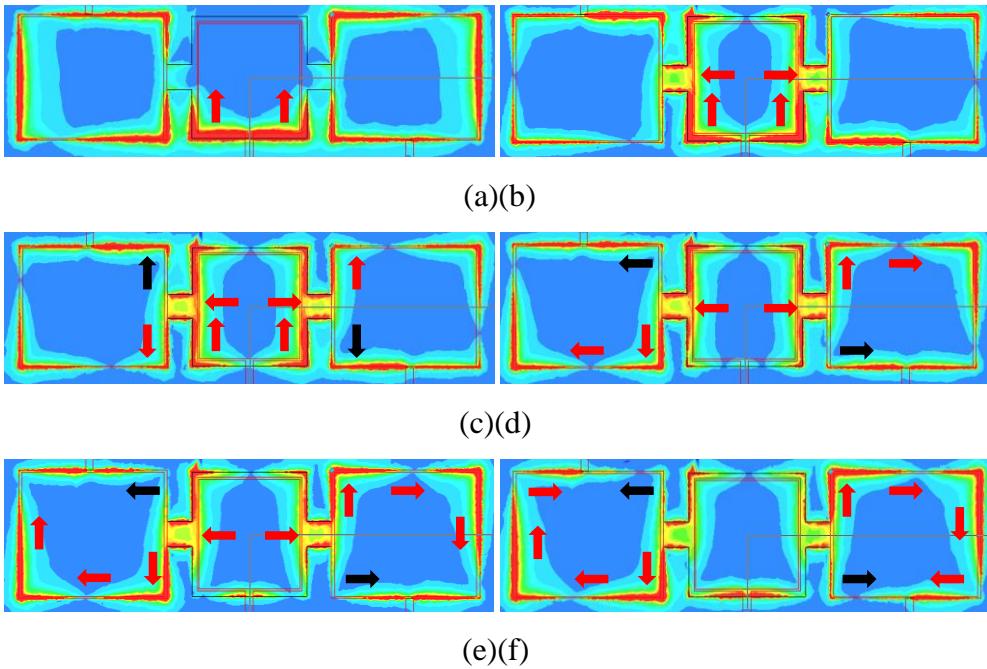


Figure 3.21: Wave fronts of P_3 at 3.80 GHz captured at different snapshots when the slot resonator is supplied with a microwave signal source with phases of (a) 90° , (b) 165° , (c) 180° , (d) 15° , (e) 30° , and (f) 45° at the input port.

One transmission zero is observed at 4.90 GHz(Z_2) with its magnetic field distribution shown in *Figure 3.22*. It can be estimated by using (3.5) as well.

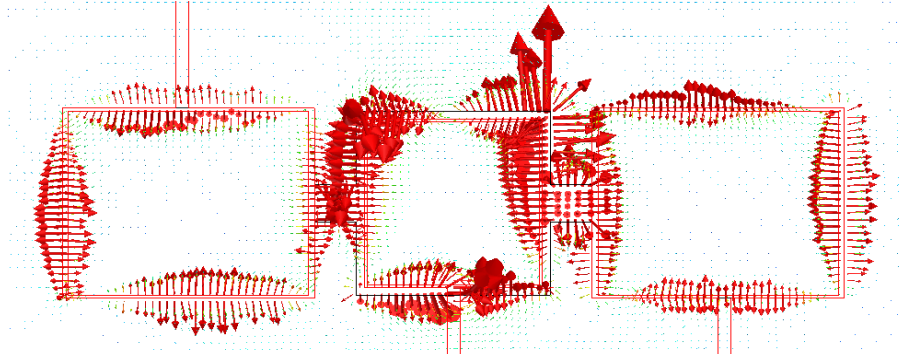


Figure 3.22: The electric field distributions of the proposed out-of-phase power divider at 4.90 GHz.

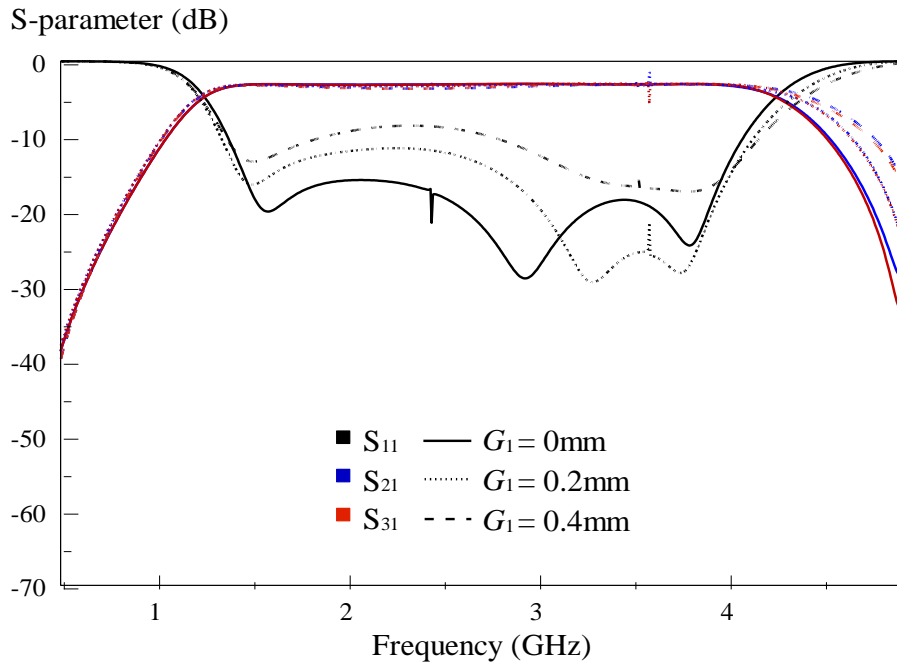
3.4 Parametric Analysis

A complete parametric analysis has been performed on the in-phase and out-of-phase power dividers. The effects of the design parameters such as those for the slot array and the ring excitors will be studied in this section. It has been found that all pole and zero resonating modes can be kept for most cases and matched with (3.2)-(3.5).

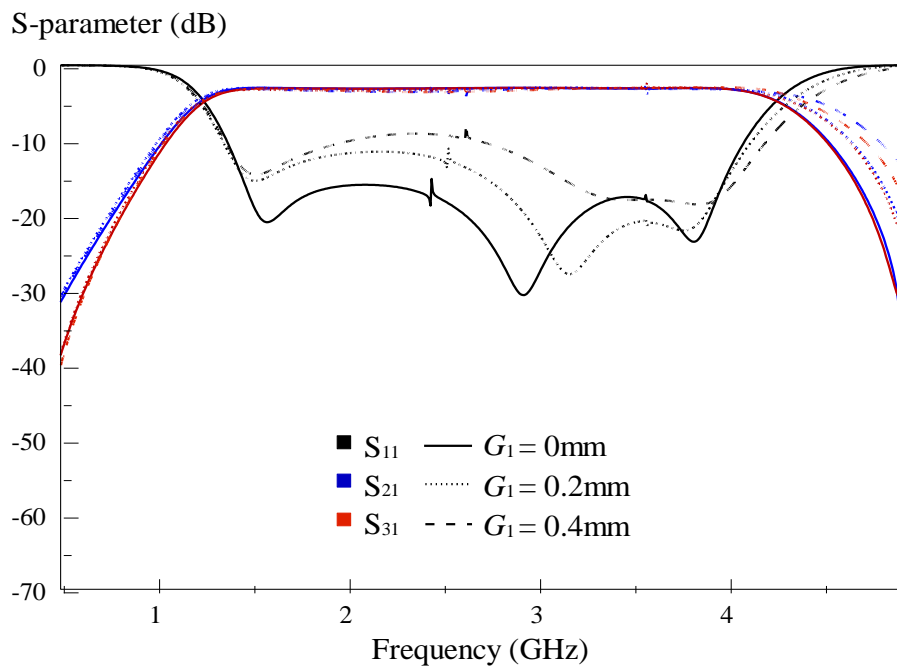
3.4.1 Gaps: G_1 and G_2

First, the effect of G_1 is studied for the in-phase and out-of-phase power dividers. It can be seen from *Figure 3.23* that the P_2 increases from 2.95 GHz to beyond 3.30 GHz when the gap separation is made slightly larger from 0mm to 0.4mm. It is not match with the (3.2). The same trend is observed for the Z_1 near to the upper cutoff frequency, which goes higher (from 4.95 GHz - 5.20 GHz) when varying the same parameter. Also, worth mentioning is that the operating frequencies of P_1 and P_3 remain unchanged. This is very positive as it implies that these two resonances can be tuned independently without affecting others. The gap G_1 is one of the crucial design parameters as it can be seen from *Figure 3.8 - 3.10* (in-phase power divider) and *Figure 3.19 - 3.21* (out-of-phase power divider) that magnetic fields travel along the gaps.

Referring to *Figure 3.24*, the gap G_2 slightly affects the positions of poles in the reflection coefficient, with all of them kept below -15 -dB. For both power dividers, the impedance matching of P_1 deteriorates when G_2 is reduced. But that for the P_3 gets improved when G_2 goes smaller. The roll-off performance at the lower and upper cutoff frequencies are slightly improved when G_2 is increased from 0.4mm to 0.8 mm. G_2 is an important design parameter because it is close to the input port.

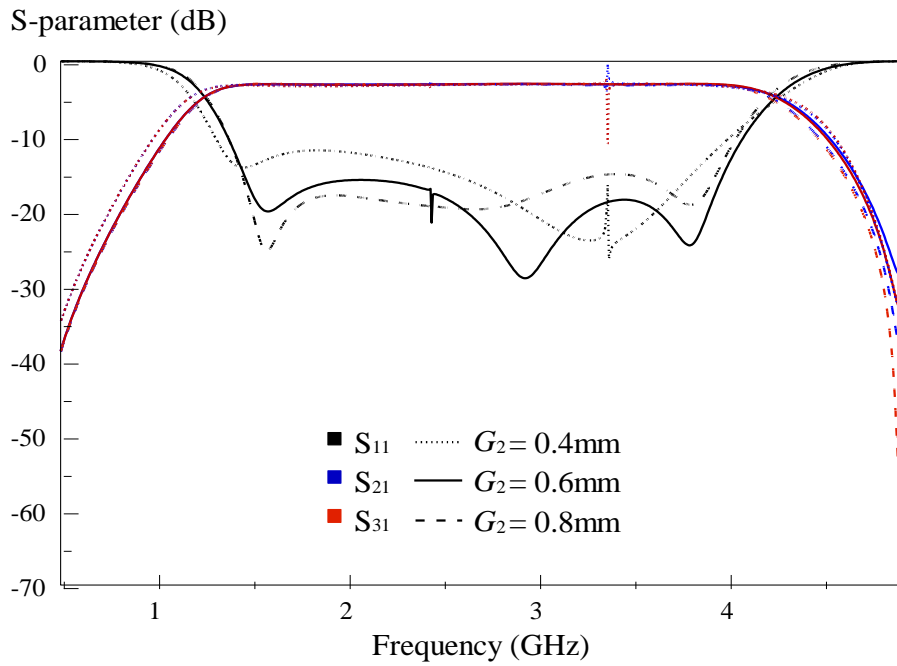


(a)

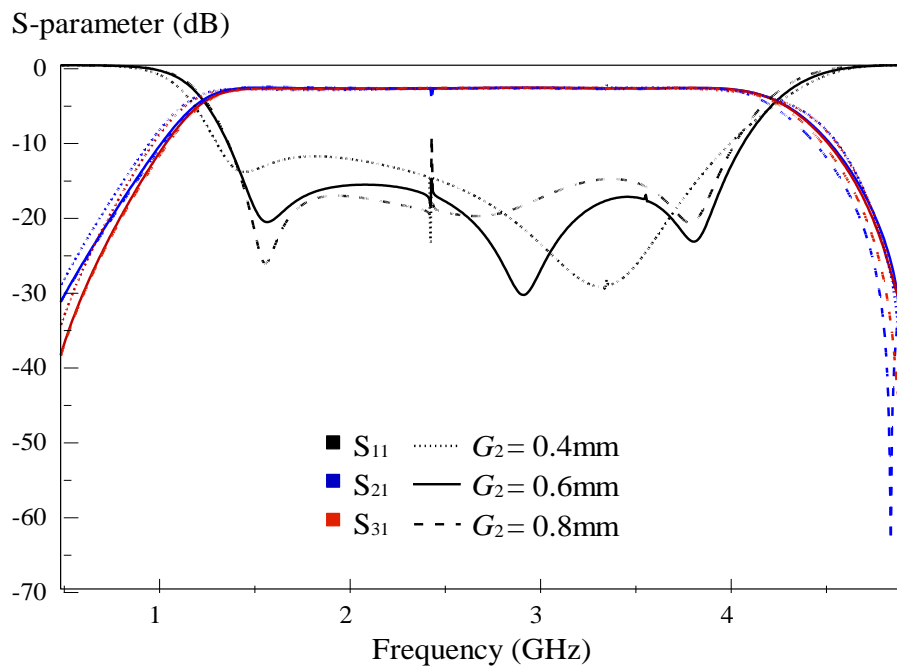


(b)

Figure 3.23: Amplitude responses of the (a) in-phase power divider and (b) out-of-phase power divider when G_1 is varied.



(a)



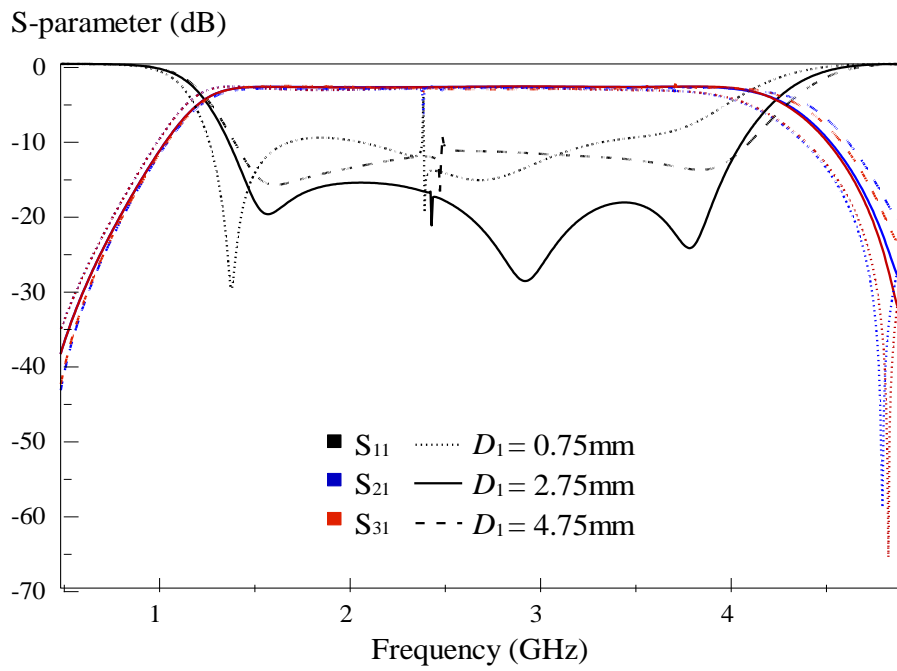
(b)

Figure 3.24: Amplitude responses of the (a) in-phase power divider and (b) out-of-phase power divider when G_2 is varied.

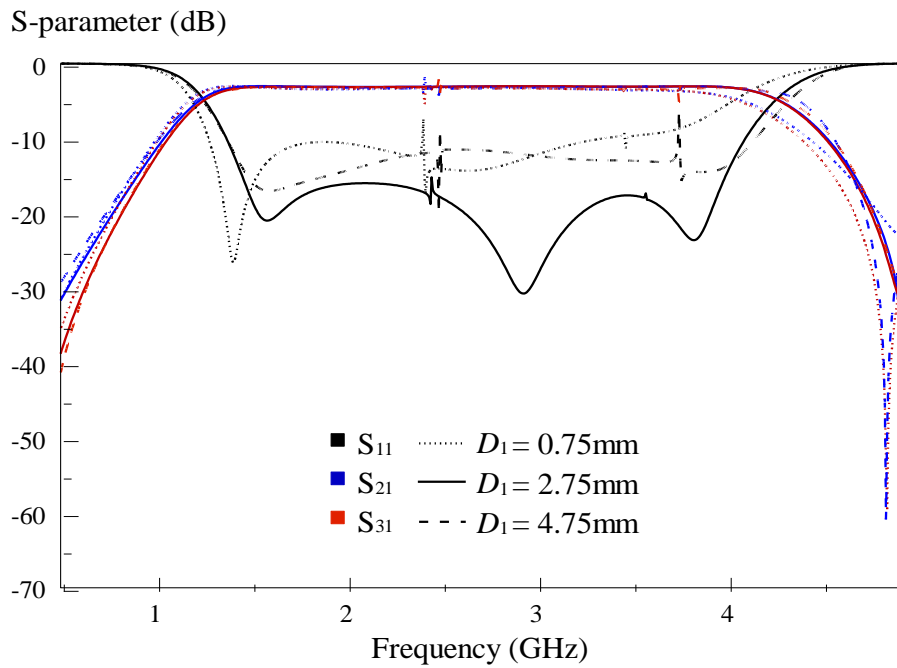
3.4.2 Interconnecting Slots: D_1 and S_1

With reference to *Figure 3.1* and *3.12*, the three rectangular slots are interconnected by two narrow slots to enable the passage of electromagnetic signal. The effect of these interconnecting slots is studied here. *Figure 3.25* shows the transmission and reflection coefficients of the proposed in-phase and out-of-phase power dividers. The impedance matching is seriously degraded when the slot width D_1 is varied. As observed in *Figure 3.25*, the optimal D_1 gives three nearly equidistant resonance poles. This makes the impedance matching good across the entire passband.

Next, the length S_1 of the interconnecting slots is explored. As can be seen from *Figure 3.26*, this design parameter does not bring any significant change to both of the proposed power dividers. It only slightly affects the impedance matching of P_2 and P_3 .

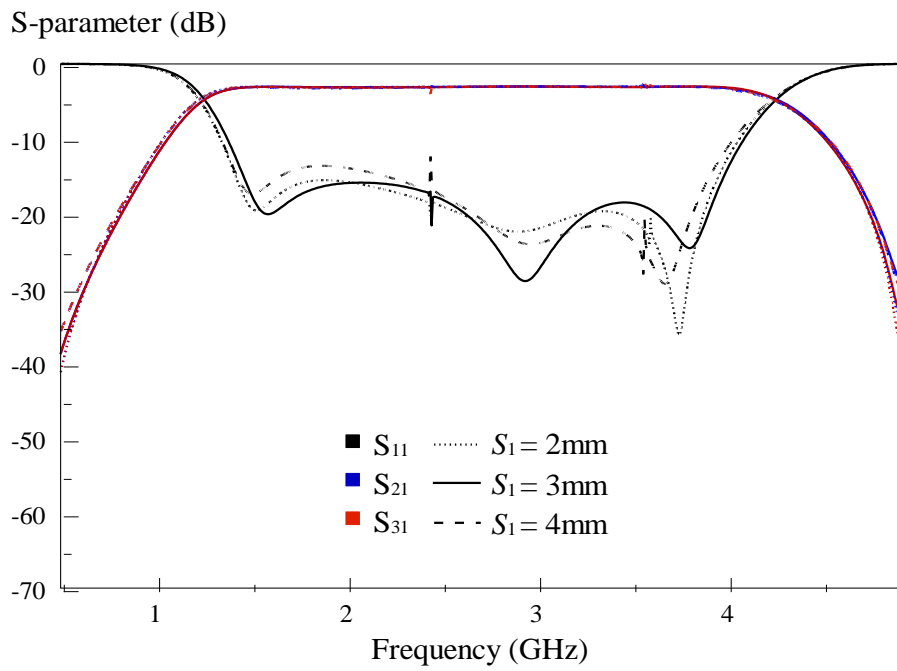


(a)

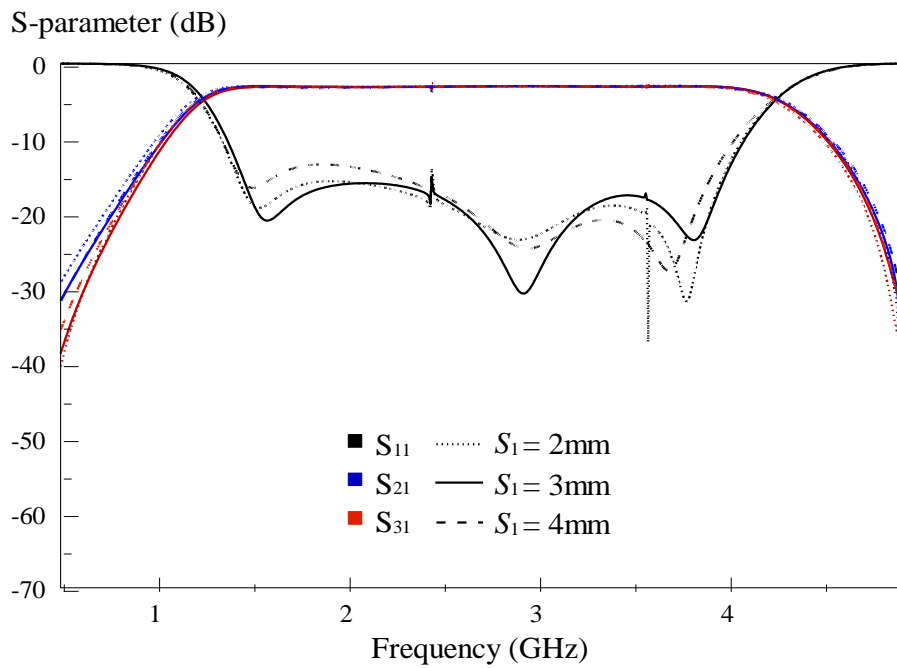


(b)

Figure 3.25: Amplitude responses of the (a) in-phase power divider and (b) out-of-phase power divider when D_1 is varied.



(a)



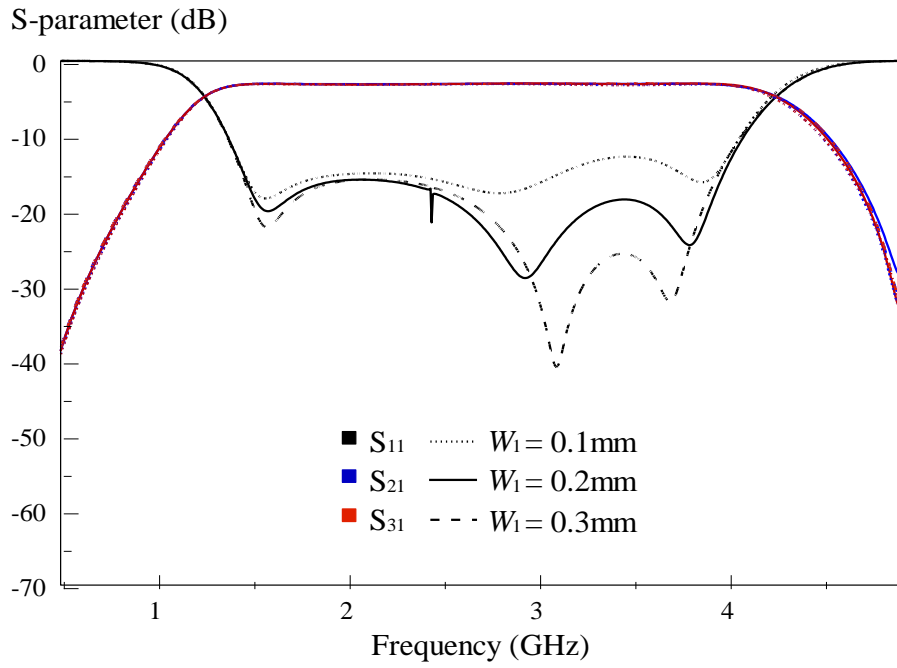
(b)

Figure 3.26: Amplitude responses of the (a) in-phase power divider and (b) out-of-phase power divider when S_1 is varied.

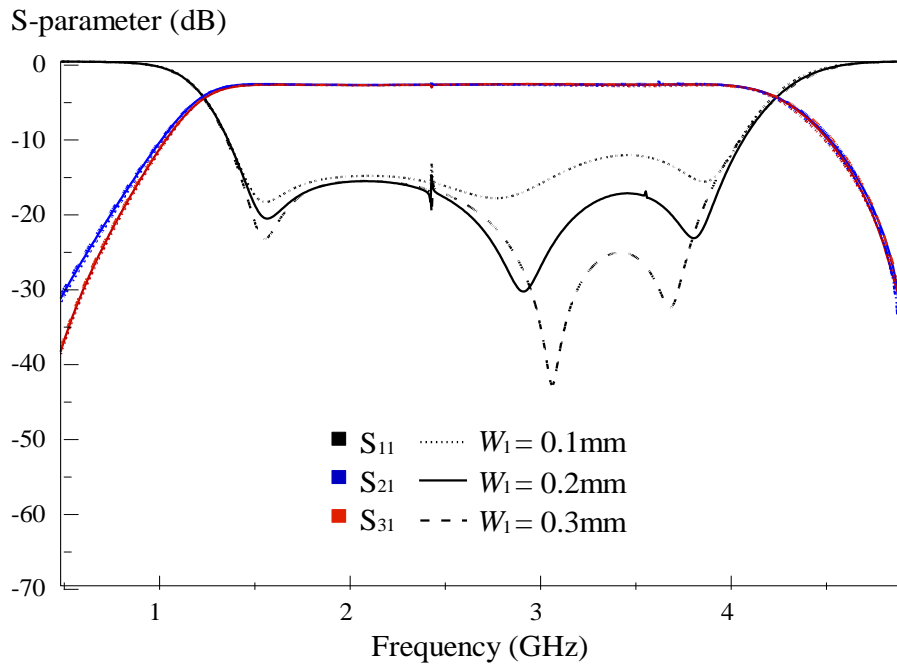
3.4.3 Coupling Rings: W_1 , W_2 and W_3

The effects of the coupling rings are studied in *Figure 3.27 – 3.29*. With reference to *Figure 3.1* and *3.12*, it can be seen that the center ring has an equal width W_1 in all the arms. On the other hand, the two side rings are equal but have different dimensions in their horizontal (W_2) and vertical (W_3) arms. First, the parameter W_1 is varied from 0.1 mm to 0.3 mm and the S-parameters are investigated. For both the in-phase and out-of-phase cases, P_2 sees a frequency shift from ~2.80 GHz to ~3.10 GHz, increasing with the width; while P_3 decreases from ~3.90 GHz to ~3.70 GHz. It can be useful for tuning the impedance matching for the abovementioned two poles. P_1 is not affected by any change in the arm width.

Next, the horizontal arm width (W_2) is analyzed. As can be seen from its amplitude imbalance, P_2 does not show any significant effect, it moves from ~2.85 GHz to ~2.95 GHz when the width is increased. However, the P_3 slides down from ~3.99 GHz to ~3.64 GHz. The P_2 pole combines with the P_3 pole when the width is set to be 0.3mm. The vertical arm width (W_3) of the side ring is also analyzed. It causes the resonating frequency of P_2 to become lower but that for P_3 to have a higher value. It is interesting to note that the two poles come together at ~3.37 GHz when the width is set at 0.2 mm.

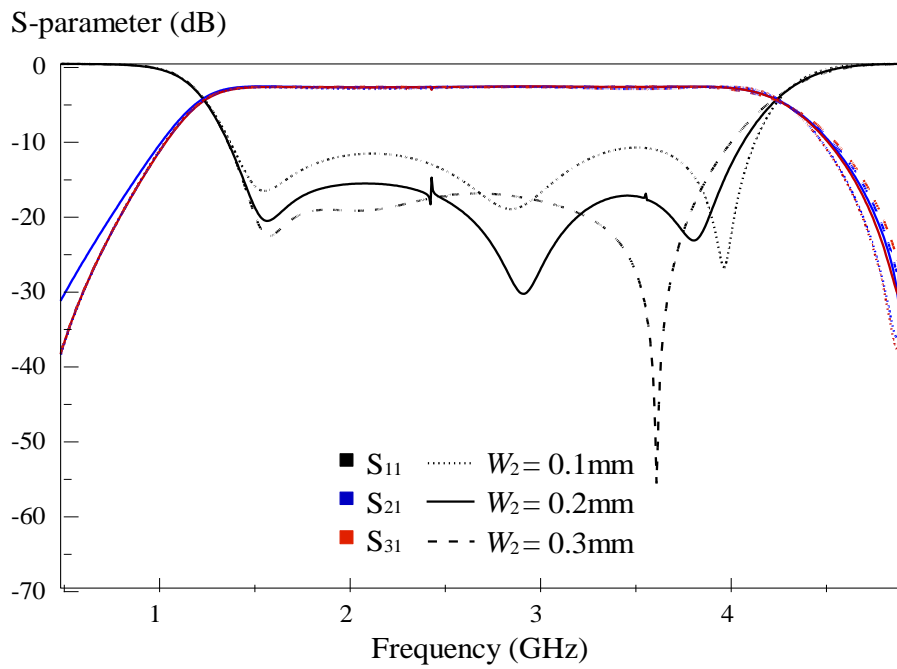


(a)

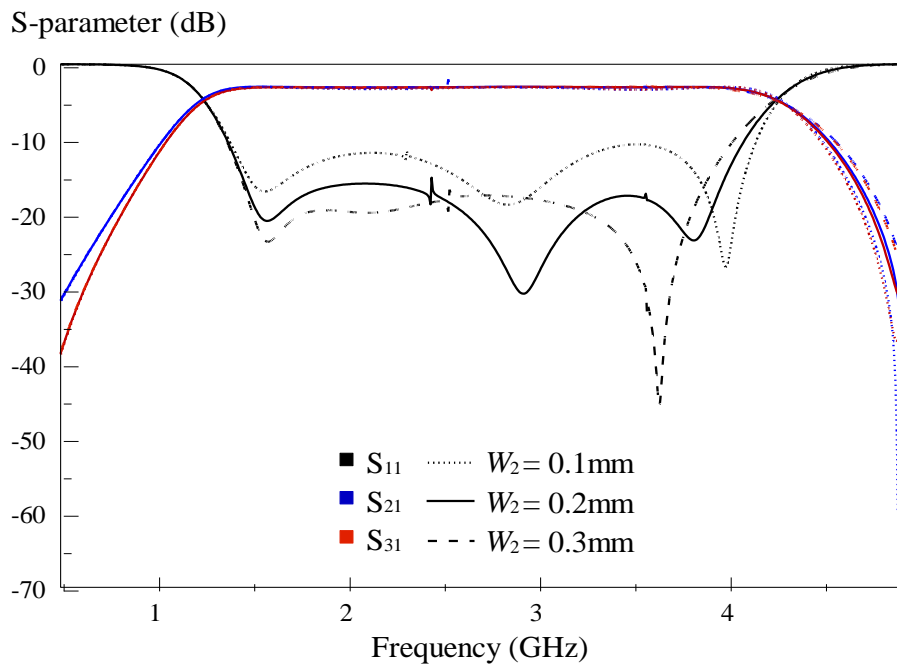


(b)

Figure 3.27: Amplitude responses of the (a) in-phase power divider and (b) out-of-phase power divider when W_1 is varied.

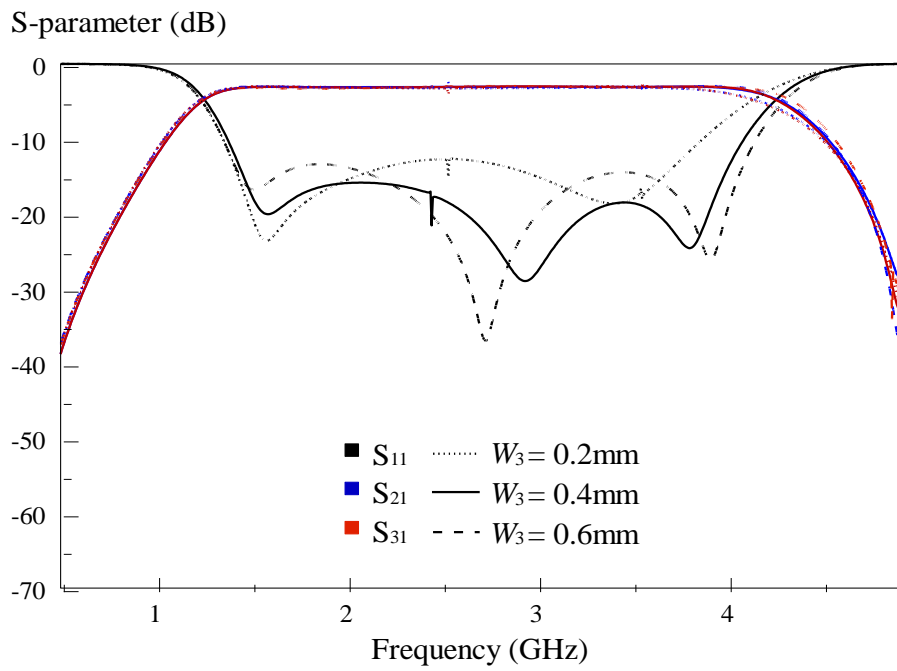


(a)

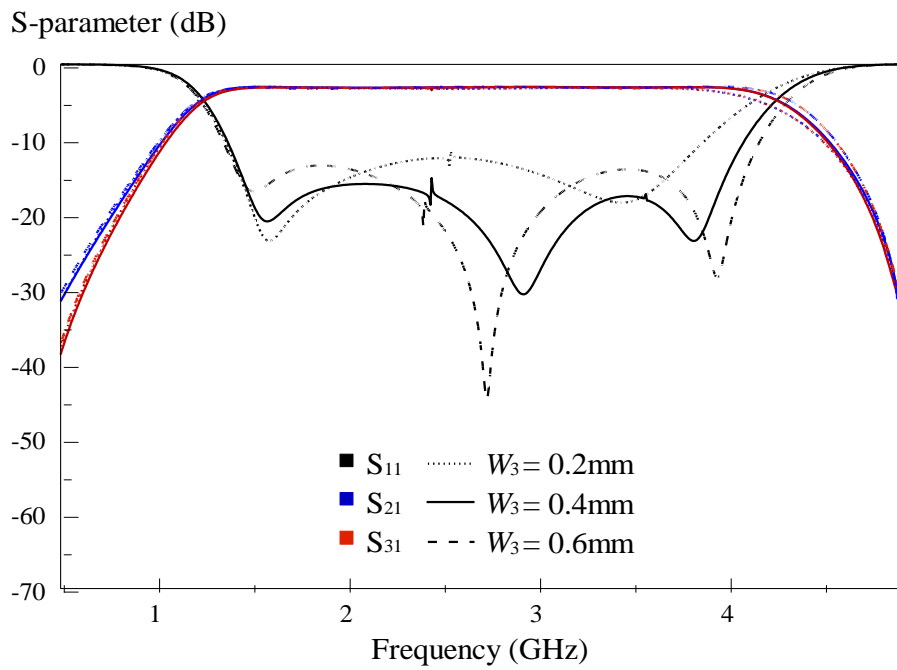


(b)

Figure 3.28: Amplitude responses of the (a) in-phase power divider and (b) out-of-phase power divider when W_2 is varied.



(a)



(b)

Figure 3.29: Amplitude responses of the (a) in-phase power divider and (b) out-of-phase power divider when W_3 is varied.

3.5 Reconfigurable Bandpassing Power Divider

3.5.1 Configuration

A reconfigurable power divider will be demonstrated in this section. It combines the previously mentioned in-phase and out-of-phase power dividers into one piece, as shown in *Figure 3.30*. As can be observed in the figure, several RF PIN diodes are incorporated with each output feedlines for performing switching function. The resulted reconfigurable power divider has four ports - Port 1 is the input port while Ports 2 - 4 are the output. It functions as an in-phase power divider when the diodes on the feedlines of Ports 3 - 4 are turned ON, with Port 2 diode set in OFF state. On the other hand, it can be configured as an out-of-phase power divider when the diodes for Ports 2 - 3 are ON while for Port 4 is OFF. The optimized design parameters for the proposed reconfigurable power divider are exactly the same as those in Section 3.3 - 3.4 given by $L_1 = 13.6\text{mm}$, $L_2 = 17.6\text{mm}$, $L_3 = 12.4\text{mm}$, $L_4 = 12\text{mm}$, $G_1 = 0\text{mm}$, $G_2 = 0.6\text{mm}$, $D_1 = 2.75\text{mm}$, $S_1 = 3\text{mm}$, $W_1 = 0.2\text{mm}$, $W_2 = 0.2\text{mm}$, $W_3 = 0.4\text{mm}$. As can be seen in *Figure 3.30*, a small stub with length L_5 is attached to the right ring for phase tuning. Also, a metallic cavity was used as a shield to minimize radiation. The prototype of the proposed reconfigurable power divider is shown in *Figure 3.31*.

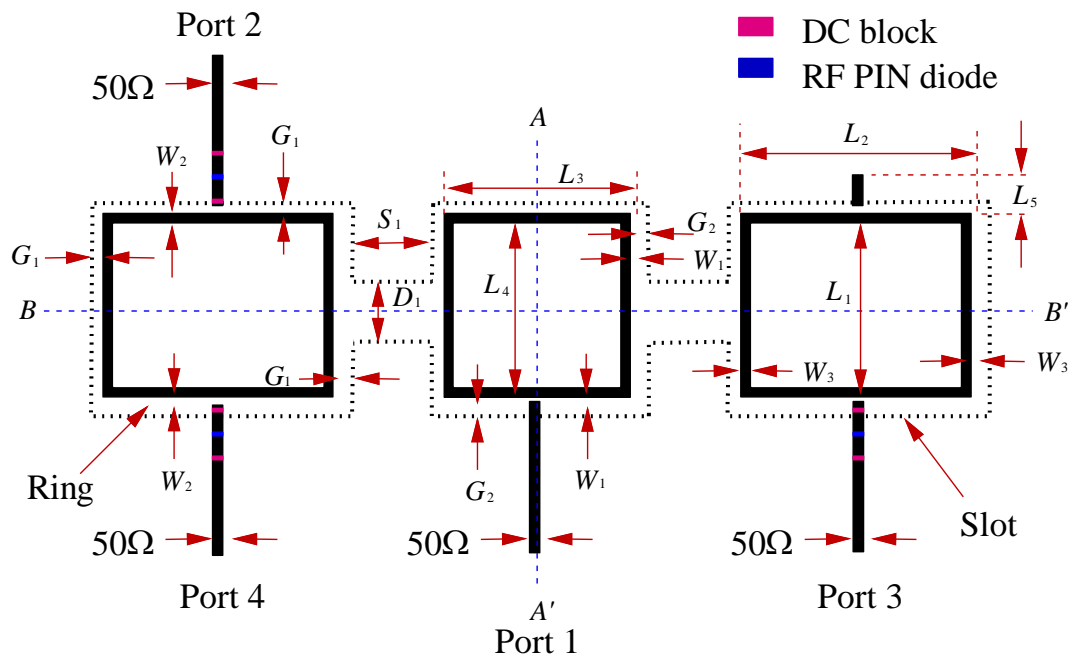


Figure 3.30: Schematic of the proposed reconfigurable power divider.

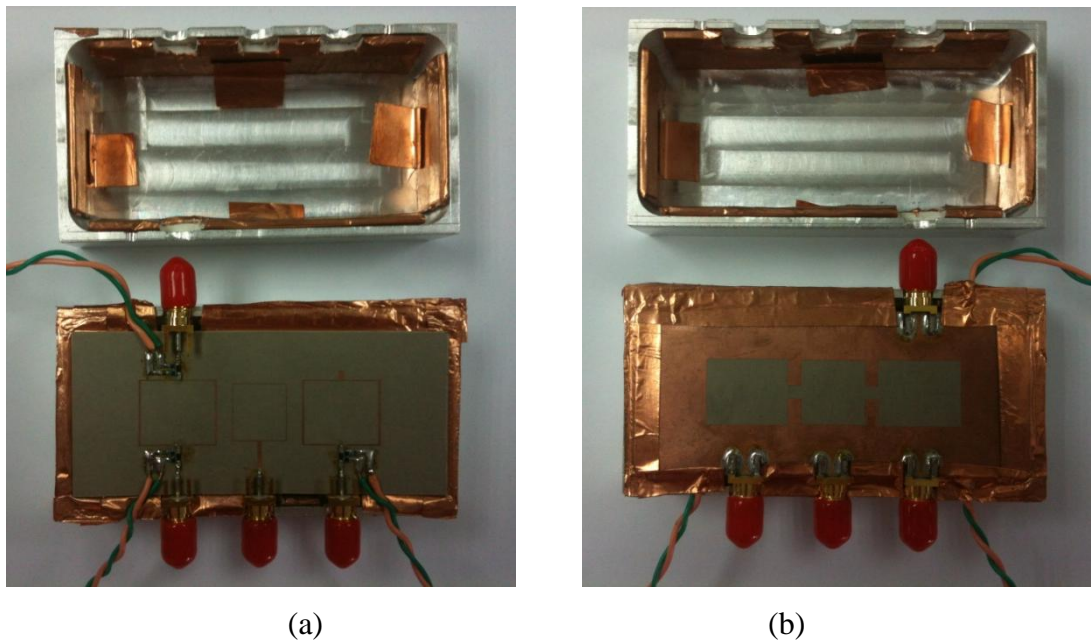


Figure 3.31: Photograph of the prototype of the proposed reconfigurable power divider: (a) Top view.(b) Bottom view.

3.5.2 Biasing Circuitry for RF PIN Diode

RF PIN diode is a semiconductor device that operates as a switch at RF and microwave frequencies. When applied with a forward-biased voltage, the diode is turned ON to work as a good RF conductor. At this state, it has very low loading resistance ($\sim 1\Omega$), resulting in minimum loss. Conversely, the diode causes the switch to be OPEN when it is in reverse-biased condition. In this case, it is equivalent to a small capacitance that disallows RF signal to pass through. This is crucial for achieving high isolation. There many types of RF PIN diodes in the market that can provide different operating frequencies, biasing points, isolation levels, and insertion losses in market.

In this project, the BAR50-02V RF PIN diodes are incorporated with the 50Ω microstrip feedlines for achieving reconfiguration. This diode is chosen because it can provide good performances at 2.4 GHz. It was also found from the specifications that the insertion loss at 4GHz is as low as -0.15 -dB with an isolation level of ~ -14 -dB at OFF stage, which are sufficient for both the proposed in-phase and out-of-phase power dividers. The biasing circuit of the RF PIN diode is shown in *Figure 3.32*. As observed in the biasing circuit, two RF chokes are used to prevent RF signal leakage into the DC path; while two DC blocks are used to block the DC current from flowing into the input and output ports. In simulation, the diode is simply replaced by a lumped resistor (1.5Ω at 100mA, from datasheet) when working at ON state. On the other hand, it will be left open when it is OFF.

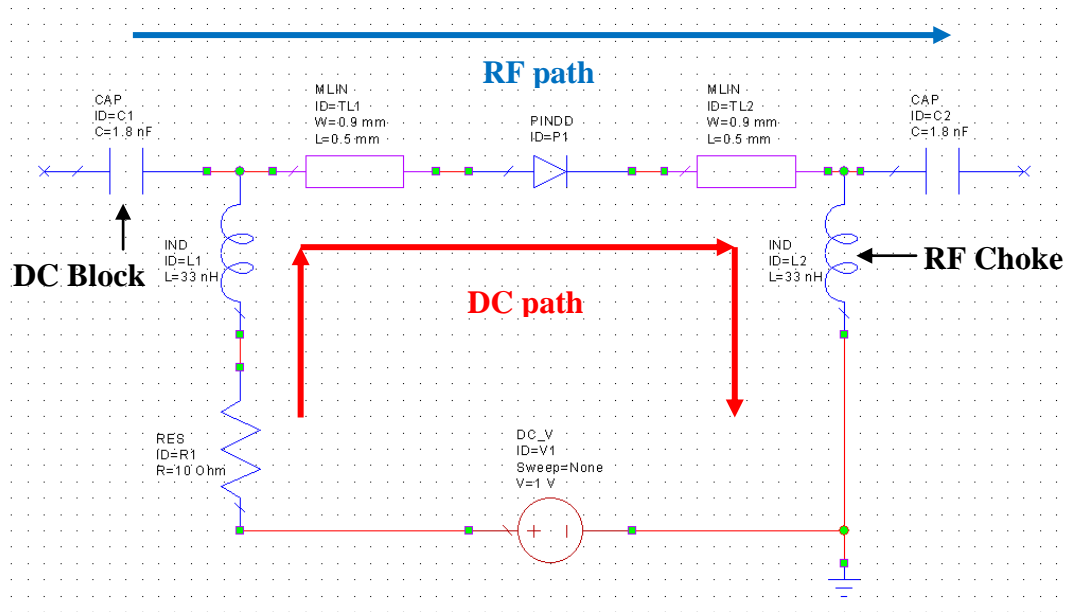
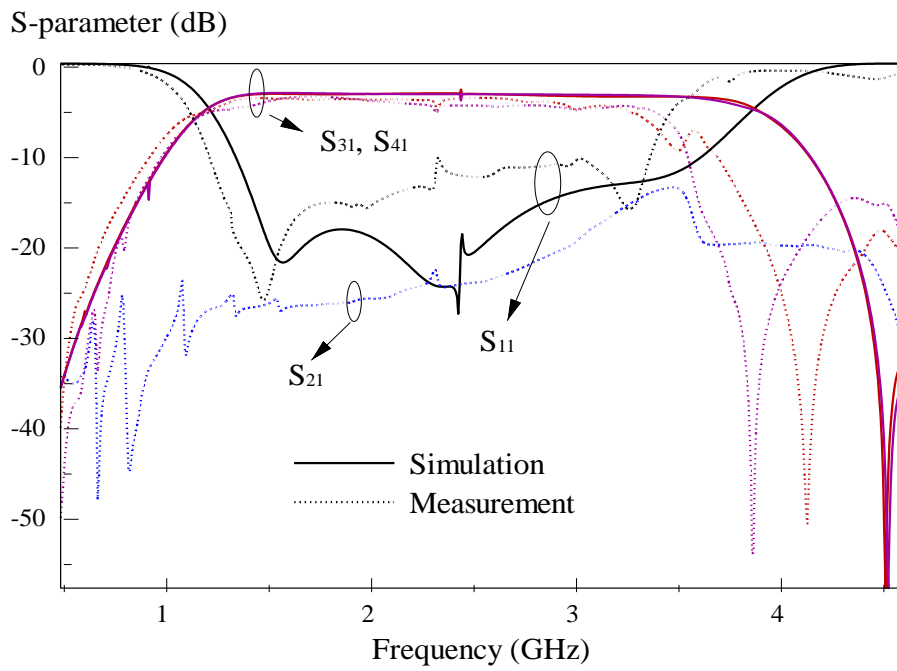


Figure 3.32: Biasing Circuit for the RF PIN Diode.

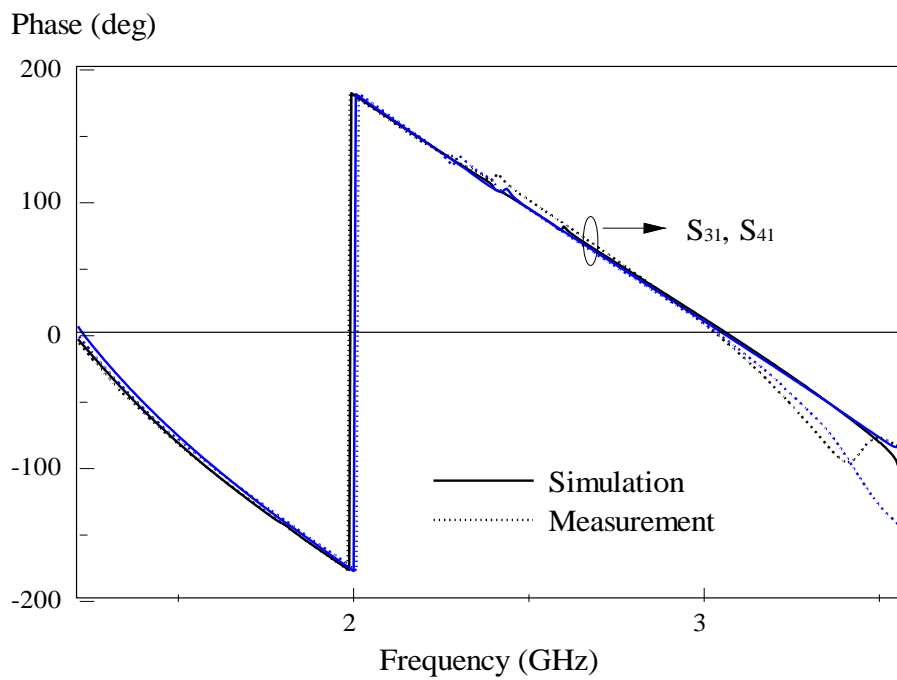
3.5.3 Simulation and Experimental Results

First, the power divider is configured to give in-phase output signals by turning ON the diodes on the feedlines of Ports 3 - 4 while that for Port 2 is turned OFF. It can be seen in *Figure 3.33* that the experimental results for the amplitude and phase responses agree reasonably well with their simulations. Three resonating poles are observed in the frequency passband, being very close to that in the passive case. It has a measured fractional bandwidth of 93.27% (simulation: 91.78%), covering 1.23 - 3.38 GHz (simulation: 1.35 - 3.64 GHz). Better selectivity has been achieved with the availability of transmission zeros at 4.14 GHz at Port 3, and 3.88 GHz at Port 4 shaping the roll-off skirts near to the upper cutoff frequencies. Working as an in-phase power divider with Port 2 disconnected, with reference to *Figure 3.33(a)*, an

isolation level (S_{21}) of below -16 -dB is achievable. It implies that this diode is cutting off Port 2 from the resonator pretty well around 2.4 GHz. *Figure 3.33(b)* depicts the measured and simulated output phases ($\angle S_{31}$ and $\angle S_{41}$), showing good agreement. The input power given to Port 1 is equally divided into the two output ports (Port 3 and 4) with amplitude and phase imbalances of less than 1.5-dB and 6° , respectively, across the passband, as can be seen in *Figure 3.34*.



(a)



(b)

Figure 3.33: Measured and simulated (a) amplitude response, (b) phase response of the reconfigurable in-phase power divider.

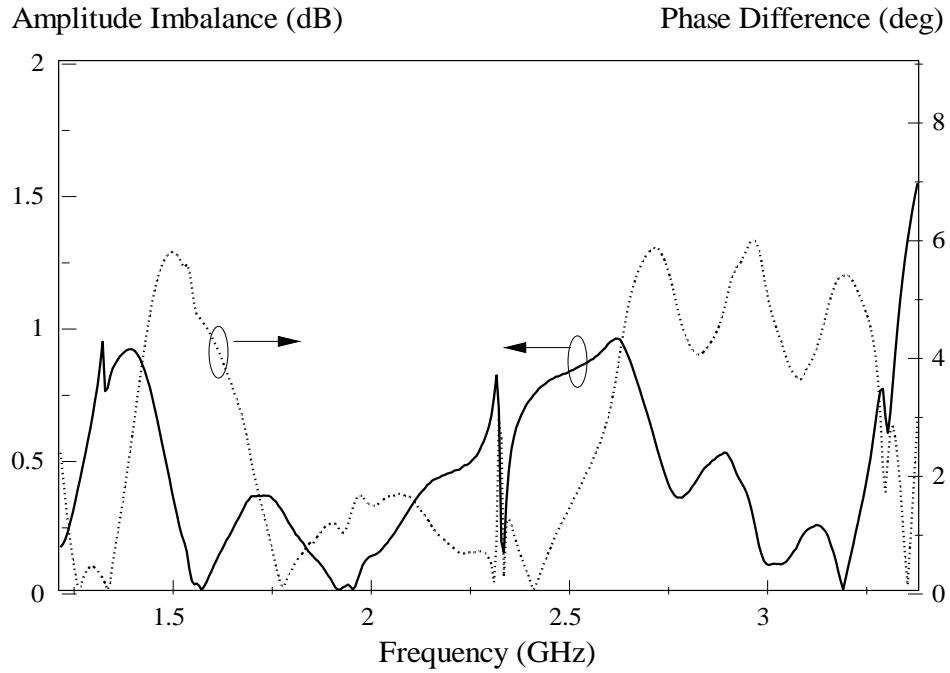
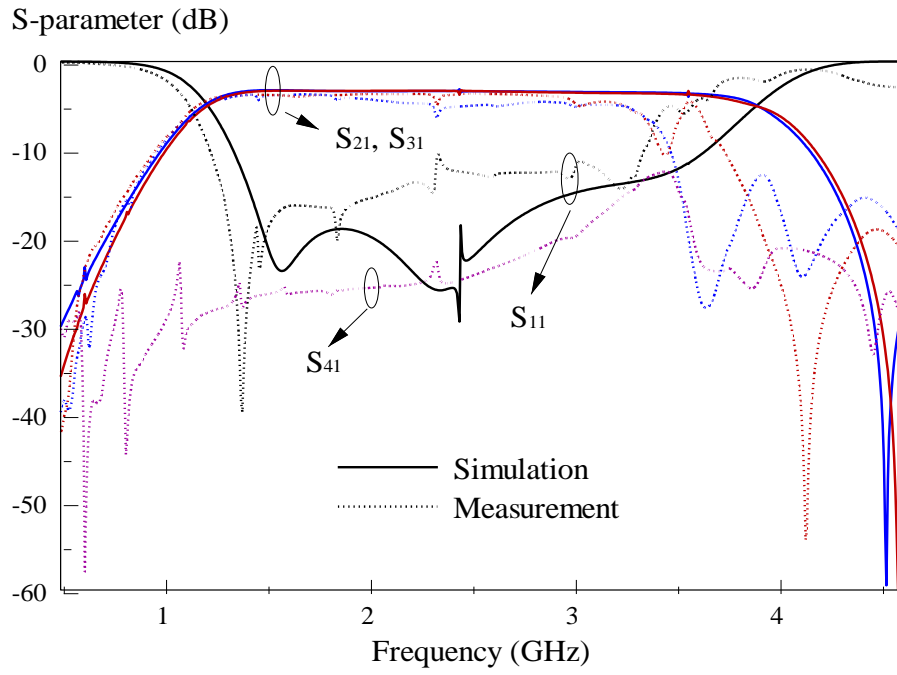
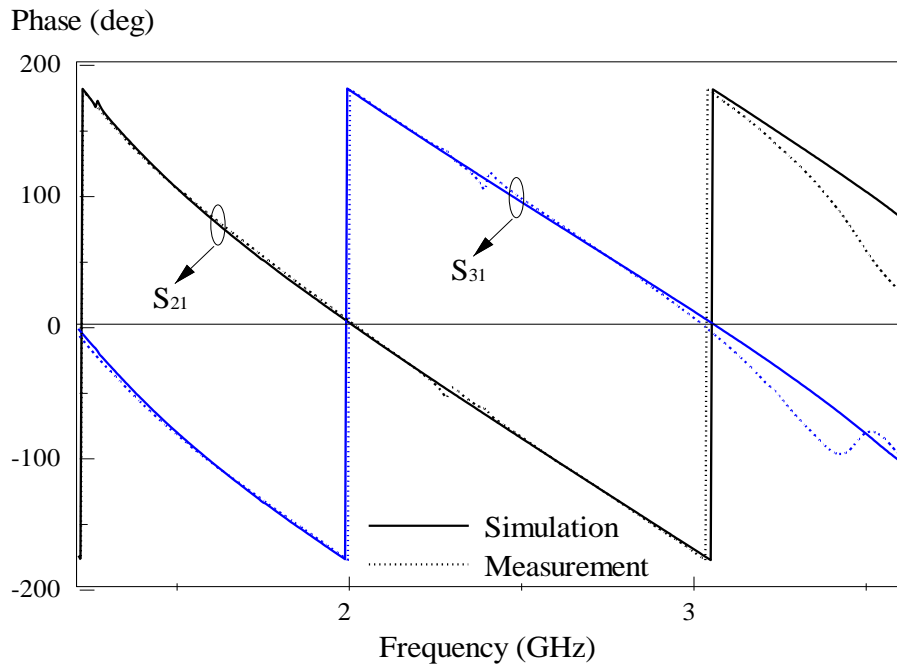


Figure 3.34: Calculated amplitude imbalance and phase difference of the reconfigurable in-phase power divider.

Next, in order to configure the power divider to give out-of-phase signals, the diodes at Ports 2 - 3 are powered ON while the diode at Port 4 is OFF. The amplitude and phase responses of this reconfigurable out-of-phase power divider are shown in *Figure 3.35*. The experimental and simulated results agree reasonably well. It has a simulated passband covering 1.34 - 3.65 GHz with a fractional bandwidth of 92.59%. Measured passband encompasses 1.23 - 3.28 GHz, being slightly narrower, giving a fractional bandwidth of 90.82%. The isolation level (S_{41}) of Port 4 can reach -16 -dB when disconnected, shown in *Figure 3.35(a)*. From *Figure 3.36*, the power divider has an amplitude imbalance of less than 1.5-dB while the output phase ($|\angle S_{21} - \angle S_{31}|$) is 180° out-of-phase within the range of 6° across the passband.



(a)



(b)

Figure 3.35: Measured and simulated (a) amplitude response, (b) phase response of the reconfigurable out-of-phase power divider.

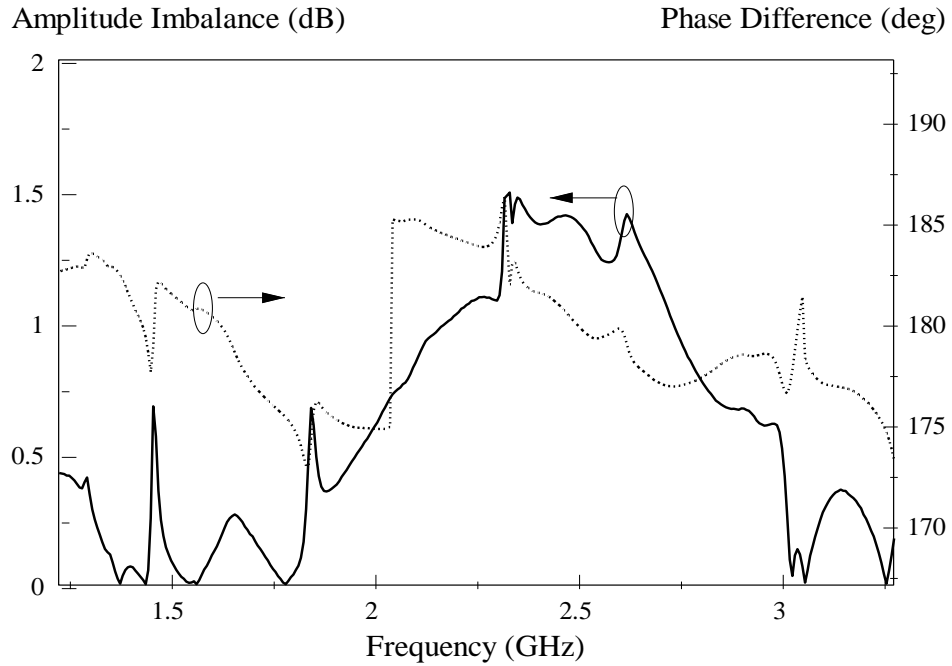


Figure 3.36: Calculated amplitude imbalance and phase difference of the reconfigurable out-of-phase power divider.

3.6 Conclusion

In conclusion, the in-phase and out-of-phase as well as the reconfigurable bandpassing power dividers have been successfully demonstrated in this chapter. Here, in-phase and out-of-phase reconfiguration can be easily achieved in a single piece of resonator by incorporating several RF switches into the feedlines. It is cost saving and versatile to have two distinct microwave modules implemented in one. Design equations have been worked out for the traveling wave mechanism. Good agreement has been observed between the simulated and experimental results. Parametric analysis has also been performed to study the effects of all the design parameters.

CHAPTER 4

Multilayered Bandpassing Couplers

4.1 Introduction

Circular patch resonator, also called circular disk, was first proposed by J. Watkins (1969). Because of its simplicity, it has been used for designing many types of microwave components. Since then, many disk-based resonators such as sector, annular sector and annular ring have been explored for antennas (L. C. Shen, et al., 1977; S. M. Ali, et al., 1982; W. F. Richards, et al., 1984; Z. Nie, et al., 1990; W. H. Hsu and K. L. Wong, 1998). The circular disk can also be used as a non-radiating microwave component. Gupta et al. (K. C. Gupta, and M. D. Abouzahra, 1985; M. D. Abouzahra and K. C. Gupta, 1987) proposed several multi-port couplers that are designed from the circular microstrip patch. Most of the reported patch couplers have poor frequency selectivity.

In 2006, F. Ferrero, et al. proposed a reconfigurable hybrid coupler which could be used to feed any printed radiating elements for achieving full polarization agility. By changing the state of its quasi-lumped hybrid coupler, the integrated antenna was able to radiate linearly or circularly polarized (LHCP or RHCP) electromagnetic waves. Later, A. Ocera, et. al. (2007) came up with a directional coupler that can be easily reconfigured by simply independent sets of MEMS switches so that the RF signals can be directed to the desired directions. L. Marcaccioli, et al. (2008) designed a broadband reconfigurable coupler at the Ku-

band. It was able to provide two different coupling levels (-10 dB and -17 dB) by making use of several RF-MEMS switches. The coupler has good impedance matching and port isolation.

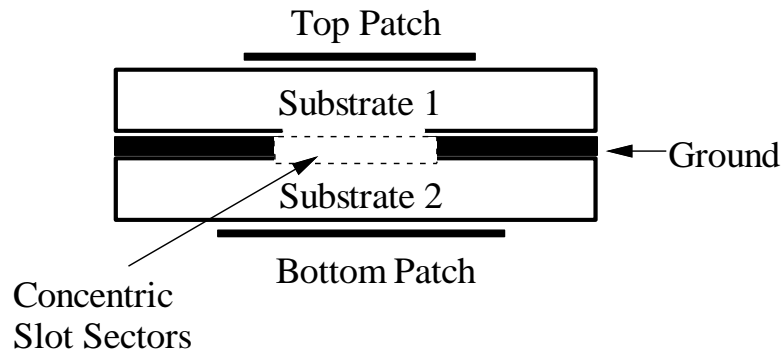
To improve the frequency selectivity, the multilayered slot-based bandpassing couplers, which are designed by combining two circular microstrip patches with four annular sectorial slots, are explored in this chapter to provide bandpassing effect and multiple outputs. The standing-wave resonances are deployed. To verify the design ideas, Ansoft HFSS was used to simulate all the configurations, and experiments were done by using the R&S@ZVB8 Vector Network Analyzer (VNA). Parametric analysis has been performed to study the effects of all the design parameters. The substrate RT/Duroid 4003C, with dielectric constant of $\epsilon_r = 3.38$ and thickness of $h = 0.8128$ mm, was used throughout the entire project.

4.2 Multilayered Bandpassing Power Divider

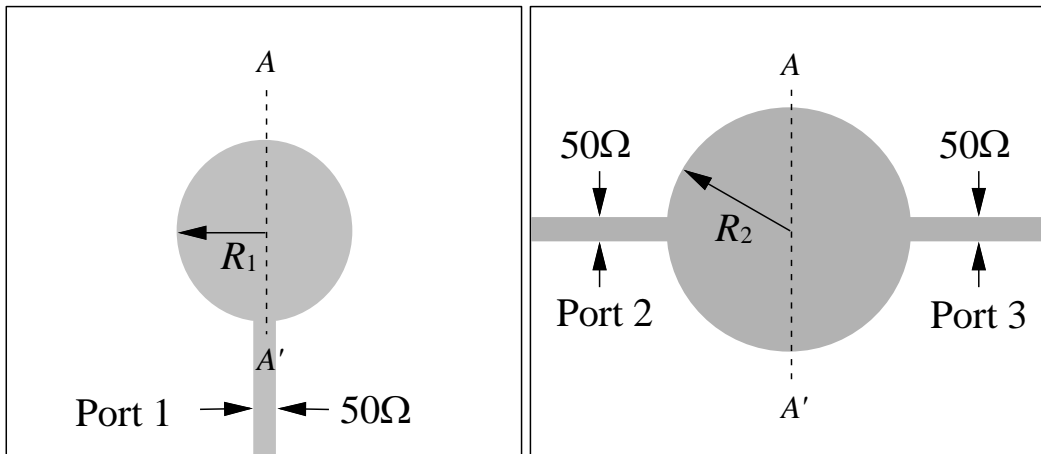
4.2.1 Configuration

The configuration of the bandpassing power divider will be illustrated in this section. *Figure 4.1* shows the schematic of the proposed bandpass power divider. The power divider has three ports, consisting of circular patches on the top and bottom with different radii. Besides that, the ground plane that accommodates the

annular slot sectors is sandwiched in between Substrate 1 and 2. Microwave signal is launched at Port 1 to feed the top patch. Then, it is coupled to the bottom patch going through the slot sectors and equally split into two equal output signals. All the ports are fed by 50Ω microstrip feedlines made on a substrate with a dielectric constant of $\epsilon_r = 3.38$ and a thickness of $h = 0.8128\text{mm}$. The component is symmetric along $A - A'$, with the detailed design parameters given by $R_1 = 12\text{ mm}$, $R_2 = 16\text{ mm}$, $R_3 = 1\text{ mm}$, $R_4 = 17\text{ mm}$, $\theta_1 = 27.31^\circ$, $\theta_2 = 14.41^\circ$, $\theta_3 = 6.82^\circ$, and $\theta_4 = 5.50^\circ$. The photographs of the prototype of the proposed bandpassing power divider are presented in *Figure 4.2*.

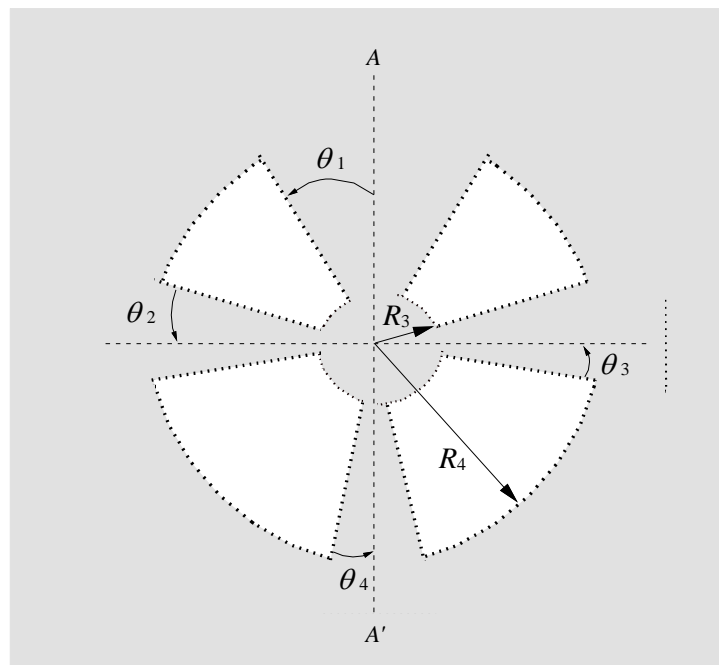


(a)



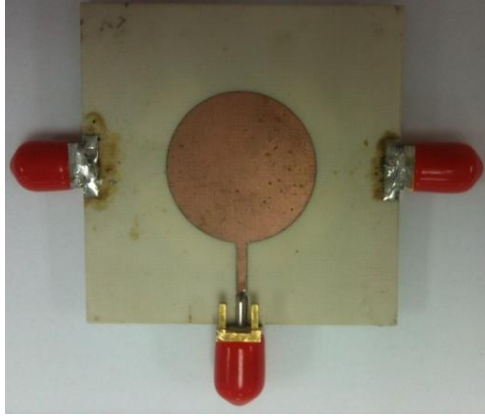
(b)

(c)

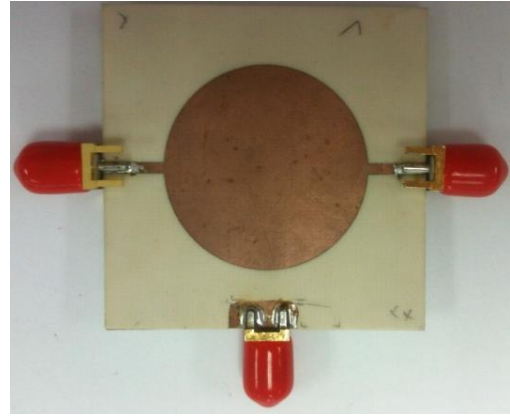


(d)

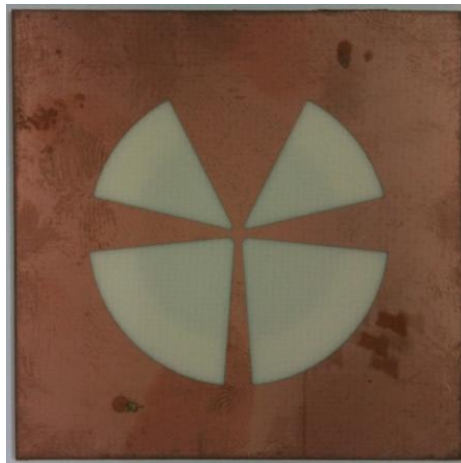
Figure 4.1: Schematic of the proposed bandpassing power divider: (a) Front view.(b) Top patch. (c) Bottom patch. (d) Concentric slot sectors in the middle layer.



(a)



(b)



(c)

Figure 4.2: Photographs of the prototype of the proposed bandpassing power divider:(a)Top patch. (b) Bottom patch. (c) Concentric slot sectors in the middle layer.

4.2.2 Simulation and Experimental Results

The amplitude and phase responses are shown in *Figure 4.3*. The experimental result agrees well with the simulation. It can be seen that two resonance modes are introduced to form the passband, and two transmission zeros are introduced for sharpening the roll-off skirts for a wider bandwidth and higher selectivity. Besides that, the input power is equally divided into the two output ports with amplitude imbalance of less than 0.5-dB across the passband. The simulated result has a passband from 2.27 GHz to 2.89 GHz with a fractional bandwidth of 24.03%. Meanwhile, the measured result gives a narrower passband covering 2.43 GHz - 2.99 GHz, yielding a fractional bandwidth of 20.66%. The phase response is shown in *Figure 4.3(b)*, showing a difference ($|\angle S_{21} - \angle S_{31}|$) of less than 4° in the passband. In *Figure 4.4*, the simulated and measured isolation curves between the two output ports show reasonable agreement. The group delays for the input signal to reach the two output ports are shown in *Figure 4.5*. Both are showing less than 1ns inside the passband, implying minimum signal distortion.

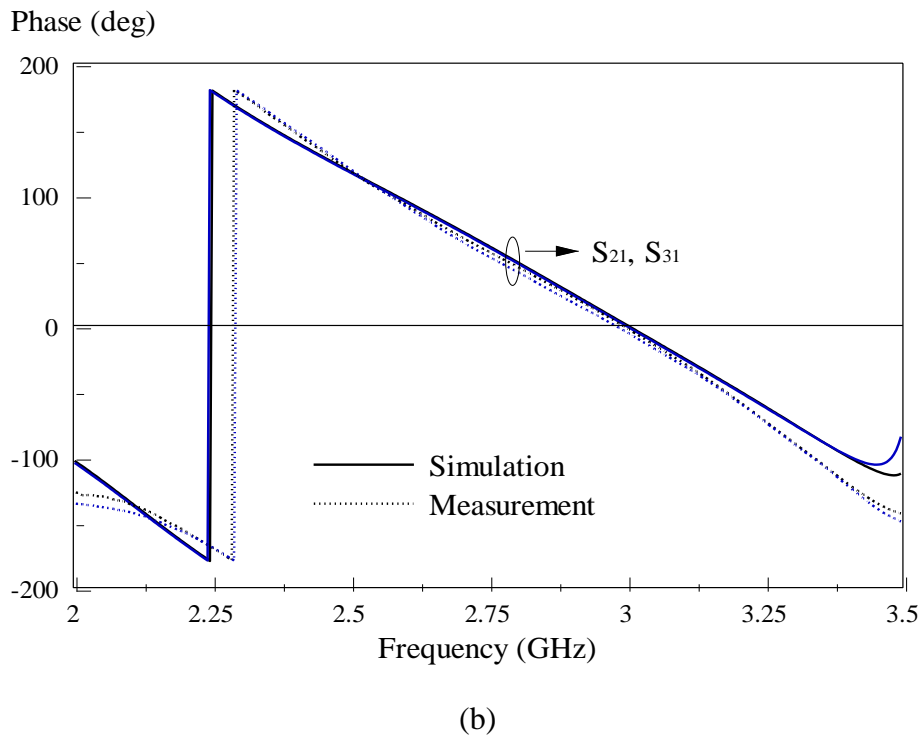
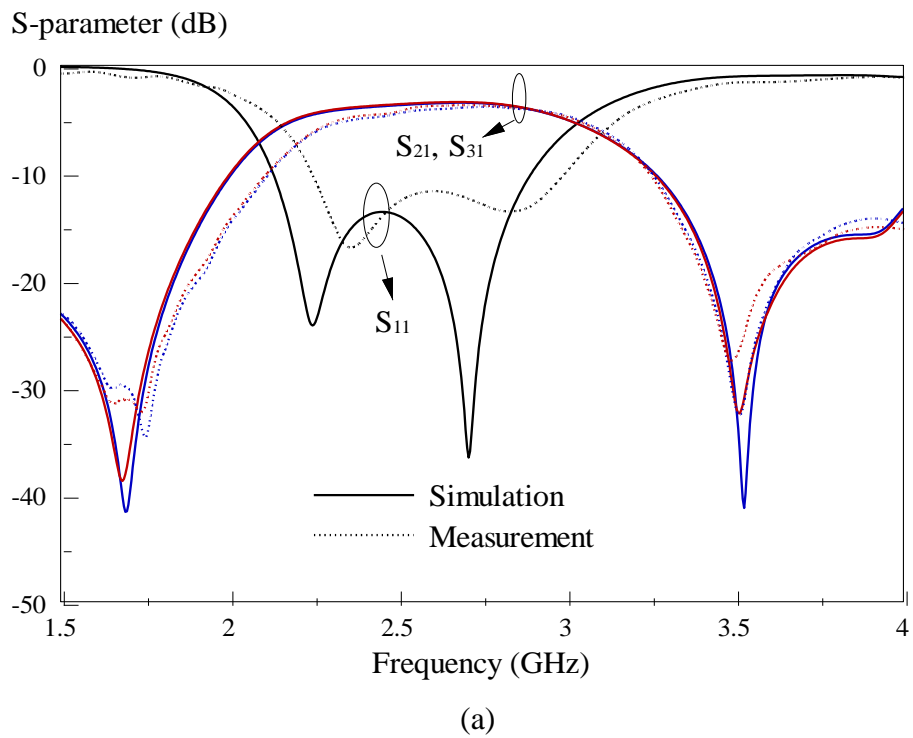


Figure 4.3: Measured and simulated (a) amplitude response, (b) phase response of the bandpassing power divider.

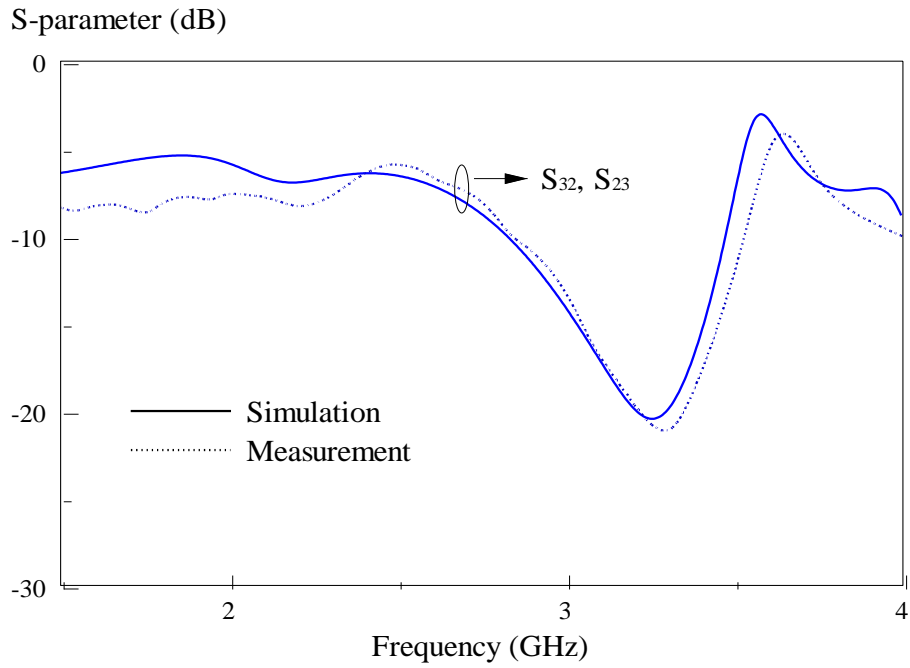


Figure 4.4: Measured and simulated isolation curves between the output ports of the bandpassing power divider.

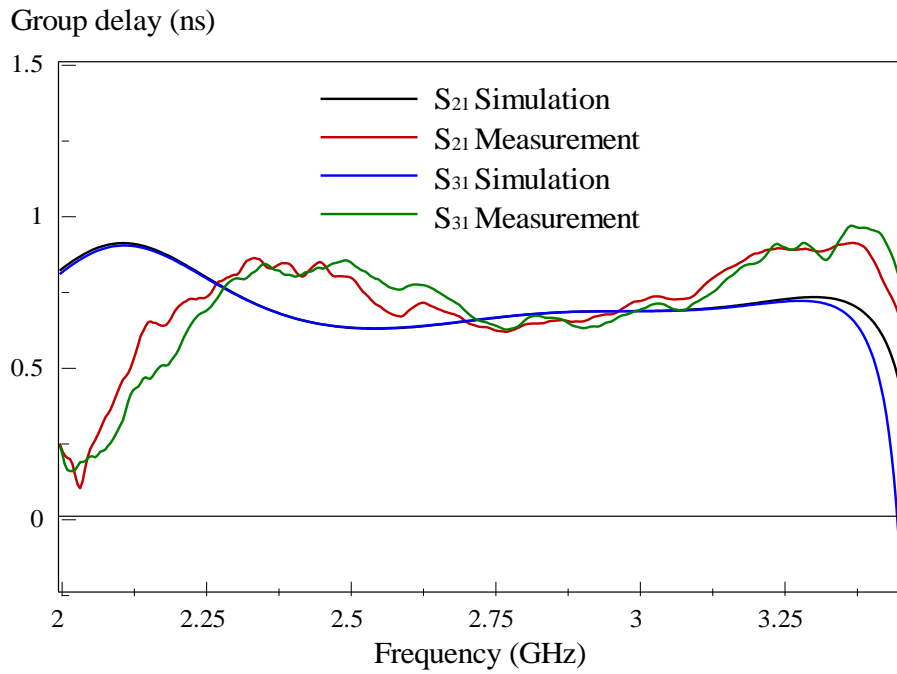
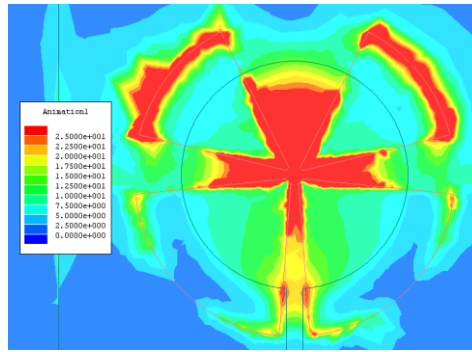


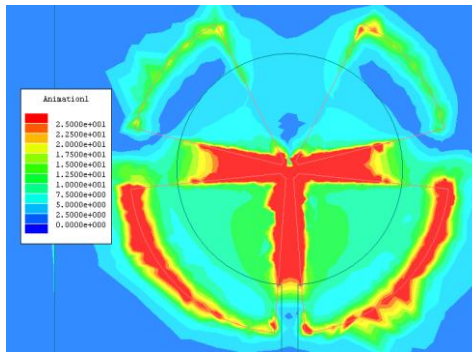
Figure 4.5: Measured and simulated group delays.

4.2.3 Electric and Magnetic Field Characteristics

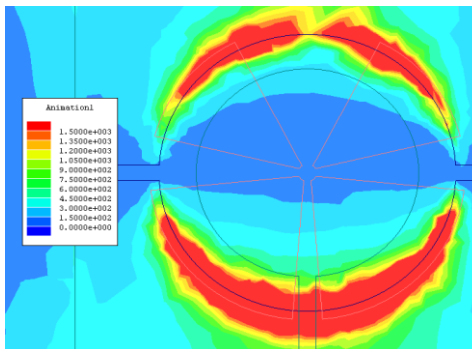
The electric and magnetic field distributions of the proposed bandpassing power divider are illustrated in this section. As can be seen from the amplitude response shown in *Figure 4.3(a)*, the simulated curve consists of two resonating poles at 2.25 GHz (P_1) and 2.71 GHz (P_2). The corresponding magnetic field distributions are shown in *Figure 4.6(a) - (b)*. With reference to *Figure 4.6(a)*, the P_1 is introduced by the two top annular sectorial slots and the bottom patch (R_2). The P_2 is caused by the lower two annular sectorial slots and the top patch (R_1). Besides that, there are two zeros observed near to the lower ($Z_1 = 1.69$ GHz) and upper ($Z_2 = 3.52$ GHz) cutoff frequencies. *Figure 4.6(c)* shows the electric field distribution at Z_1 . As can be seen from the figure, the zero Z_1 is caused by the bottom patch with a radius of R_2 , θ_1 , and θ_4 . The magnetic field distribution of Z_2 is shown in *Figure 4.6(d)*. It is obvious that this zero is introduced by the top patch (R_1). The field penetrates through the four annular sectorial slots.



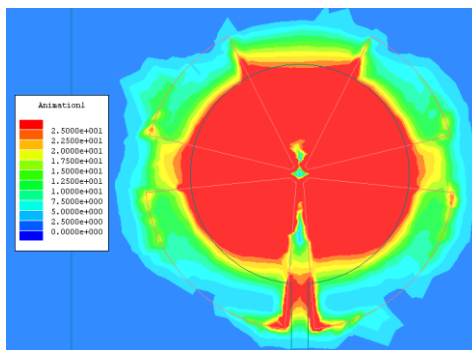
(a)



(b)



(c)



(d)

Figure 4.6: The field distributions of the proposed bandpassing power divider at (a) 2.25 GHz, (b) 2.71 GHz, (c) 1.69 GHz,(d) 3.52 GHz.

4.2.4 Parametric Analysis

The design parameters for the bandpass power divider are analyzed individually in order to understand the configuration better. The effect of the circular patch and annular sectorial slot resonator will be studied in this section. It has been found that all pole and zero resonating modes can be kept for most cases. Also, the performances of the power divider can be easily analyzed by observing parametric analysis.

4.2.4.1 Patch Radius, R_1 and R_2

Two poles are still observed in *Figure 4.7*. The P_2 is found shifting from 2.82 GHz to 2.55 GHz with increasing R_1 from 10 mm to 14 mm. But the roll-off rate near to the upper cutoff frequency (Z_2) becomes much sharper in this case. The optimal value of 12 mm has been selected as it is able to give good roll-off and broad bandwidth at the same time. It can be explained by the fact that wave is travelling along the perimeter of the patch. A larger patch will result in a longer traveling path which causes the operating frequency to reduce.

The effect of the bottom patch (R_2) is now studied. Notably, this parameter only affects Z_1 and P_1 frequencies, without affecting others. It is seen from *Figure 4.8*

that the P_1 frequency leaps from 2.24 GHz to 2.47 GHz when the radius R_2 is decreased from 16 mm to 14.5 mm.

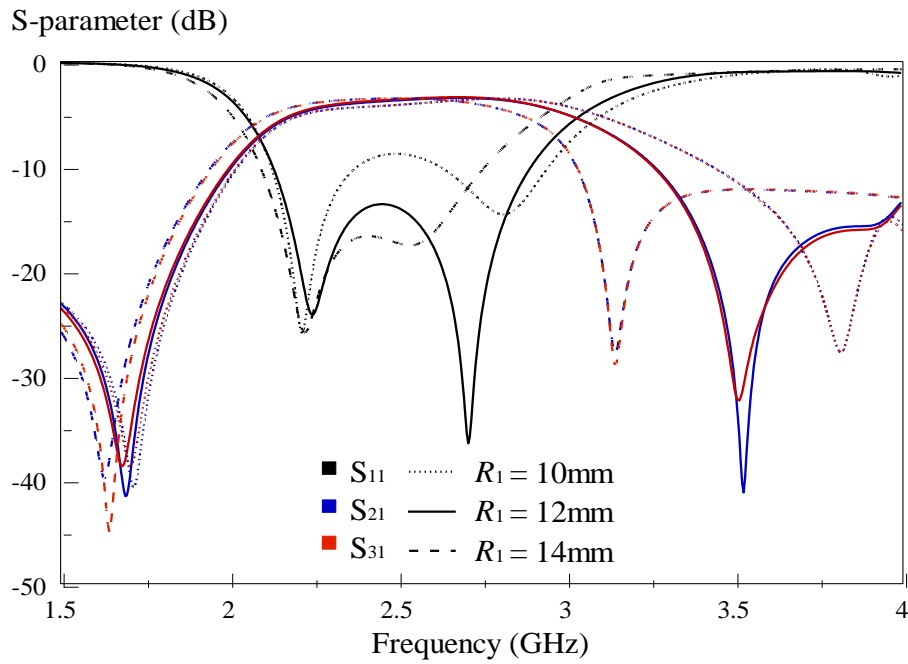


Figure 4.7: Amplitude response of the bandpassing power divider when R_1 is varied.

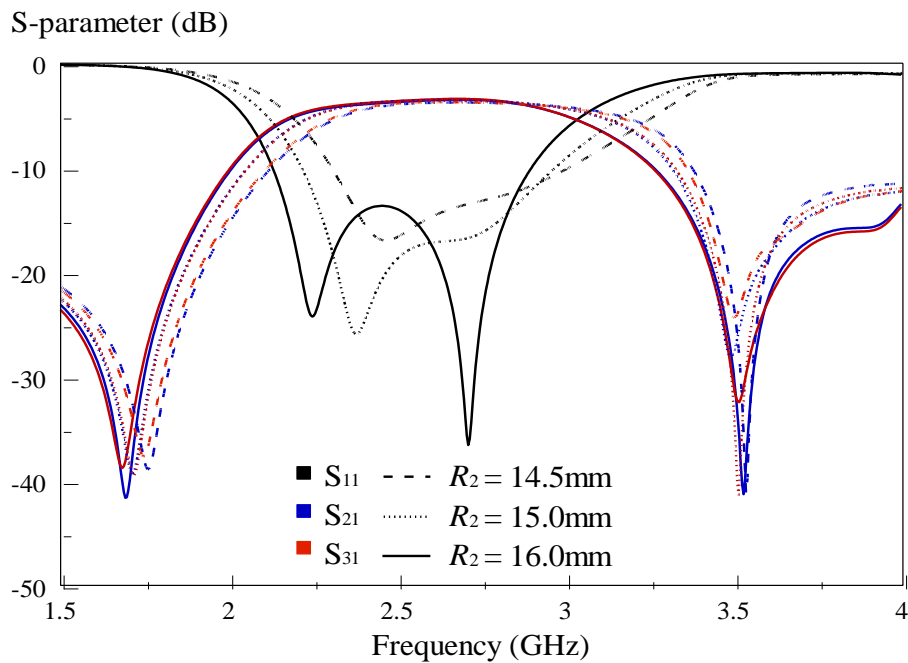


Figure 4.8: Amplitude response of the bandpassing power divider when R_2 is varied.

4.2.4.2 Radius, R_3 and R_4

As can be seen in *Figure 4.9*, increasing R_3 causes the frequency of the lower zero (Z_1) to increase, but that for the P_2 to reduce. It is also obvious that the selected R_3 can give the best result for both. As can be seen in *Figure 4.10*, the radius of the annular slots affects P_2 . Larger radius R_4 causes the resonant frequency P_2 to increase.

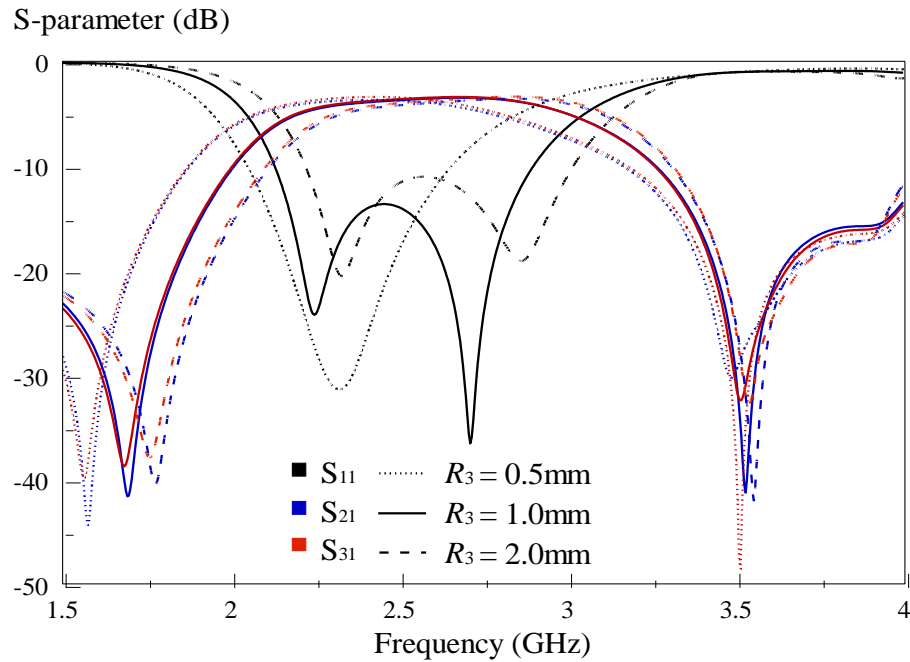


Figure 4.9: Amplitude response of the bandpassing power divider when R_3 is varied.

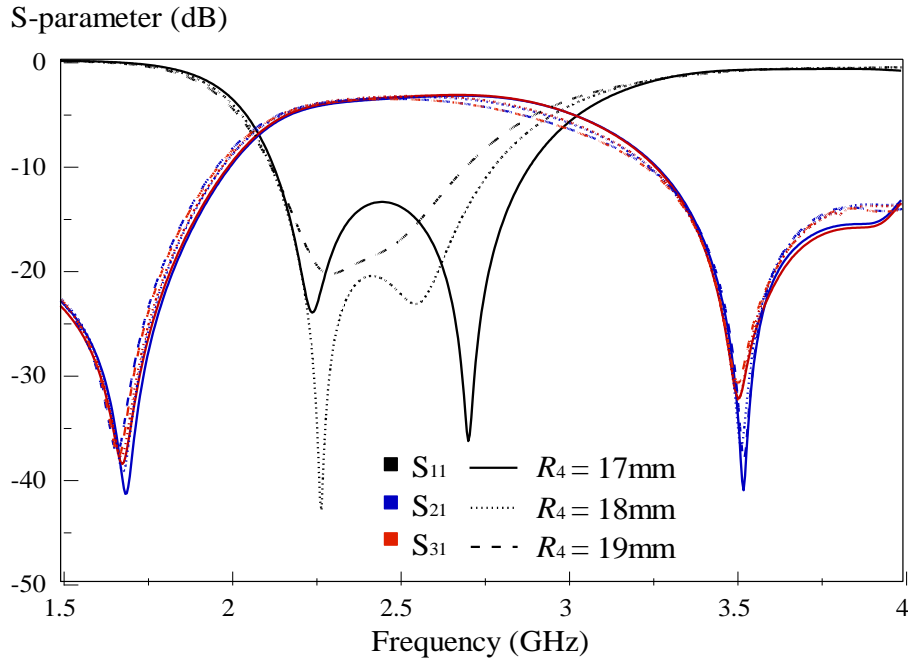


Figure 4.10: Amplitude response of the bandpassing power divider when R_4 is varied.

4.2.4.3 Sector Angles, θ_1 , θ_2 , θ_3 , and θ_4

In *Figure 4.11*, increasing θ_1 from 19.66° to 36.03° causes the Z_1 frequency to reduce from 1.78GHz to 1.58 GHz, without affecting others. However, it causes the impedance matching of P_1 and P_2 to become slightly poorer. As a result, θ_1 is designed to be 27.31° to obtain both good frequency selectivity and impedance bandwidth. With reference to *Figure 4.12*, larger θ_2 results in lower P_2 frequency but higher Z_1 frequency. The impedance matching is optimum at $\theta_2= 14.41^\circ$. It can be seen from *Figure 4.13* that θ_3 does not affect poles and zeros. *Figure 4.14* shows the amplitude response of the in-phase power divider by varying the angle of θ_4 . From the figure, it is observed that $\theta_4= 5.5^\circ$ gives the best impedance matching and fractional bandwidth.

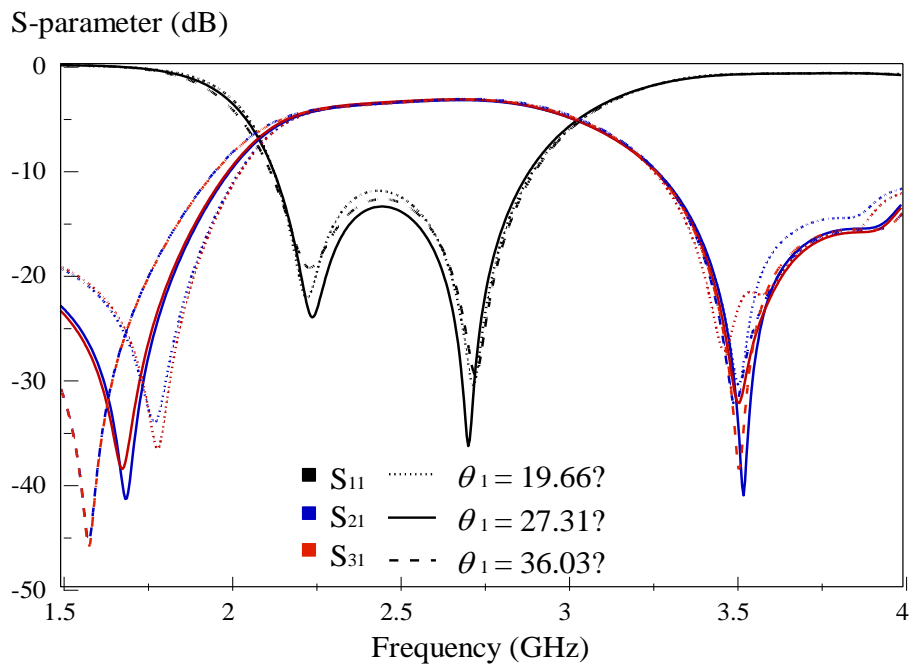


Figure 4.11: Amplitude response of the bandpassing power divider when θ_1 is varied.

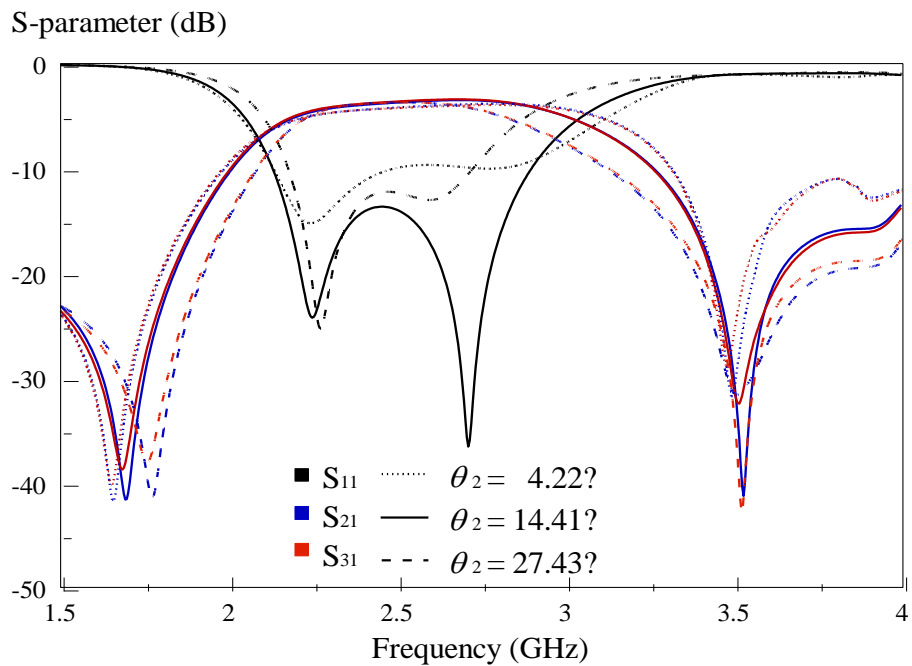


Figure 4.12: Amplitude response of the bandpassing power divider when θ_2 is varied.

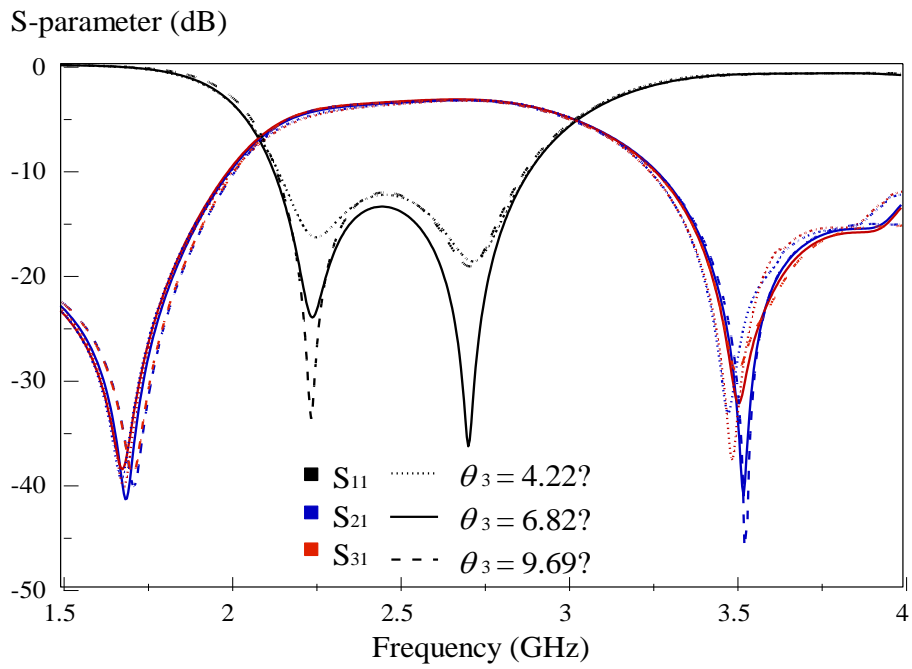


Figure 4.13: Amplitude response of the bandpassing power divider when θ_3 is varied.

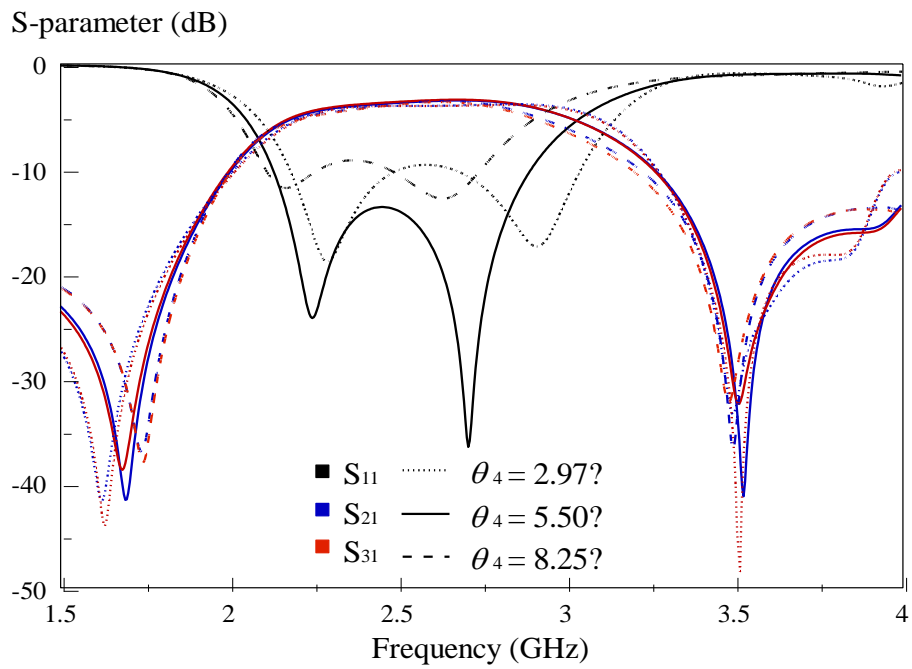


Figure 4.14: Amplitude response of the bandpassing power divider when θ_4 is varied.

4.3 Multifunctional Bandpass Power-Dividing Directional Coupler

4.3.1 Configuration

The configuration of the proposed multifunctional and bandpassing power-dividing directional coupler with multiple outputs will be discussed in this section. The configuration is shown in *Figure 4.15*. In this new implemented structure, two additional ports (Ports 4 and 5) have been introduced for constructing the 20-dB directional coupler. Also, this configuration is symmetric along $A - A'$. Here, Port 1 is the input port, Ports 2 and 3 are the coupled ports to give half-power division while Ports 4 and 5 are giving 20-dB coupling output signals. The sectorial slots decide how much signal is going to the output ports. The detailed design parameters for the proposed configuration are given by $R_1 = 12$ mm, $R_2 = 16$ mm, $R_3 = 1$ mm, $R_4 = 17$ mm, $\theta_1 = 27.31^\circ$, $\theta_2 = 14.41^\circ$, $\theta_3 = 6.82^\circ$, $\theta_4 = 5.50^\circ$, and $\theta_5 = 40^\circ$. The photographs of the fabricated prototype are shown in *Figure 4.16*.

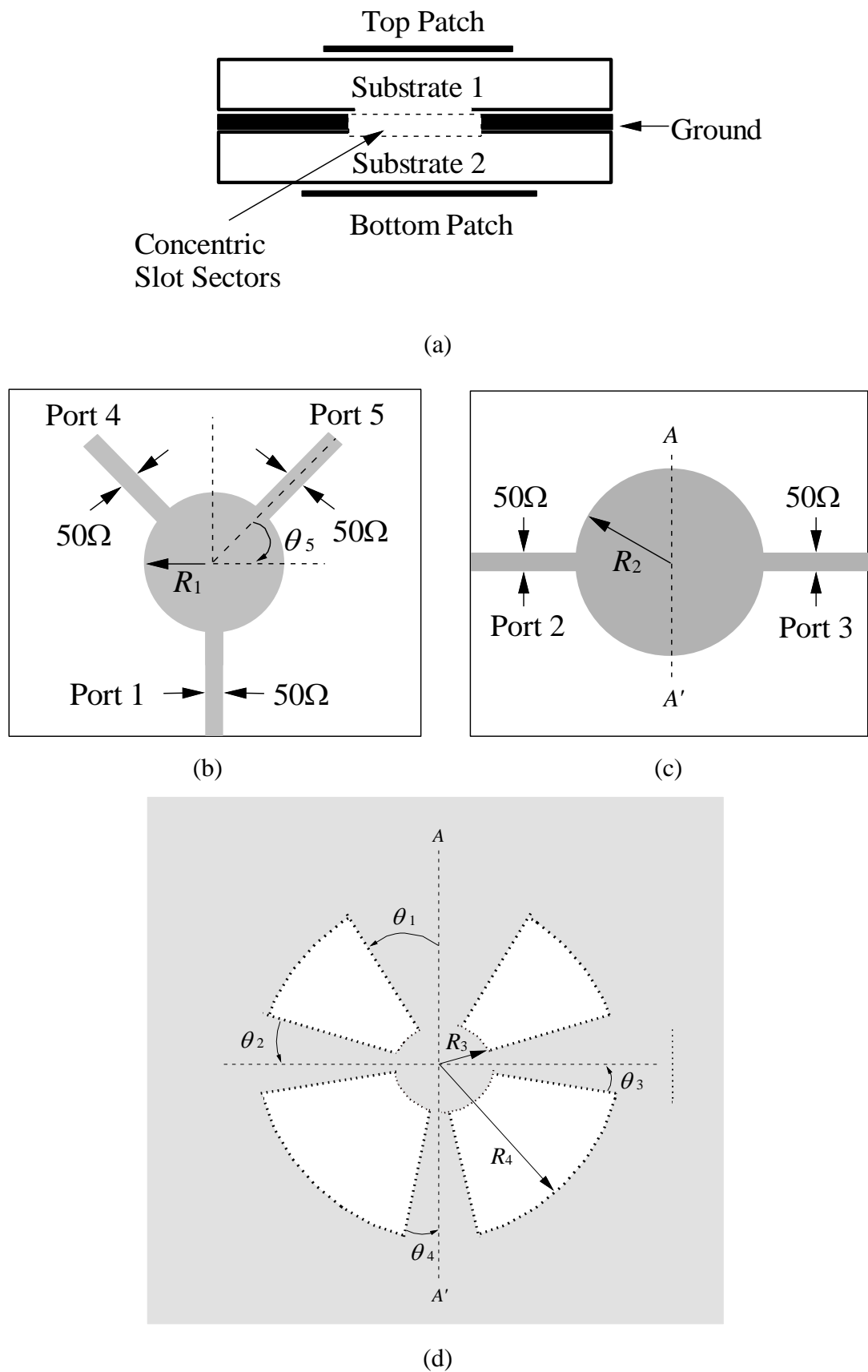


Figure 4.15: Schematic of the proposed bandpass power dividing directional coupler: (a) Front view. (b) Top patch. (c) Bottom patch. (d) Concentric slot sectors in the middle layer.

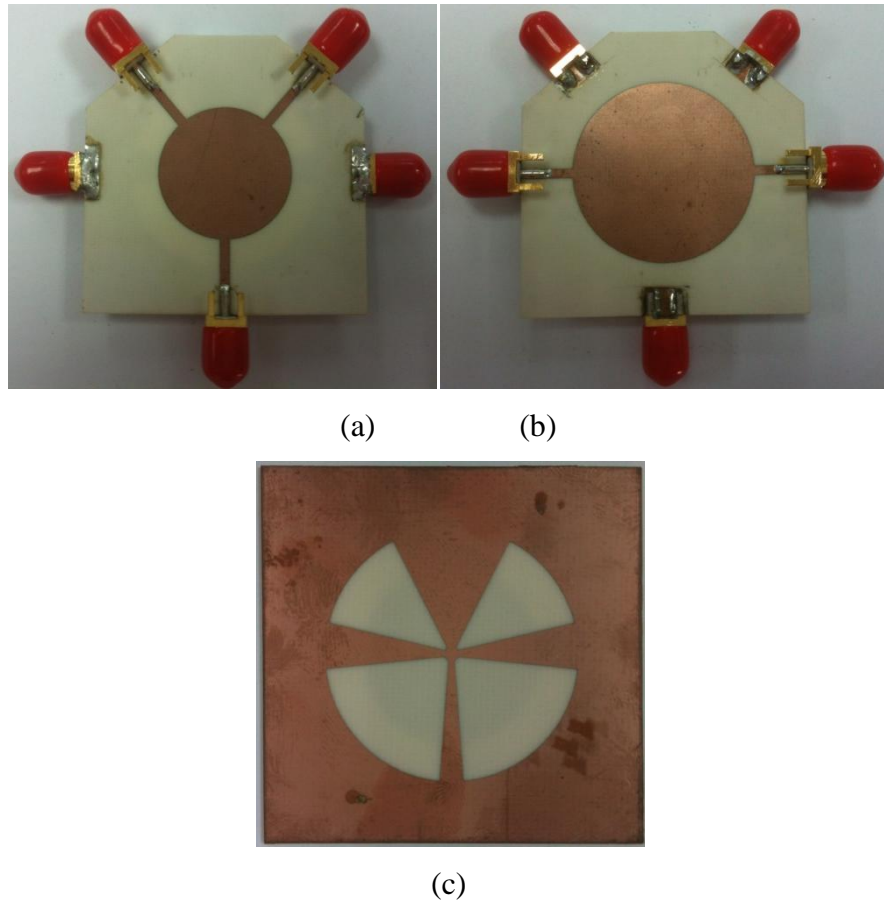


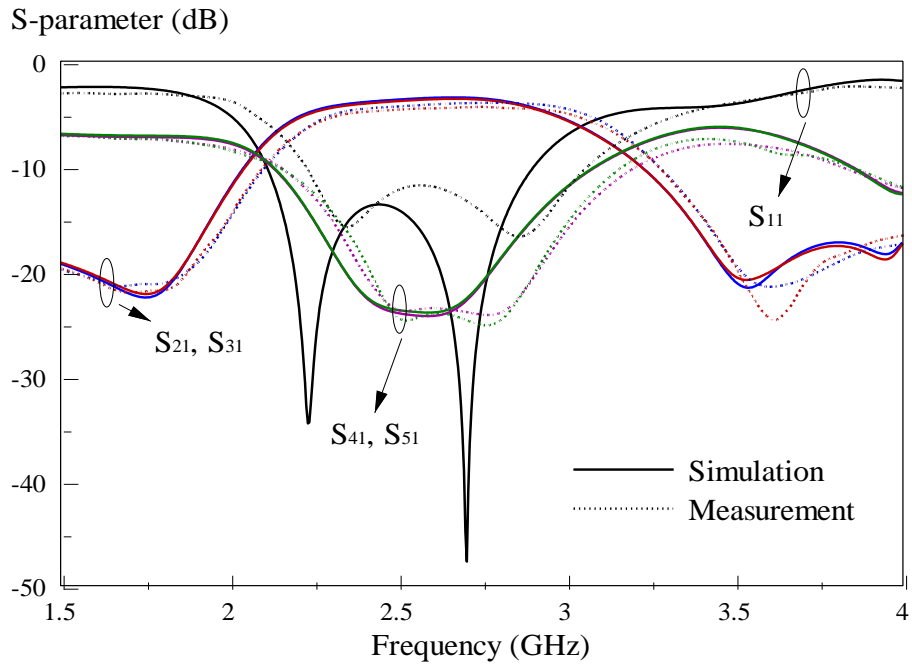
Figure 4.16: Photographs of the prototype of the proposed bandpass power dividing directional coupler: (a) Top patch. (b) Bottom patch. (c) Concentric slot sectors in the middle layer.

4.3.2 Simulation and Experiment Results

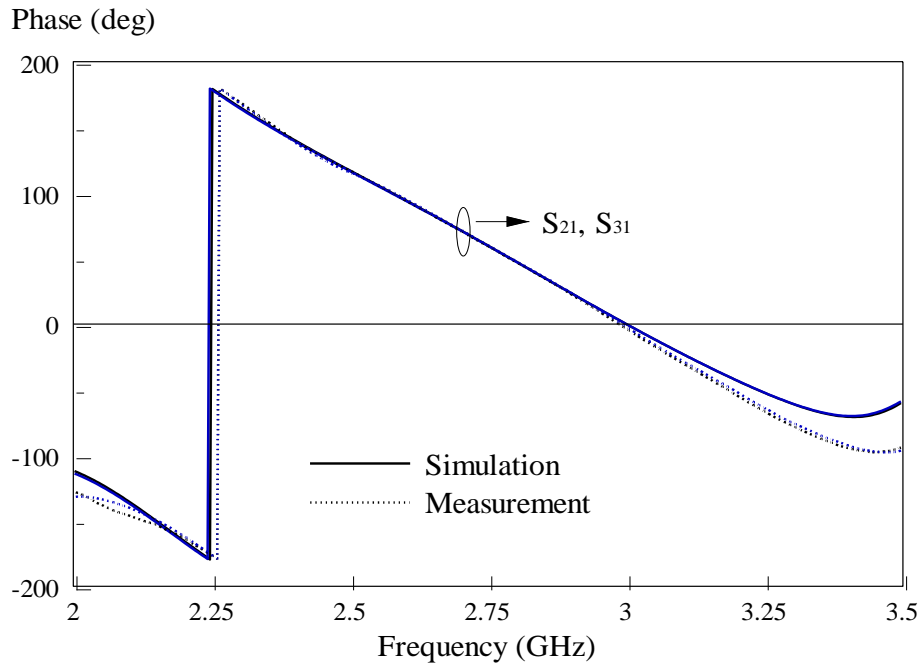
The experimental amplitude and phase responses agree well with the simulation shown in *Figure 4.17* and *Figure 4.18*. It has two poles at 2.23 GHz (P_1) and 2.71 GHz (P_2), and two zeros at 1.78 GHz (Z_1) and 3.53 GHz (Z_2). Broader bandwidth and higher selectivity can be achieved at the same time by introducing two resonating poles and two transmission zeros. With reference to *Figure 4.17(a)*, it can be seen that the in-phase half-power division at Ports 2 and 3 has a measured fractional bandwidth of 26.87% (simulation 23.94%), covering 2.32 GHz - 3.04 GHz

(simulation 2.28 GHz - 2.90 GHz) with the observation of an amplitude imbalance of less than 0.5-dB. Working as a directional coupler, the multifunctional component has a measured -23 -dB fractional bandwidth of 13.85%, covering 2.44 GHz to 2.80 GHz. More interestingly is that the coupled signals both Ports 4 and 5 are 20 ± 1 dB lower than those at Ports 2 and 3 over a measured frequency range of 2.49 GHz - 2.80 GHz (simulation 2.42 GHz to 2.71 GHz). The phase responses of the half-power divider (Ports 2 and 3) and 20-dB coupler (Ports 4 and 5) are shown in *Figure 4.17(b)* and *Figure 4.18*. It can be seen that the phases between Ports 2 and 3 are almost equal, with a discrepancy ($|\angle S_{21} - \angle S_{31}|$) of less than 5° over the entire passband. The same tolerance is observed for Ports 4 and 5 ($|\angle S_{41} - \angle S_{51}|$). The simulated and measured isolation curves between the four output ports agree reasonably well, as shown in *Figure 4.19*. The group delays for the input signal to reach the four output ports are shown in *Figure 4.20* and *Figure 4.21*. All are below 1ns with a constant delay in the passband. It has negative group delay at the coupling outputs because the phase slope is positive (A. R. Dordevic and D. V. Tosic, 2010).

Since there is no isolation port for this case, the directivity and isolation (David M. Pozar, 2005) for the power-dividing directional coupler are infinity. A good directional coupler is always required to have high directivity of at least 35-dB. The measured coupling factor and insertion loss are -23.56 -dB and -4.10 -dB, respectively, at the center frequency.



(a)



(b)

Figure 4.17: Measured and simulated (a) amplitude response, (b) phase response of the half-power outputs of the bandpass power dividing directional coupler.

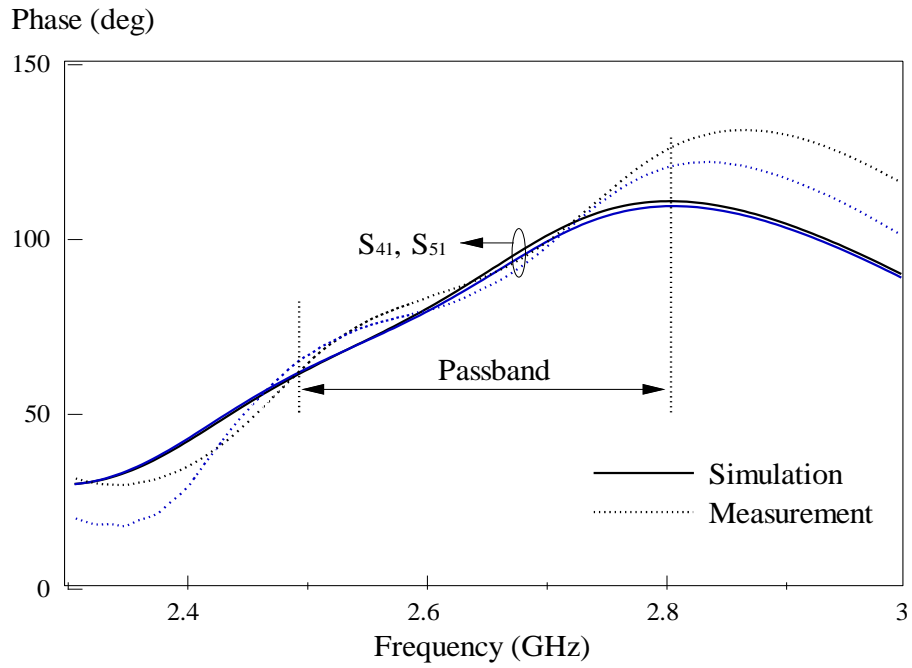


Figure 4.18: Measured and simulated phase response of the 20-dB output signals of the bandpass power dividing directional coupler.

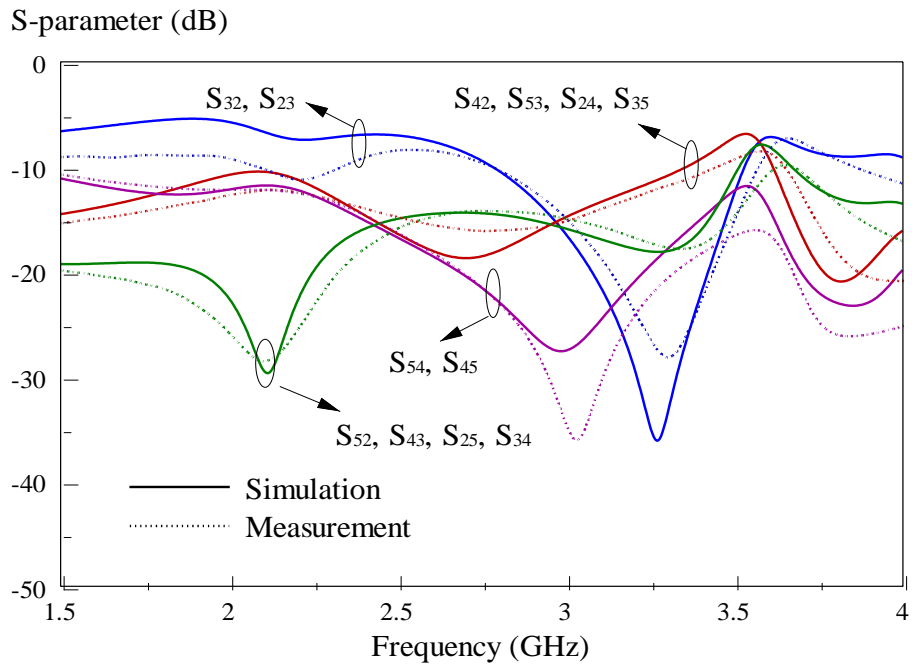


Figure 4.19: Measured and simulated isolation between the output ports of the bandpass power dividing directional coupler.

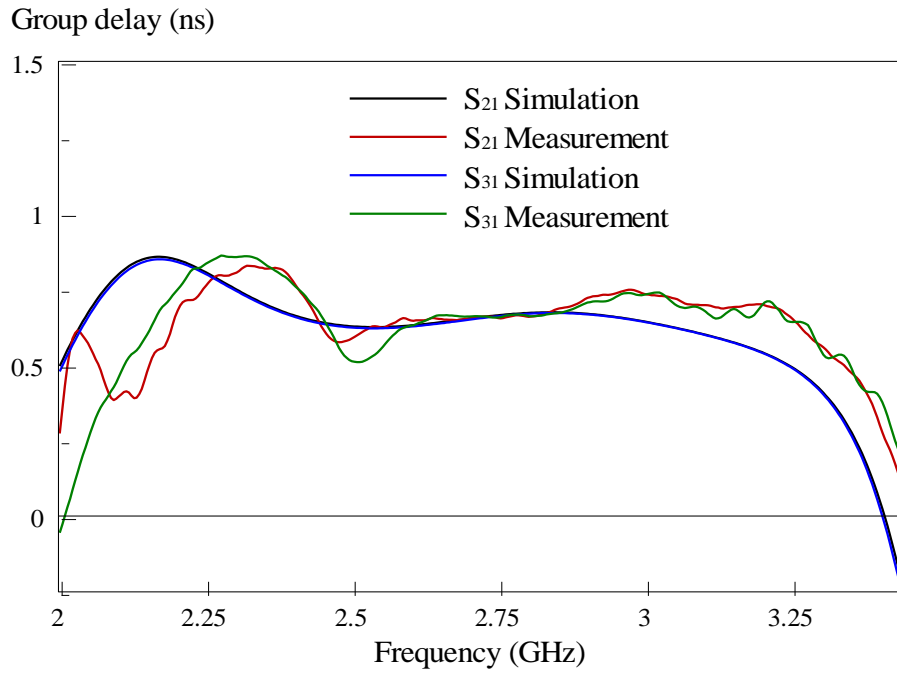


Figure 4.20: Measured and simulated group delays for the input signal to reach the half-power division ports (Ports 2 and 3).

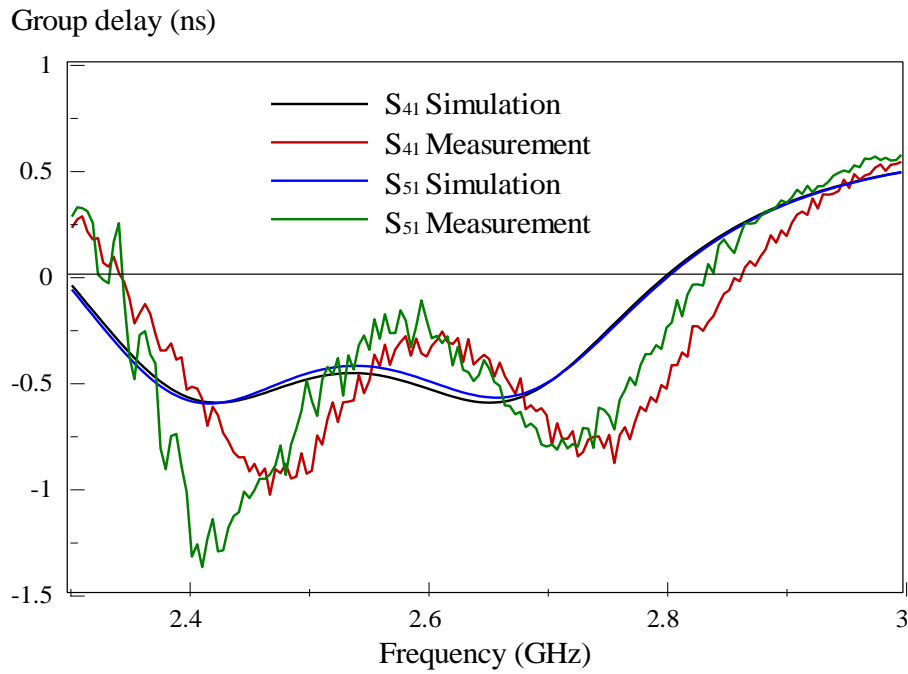


Figure 4.21: Measured and simulated group delays for the input signal to reach the 20-dB coupling ports (Ports 4 and 5).

4.3.3 Electric and Magnetic Field Characteristics

The electric and magnetic field distributions of all the poles and zeros are discussed here. It can be seen from *Figure 4.22(a) - (d)* that the responses are quite similar to those in *Figure 4.6*. This is reasonable as they have the same resonator.

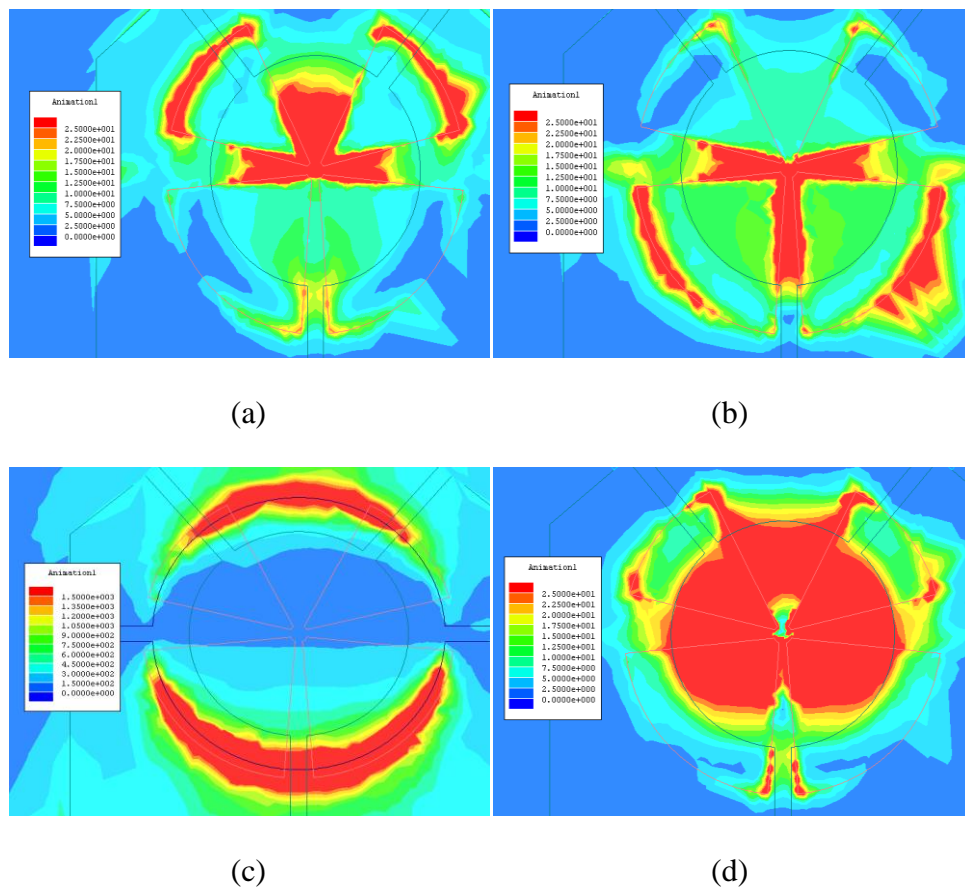


Figure 4.22: The field distributions of the proposed bandpassing power divider at (a) 2.23 GHz, (b) 2.71 GHz, (c) 1.78 GHz, (d) 3.53 GHz.

4.3.4 Parametric Analysis

Parametric analysis has been performed on the bandpass power-dividing directional coupler. The effect of the circular patch and the annular sectorial slot resonators will be studied in this section. It is usually very challenging to optimize a 20-dB directional coupler with multiple modes as any change in the design parameters will affect the performance of the component.

4.3.4.1 Patch Radius, R_1 and R_2

First, the effect of R_1 is studied for the bandpass power dividing directional coupler. Observed in *Figure 4.23* is that frequency of P_2 increases from 2.53 GHz to 2.82 GHz when the top circular patch is decreased from 14mm to 10mm. At the same time, the zero near to the upper cutoff frequency (Z_2) shifts from 3.19 GHz to 4.04 GHz as R_1 goes lower. It has the best roll-off skirt when R_1 is set to be 14mm but the bandwidth becomes slightly narrower. However, the 20-dB coupling signals at Ports 4 and 5 are jeopardized in this case.

Figure 4.24 shows the effect on the amplitude response by varying the bottom circular patch R_2 . This parameter only affects Z_1 and P_1 frequencies. The P_1 frequency is found shifting from 2.23 GHz to 2.51 GHz with decreasing R_2 from 16mm to 14.5mm. Meanwhile, other pole and zeros remain unchanged. Still, the performance of the coupling signals at Port 4 and 5 degrades when R_2 is varied. Besides that, the

passband moves higher for a smaller patch. The 20-dB coupling signals at Ports 4 and 5 are affected when R_2 is varied.

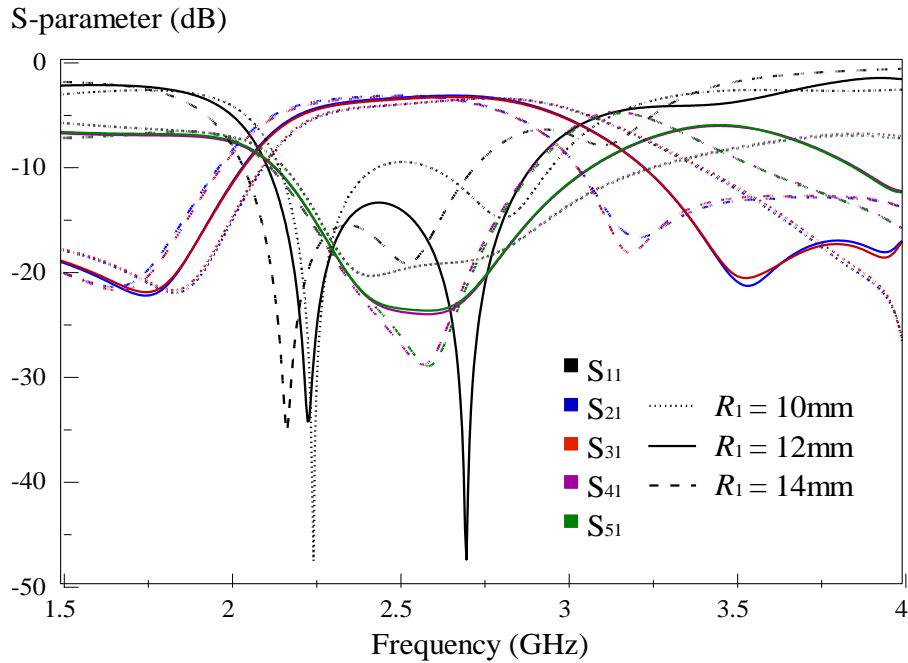


Figure 4.23: Amplitude response of the bandpass power-dividing directional coupler when R_1 is varied.

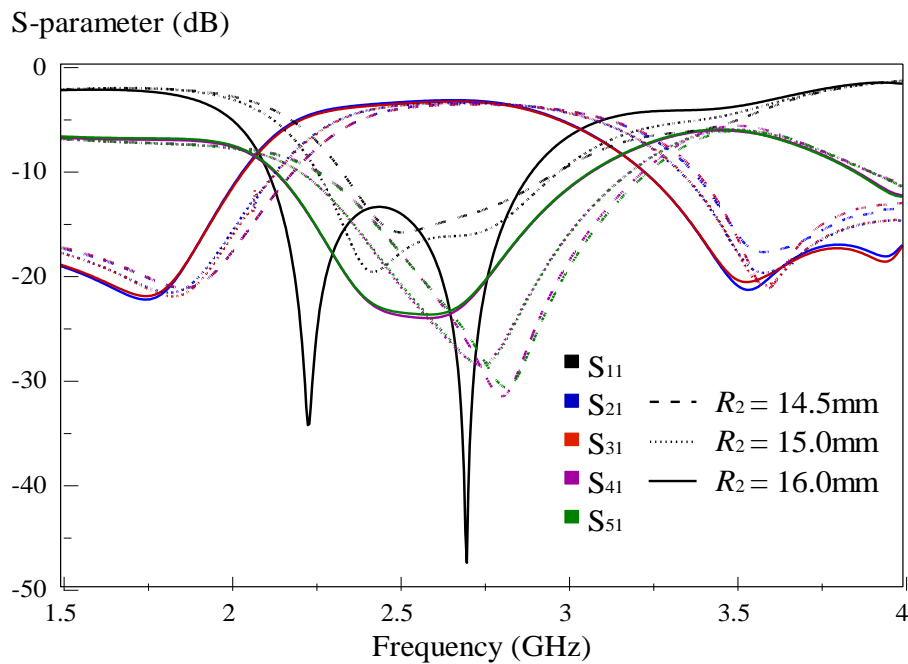


Figure 4.24: Amplitude response of the bandpass power-dividing directional coupler when R_2 is varied.

4.3.4.2 Radius, R_3 and R_4

With reference to *Figure 4.25*, it can be seen that increasing R_3 causes the frequency of the Z_1 to increase (2.19 GHz to 2.31 GHz), but that for the P_2 to reduce (1.87 GHz to 1.77 GHz). Also observed is that the selected R_3 can give the best result when it is set to be 1 mm to give broad bandwidth with good impedance matching at all the outputs. As can be seen in *Figure 4.26*, P_2 is affected when R_4 is varied. The resonant frequency P_2 decreases when R_4 is made larger. Both radii of R_3 and R_4 will affect the 20-dB coupling signals at Ports 4 and 5.

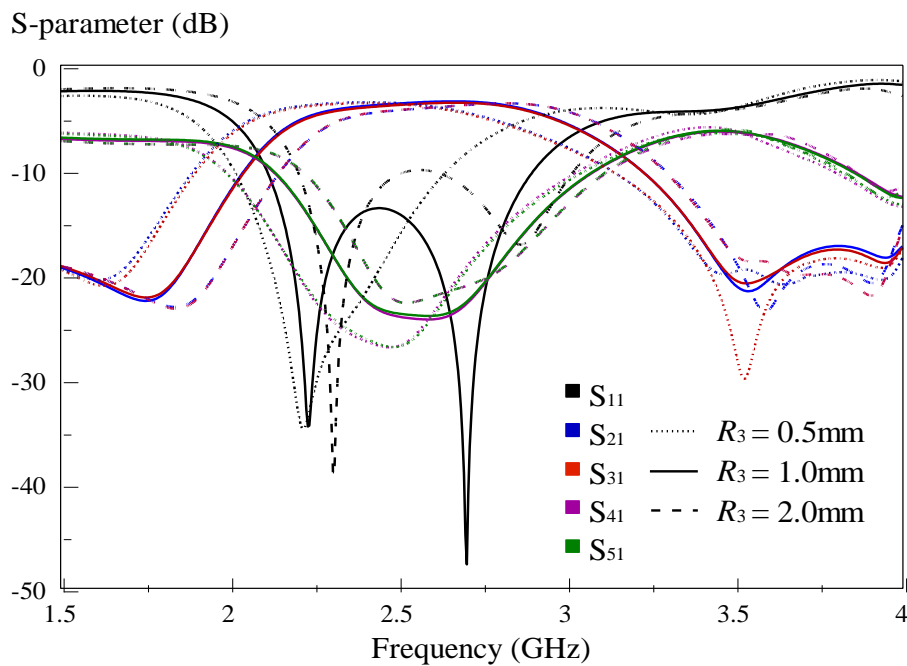


Figure 4.25: Amplitude response of the bandpass power-dividing directional coupler when R_3 is varied.

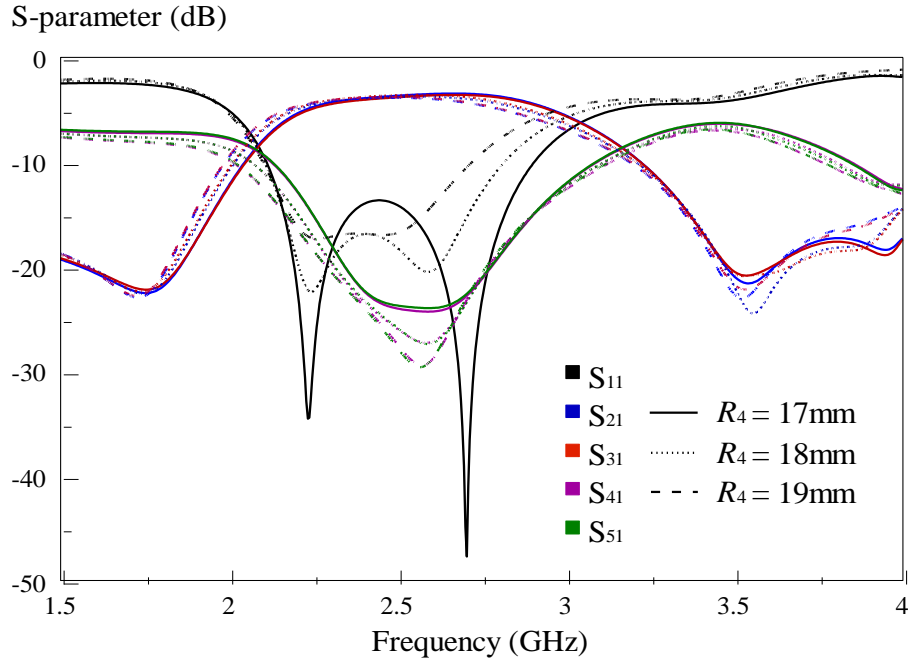


Figure 4.26: Amplitude response of the bandpass power dividing directional coupler when R_4 is varied.

4.3.4.3 Sector Angles, θ_1 , θ_2 , θ_3 , and θ_4

In *Figure 4.27*, the Z_1 frequency increases from 1.63 GHz to 1.91 GHz when θ_1 is changed from 19.66° to 36.03° . In this case, the impedance matching of the two resonating poles becomes slightly poorer. But to have good roll-off-skirt and impedance bandwidth, θ_1 is optimized to be 27.31° . Also seen in *Figure 4.28* is that the P_2 frequency is optimized at $\theta_2 = 14.41^\circ$. Again, θ_3 does not affect all the poles and zeros, as shown in *Figure 4.29*. It can be seen from *Figure 4.30* θ_4 is optimum at 5.5° to have better impedance matching and bandwidth simultaneously. It was found that the 20-dB coupling signals at Port 4 and Port 5 are very sensitive to all the angles.

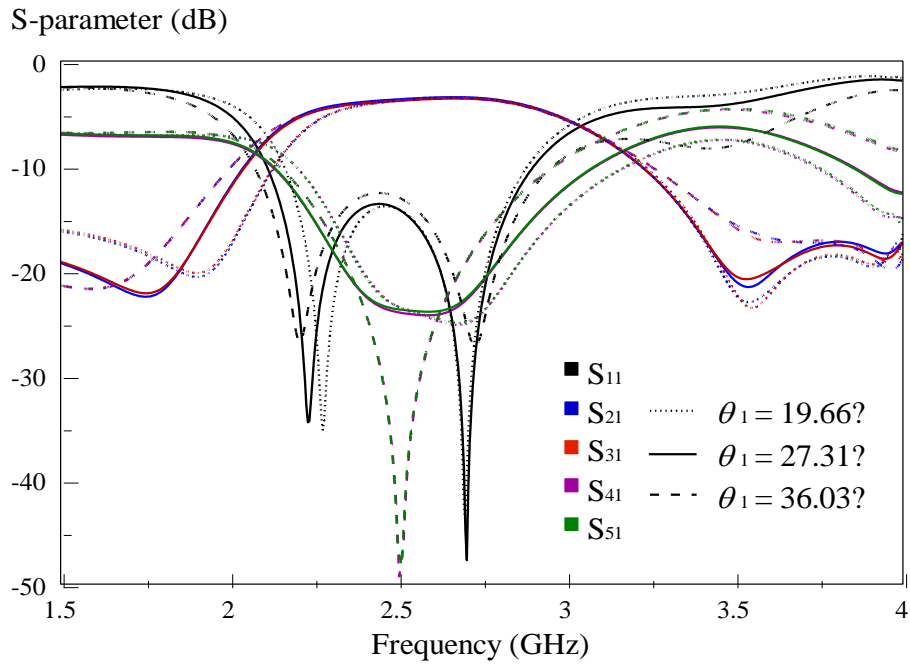


Figure 4.27: Amplitude response of the bandpass power-dividing directional coupler when θ_1 is varied.

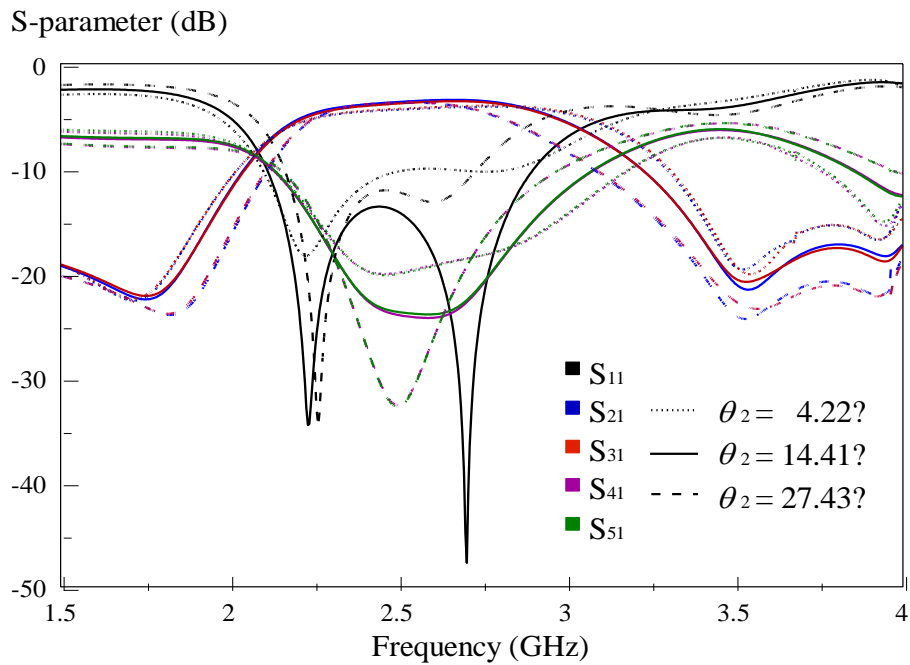


Figure 4.28: Amplitude response of the bandpass power-dividing directional coupler when θ_2 is varied.

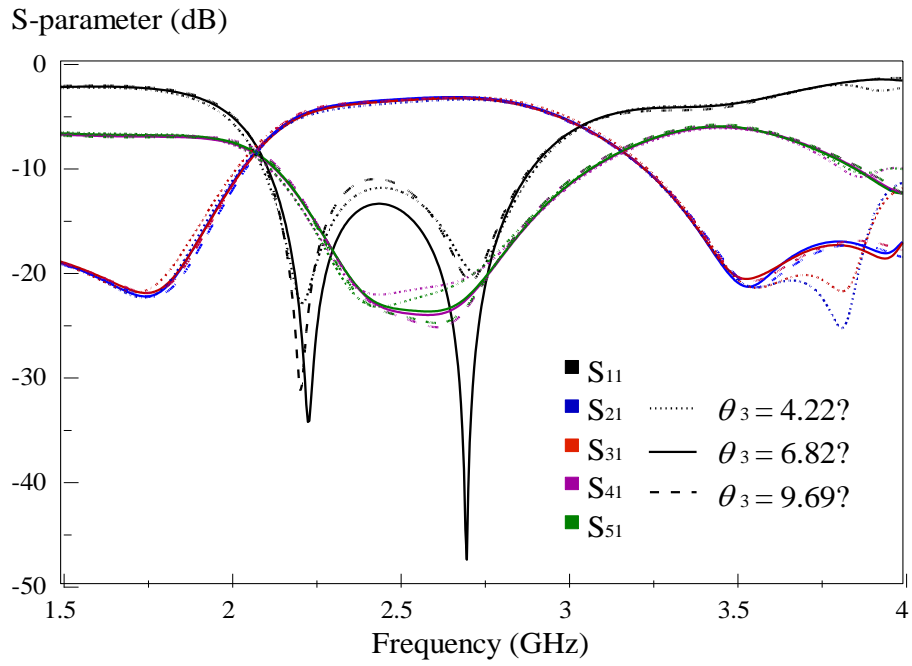


Figure 4.29: Amplitude response of the bandpass power-dividing directional coupler when θ_3 is varied.

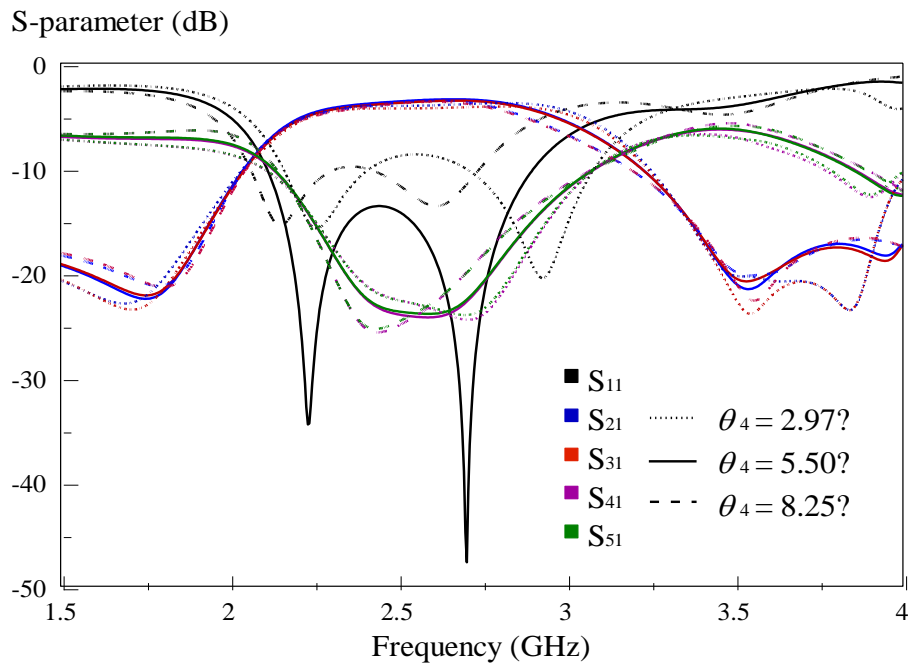


Figure 4.30: Amplitude response of the bandpass power-dividing directional coupler when θ_4 is varied.

4.3.4.4 Inclination Angle θ_5 of Feedlines

The inclination angle, θ_5 affects the coupled signals at Ports 4 and 5. As can be seen from *Figure 4.31*, the coupled powers reduce with decreasing angle. The bandwidth of the coupled signals is optimized at the inclination angle θ_5 of 40° .

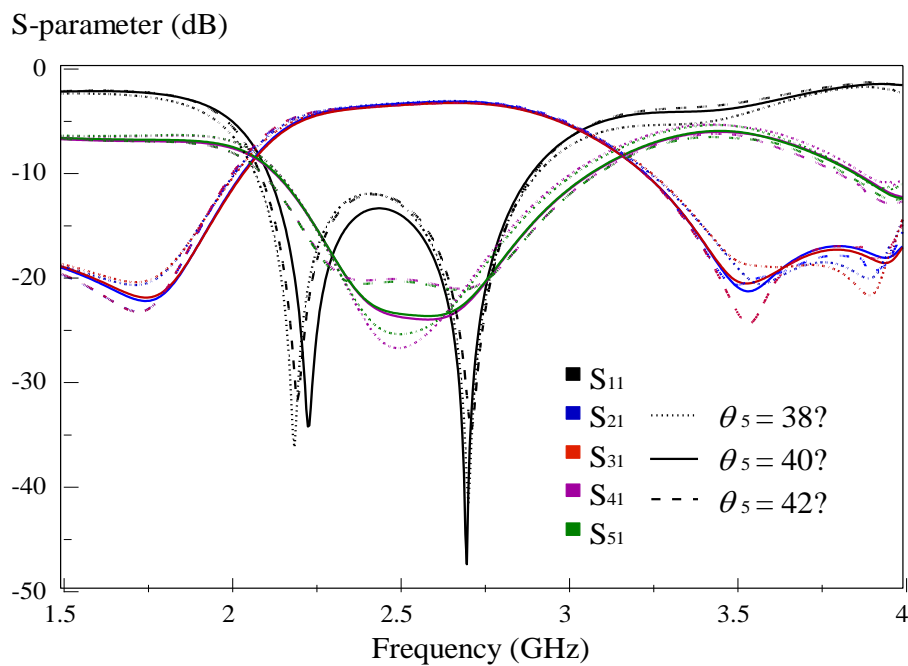


Figure 4.31: Amplitude response of the bandpass power-dividing directional coupler when θ_5 is varied.

4.4 Conclusion

In conclusion, the bandpass power divider and bandpass power-dividing directional coupler have been successfully designed in this chapter. The circular patch power divider can be made to provide coupling functions by adding in extra output ports. Multifunctional components are much desired because of their low cost and high compactness. The simulated and experimental results agree well. All the design parameters have been studied and analyzed.

CHAPTER 5

Conclusion

5.1 Summary

In this dissertation, two different power dividers have been proposed. In the first part, the bandpassing in-phase and out-of-phase power dividers have been designed by using the rectangular slot array. To achieve multifunction, several PIN diodes are incorporated with the feedlines for phase reconfiguration. In the second part, a bandpassing power dividers and a bandpassing power-dividing coupler are designed from a hybrid resonator consisting of two circular disks and four annular sectorial slots. The multifunctional power divider can also produce 20-dB coupled signals. Reasonable agreement has been observed between all the simulations and measurements.

5.2 Future Works

This dissertation has successfully proposed two novel microwave structures for the multifunctional slot-based bandpassing power dividers and couplers. It is obvious that multifunction is a possible avenue for achieving high compactness in the wireless systems. To obtain an even broader bandwidth, in the future, it is believed that hybrid resonator may be used. This is because the performance of the microstrip-

based resonators are somewhat limited by the Q factor. Also, the employment of leaky-wave modes may be a possible way for getting an ultra-wide bandwidth.

References

A. G. Bert and D. Kaminsky, 1980 The Traveling Wave Power Divider/Combiner, *10th European Microwave Conference*, pp.408-412.

A. K Bhattacharyya, 1990 Long Rectangular Patch Antenna with a Single Feed, *IEEE Trans. Antennas Propag.*, 38(7), pp.987-993.

A. M. Abbosh, 2009 Ultra Wideband Inphase Power Divider for Multilayer Technology, *IET Microw. Antennas Propag.*, 3(1), pp.148-153.

A. Ocera, P. Farinelli, P. Mezzanotte, R. Sorrentino, B. Margesin, F. Giacomozzi, 2007 Novel RF-MEMS Widely-Reconfigurable Directional Coupler, *Proceedings of European Microwave Conference*, pp.111-125.

A. R. Dordevic and D. V. Tasic, 2010 Negative Group Delay and Causality, *5th European Conference on Circuits and Systems for Communications (ECCSC'10)*.

Ansoft Corporation, High Frequency Structure Simulator (HFSS) v. 11 [Online]. Available: <http://www.ansoft.com/products/hf/hfss/>. [11 July 2010]

C. A. Balanis, 1997 Antenna Theory, John Wiley & Sons, Inc., Second Edition.

C.-K. Wu and C.-K. C. Tzuang, 2002 Dual-Band Microstrip Leaky-Mode Antenna of Similar Radiation Characteristics, *IEEE Antennas and Propagation Society International Symposium*, 3, pp.387-390.

C. W. Cheung and Y. O. Yam, 1994 Traveling-wave Power Combiner/Divider Implemented by Lumped Elements, *Electron. Lett.*, 30(9), pp.713-715.

D. M. Pozar, 1998 Microwave Engineering, John Wiley & Sons, Inc., Second Edition.

- D. Packiaraj, A. Bhargavi, M. Ramesh and A. T. Kalghatgi, 2008 Compact Power Divider using Defected Ground Structure for Wireless Application, *Int. Conf. Sig. Proc. Comm. Network*, pp.25-29.
- D. Yau, N. Y. Shuley and L. O. McMillan, 1999 Characteristic of Microstrip Leaky Wave Antenna Using The Method of Moments, *IEE Proceedings Microwaves, Antennas and Propagation*, 146(5), pp.324-328.
- E. E. Okon and C. W. Turner, 2002 Design of Broadband Microstrip Series Array for MM-wave Applications, *Electron. Lett.*, 38(18), pp.1036-1037.
- E. J. Wilkinson, 1960 An N-Way Hybrid Power Divider, *IRE Trans. Microw. Theory Tech.*, 8(1), pp.116-118.
- F. S. Coale, 1956 A Traveling-Wave Directional Filter, *IRE Trans. Microw. Theory Tech.*, 4(4), pp.256-260.
- F. Ferrero, C. Luxey, G. Jacquemod, R. Staraj, and V. Fusco, 2006 A Reconfigurable Hybrid Coupler Circuit for Agile Polarisation Antenna, *Antennas and Propagation, EuCAP*, pp.1-5.
- G. Monti, R. D. Paolis, and L. Tarricone, 2009 Dual-Band T-Junction with a Reconfigurable Power Ratio, *Proceedings of European Microwave Conference*, pp.1219-1222.
- H. Jiang, K. M. Pasala, L. M. Kempel and S. M. Schneider, 2006 A Novel Broadband Microstrip Leaky Wave Antenna with Inhomogeneous Substrate, *IEEE Antennas and Propagation Society International Symposium*, pp.4243-4246.
- H. Q. Tserng and P. Saunier, 1985 10-30 GHz Monolithic GaAs Traveling-Wave Divider/Combiner, *Electron. Lett.*, 21(21), pp.950-951.

- J.-C. Chiu, J.-M. Lin and Y.-H. Wang, 2006 A Novel Planar Three-Way Power Divider, *IEEE Microw. Wireless Comp. Lett.*, 16(8), pp.449-451.
- J. E. Ruyle and J. T. Bernhard, 2011 A Wideband Transmission Line Model for a Slot Antenna, *IEEE Trans. Antennas Propag.*, 61(3), pp.1407-1410.
- J. N. Hines, V. H. Rumsey and C. H. Walter, 1953 Traveling-Wave Slot Antennas, *Proceedings of the IRE*, 41(11), pp.1624-1631.
- J.-S. Hong, 2011 Microstrip Filters for RF/Microwave Applications, John Wiley & Sons, Inc., Second Edition.
- J. Watkins, 1969 Circular Resonant Structures in Microstrip, *Electron. Lett.*, 5(21), pp.524-525.
- K. C. Gupta and M. D. Abouzahra, 1985 Analysis and Design of Four-Port and Five-Port Microstrip Disc Circuits, *IEEE Trans. Microw. Theory Tech.*, 33(12), pp.1422-1428.
- K. Chang and C. Sun, 1983 Millimeter-Wave Power-Combining Techniques, *IEEE Trans. Microw. Theory Tech.*, 31(2), pp.91-107.
- K. J. Russell, 1979 Microwave Power Combining Techniques, *IEEE Trans. Microw. Theory Tech.*, 27(5), pp.472-478.
- K. Kim, D. Jang, B. Dorjsuren, J. Lim, and D. Ahn, 2009 A New Design Method for a Dual-Band Power Divider, *Wireless and Microw. Tech. Conf.*, pp.1-4.
- K. M. Lum, C. Laohapensaeng and C. Free, 2005 A Novel Traveling-Wave Feed Technique for Circularly Polarized Planar Antennas, *IEEE Microw. Wireless Comp. Lett.*, 15(3), pp.180-182.

- K. Song and Q. Xue, 2010 Novel Ultra-Wideband (UWB) Multilayer Slotline Power Divider With Bandpass Response, *IEEE Microw. Wireless Comp. Lett.*, 20(1), pp.13-15.
- K. S. Yee, 1966 Numerical Solution of Initial Boundary Value Problems Involving Maxwell's Equations in Isotropic Media, *IEEE Trans. Antennas Propag.*, 14(3), pp.302-307.
- K. Wincza and S. Gruszczynski, 2011 Microstrip Antenna Arrays Fed by a Series-Parallel Slot-Coupled Feeding Network, *IEEE Antennas Wireless Propag. Lett.*, 10, pp.991-994.
- L. C. Shen, S. A. Long, M. R. Allerding and M. D. Walton, 1977 Resonant Frequency of a Circular Disc, Printed-Circuit Antenna, *IEEE Trans. Antennas Propag.*, 25(4), pp.595-596.
- L. Marcaccioli, P. Farinelli, M. M. Tentzeris, J. Papapolymerou, R. Sorrention, 2008 Design of a Broadband MEMS-based Reconfigurable Coupler in Ku-band. *Proceedings of European Microwave Conference*, pp.595-598.
- M. D. Abouzahra and K. C. Gupta, 1987 Multiple-Port Power Divider/Combiner Circuit Using Circular Microstrip Disk Configuration, *IEEE Trans. Microw. Theory Tech.*, 35(12), pp.1296-1302.
- M. E. Bialkowski and A. M. Abbosh, 2007 Design of a Compact UWB Out-of-Phase Power Divider, *IEEE Microw. Wireless Comp. Lett.*, 17(4), pp.289-291.
- M.-J. Park, 2011 Dual-band Unequal Power Divider with Simplified Structure, *IET Microw. Antennas Propag.*, 5(15), pp.1891-1896.
- M. K. Kim, K. Kim, Y. H. Suh and I. Park, 2000 A T-Shaped Microstrip-Line-Fed Wide Slot Antenna, *IEEE Antennas and Propagation Society International Antennas and Propagation Society International Symposium*, 3, pp.1500-1503.

M. Lucido, M. D. Migliore, G. Panariello and F. Schettino, 2008 Full Wave Analysis of Leaky-Wave Antennas, *IEEE Antennas and Propagation Society International Symposium*, pp1-4.

N. Seman, M. E. Bialkowski, and W. C. Khor, 2007 Ultra Wideband Vias and Power Dividers in Microstrip-Slot Technology, *Proceedings of Asia-Pacific Microwave Conference*, pp.1-4.

P. Hallbjorner, M. Bergstrom, M. Boman, P. Lindberg, E. Ojefors and A. Rydberg, 2005 Millimetre-wave Switched Beam Antenna Using Multiple Travelling-wave Patch Arrays, *IEE Proceedings Microwaves, Antennas and Propagation*, pp.551-555.

P. K. Singh, S. Basu, and Y. -H. Wang, 2009 Coupled Line Power Divider with Compact Size and Bandpass Response, *Electron. Lett.*, 45(17), pp.892-894.

R. V. Gatti, A. Ocera, L. Marcaccioli, and R. Sorrentino, 2006 A Dual Band Reconfigurable Power Divider for WLAN Applications, *IEEE MTT-S Int. Microw. Symposium*, pp.465-468.

P.-W. Chen, C. S. Lee and V. Nalbandian, 2002 Planar Double-Layer Leaky-Wave Microstrip Antenna, *IEEE Trans. Antennas Propag.*, 50(6), pp.832-835.

R. Chaudhuri, S. Mukherjee and C. Saha, 2011 Design of UWB Filter Using DGS and Slot SRR Array With Band Rejection for IEEE 802.11a WLAN, *IEEE Applied Electromagnetics Conference (AEMC)*, pp.1-2.

S.-K. Lin and Y.-C. Lin, 2011 A Broadband Leaky-Wave Aperture Antenna of Circular Polarization, *IEEE International Symposium on Antennas and Propagation (APSURSI)*, pp.789-792.

S. M. Ali, W. C. Chew and J. A. Kong, 1982 Vector Hankel Transform Analysis of Annular-Ring Microstrip Antenna, *IEEE Trans. Antennas Propag.*, 30(4), pp.637-644.

S. S. Gao, S. Sun, and S. Xiao, 2013 A Novel Wideband Bandpass Power Divider With Harmonic-Suppressed Ring Resonator, *IEEE Microw. Wireless Comp. Lett.*, 23(3), pp.119-121.

S. W. Wong and L. Zhu, 2008 Ultra-wideband Power Dividers with Good Isolation and Improved Sharp Roll-Off-Skirt, *IET Microw. Antennas Propag.*, 3(8), pp.1157-1163.

T.-L. Chen and Y.-D. Lin, Aperture Coupled Microstrip Line Leaky Wave Antenna With Broadside Mainbeam, *Electron. Lett.*, 34(14), pp.1366-1367.

U. H Gysel, 1975 A New N-Way Power Divider/Combiner Suitable For High-Power Applications, *IEEE MTT-S Int. Microw. Symposium*, pp.116-118.

W. F. Richards, J.-D. Ou and S. A. Long, 1984 A Theoretical and Experiment Investigation of Annular, Annular Sector, and Circular Sector Microstrip Antennas, *IEEE Trans. Antennas Propag.*, 32(8), pp.864-867.

W.-H. Hsu and K. L. Wong, 1998, Circularly-Polarised Disk-Sector Microstrip Antenna, *Electron.Lett.*, 34(23), pp.2188-2190.

W.-R. Dong and D. L. Sengupta, 1984 A Class of Broad-Band Patch Microstrip Traveling Wave Antennas, *IEEE Trans. Antennas Propag.*, 32(1), pp.98-100.

W. Menzel, 1978 A New Traveling Wave Antenna in Microstrip, *Proceedings of European Microwave Conference*, pp.302-306.

W. Yu, X. Yang, Y. Liu, R. Mittra and A. Muto, 2011 Advanced FDTD Methods, Artech House.

X. Tang and K. Mouthaan, 2009 Analysis and Design of Compact Two-Way Wilkinson Power Dividers Using Coupled Lines, *APMC*, pp.1319-1322.

Y. Cheng, W. Hong, K. Wu, 2007 Half Mode Substrate Integrated Waveguide (HMSIW) Directional Filter, *IEEE Microw. Wireless Comp. Lett.*, 17(7), pp.504-506.

Y. E. Erdemli, J. L. Volakis, D. E. Wright and R. A. Gilbert, 2002 A Broadband Substrate/Feed Design for Conformal Slot Arrays, *IEEE Antennas and Propagation Society International Symposium*, 4, pp.208-211.

Y. Hase, N. Obara, H. Saitoh and C. Ohuchi, 1996 Slot Array Antenna System for COMETS Advanced Mobile Satcom Experiments,

Y. Li, Q. Xue, E. K.-N. Yung and Y. Long, 2007 Circularly-polarised Microstrip Leaky-wave Antenna, *Electron. Lett.*, 43(14).

Y. Li, Q. Xue, E. K.-N. Yung and Y. Long, 2008 Dual-Beam Microstrip Leaky Wave Antenna With Fixed Operating Frequency, *IEEE Trans. Antennas Propag.*, 56(1), pp.248-252.

Z. Jia, Q. Zhu and F. Ao, 2006 A 2-Way Broad-Band Microstrip Matched Power Divider, *Int. Conf. Comm. Circ. Sys. Proc.*, 4, pp.2592-2596.

Z. Nie, W. C. Chew and Y. T. Lo, 1990 Analysis of the Annular-Ring-Loaded Circular-Disk Microstrip Antenna, *IEEE Trans. Antennas Propag.*, 38(6), pp.806-813.

Z. Zakaria, W. Y. Sam, M. Z. A. Abd Aziz and M. A. Meor Said, 2012 Rectangular Microstrip Patch Antenna Based on Resonant Circuit Approach, *IEEE Symposium Wireless Technology and Applications (ISWTA)*, pp.220-223.

Bibliography

1. C. W. Lim, E. H. Lim and F. L. Lo "Reconfigurable Traveling-Wave Bandpassing Power Dividers", *IET Microwaves, Antennas & Propagation*. (Submitted)
2. C. W. Lim, E. H. Lim and F. L. Lo, "Multilayered Bandpassing Couplers", *IET Microwaves, Antennas & Propagation*. (Submitted)